Development and Application of Accelerated Diffusion Ordered Spectroscopy

Zur Erlangung des akademischen Grades eines

DOKTORS DER NATURWISSENSCHAFTEN

(Dr. rer. nat.)

von der KIT-Fakultät für Chemie und Biowissenschaften des

Karlsruher Instituts für Technologie (KIT)

genehmigte

DISSERTATION

von

Dipl.-Biophys. Sebastian Spann

1. Referent: Prof. Dr. Burkhard Luy

2. Referentin: apl. Prof. Dr. Gisela Guthausen

Tag der mündlichen Prüfung: 13.12.2023

Eidesstattliche Erklärung

Hiermit versichere ich diese vorgelegte Arbeit selbstständig und wahrheitsgemäß angefertigt zu haben. Des weiteren versichere ich alle verwendeten Hilfsmittel gekennzeichnet zu haben, was aus anderen Arbeiten vollständig, oder unter Änderung entnommen wurde. Weiterhin versichere ich, dass der Inhalt dieser Arbeit bis auf die angegebenen Publikationen noch nicht veröffentlicht wurden und dass ich eine solche Veröffentlichung nicht vor Abschluss meines Promotionverfahrens vornehmen werde.

.....
Sebastian Spann

Wer kein Auge hat, dem fehlt das Licht, wer keine Einsicht hat, dem fehlt die Weisheit. Sir 3,25

für Anni und Hans

List of Publication

L. D. Thai, T. R. Guimaraes, S. Spann, A. S. Goldmann, D. Golberg, H. Mutlu, and C. Barner-Kowollik, "Photoswitchable block copolymers based on main chain α-bisimines," *Polymer Chemistry*, vol. 13, no. 39, pp. 5625–5635, 2022

X. Guo, K. S. Wetzel, S. C. Solleder, S. Spann, M. A. R. Meier, M. Wilhelm, B. Luy, and G. Guthausen, "^{1}H PFG-NMR diffusion study on a sequence-defined macromolecule: Confirming monodispersity," *Macromolecular Chemistry and Physics*, vol. 220, aug 2019

T. S. Fischer, S. Spann, Q. An, B. Luy, M. Tsotsalas, J. P. Blinco, H. Mutlu, and C. Barner-Kowollik, "Self-reporting and refoldable profluorescent single-chain nanoparticles," *Chemical Science*, vol. 9, no. 20, pp. 4696–4702, 2018

Contents

1. Motivation

When talking to friends and family I am often asked: What are you doing exactly and what are you doing it for? The most honest answer I could give is: I don't know! The field of nuclear magnetic spectroscopy is so extensive and versatile that I cannot give a simple answer. Moreover the application of NMR is so huge. But how may i describe the meaning of NMR to people that have no grasp of quantum mechanics or physical chemistry. An easy way to tell the concept of nuclear magnetic resonance is used in MRI (I always ask: "warst du schonmal in der Röhre?"). Well, family and friends don't need to know the datails of what I do exactly. However, it is always the second question that ignites my passion of what I do! But again, my answer is I don't know...

Because it is not the question what I am doing it for. I don't want to design a product, or create something to put an a wall. Researching is about asking questions and the quest to find answers. And if any scientist finds something new, as insignificant as it may seem, it is a contribution to the general knowledge of mankind. And this is why I am doing what I am doing. To elevate humanity's common understanding.

Like Newton said: *"if I have seen further, it is by standing on the shoulder of giants."*. This work is only possible, because so many people where passionate about knowledge and were determined to answer the unknown. So maybe my findings will help future generations to understand and ultimately stand on my shoulders to see even further. Working in the field of NMR I had the opportunity to talk and discuss science with many brilliant people that are equaly passionate, for which I am eternally greatful.

2. Abstract

Since the discovery of Nuclear Magnetic Resonance spectroscopy (NMR spectroscopy) in the middle of the last century the method has become an important tool in analytics and has a vast field of application. Due to its noninvasive nature, NMR plays an essential role in biology, chemistry, material science and pharmaceutical studies. NMR complements other methods in structural determination of molecules. The versatility of NMR helps scientist worldwide to study conformation and dynamics among other things. Multidimensional experiments such as COSY, TOCSY, NOESY, HMBC, or HSQC are fundamental in analytical chemistry. Consequently, the development and improvement of novel pulse sequences have been the target of many scientist. With the increasing complexity of scientific research, NMR spectroscopists have been able to adapt and develop new sequences.
With the advent of diffusion ordered NMR spectroscopy (DOSY), the method has developed into a preferential method in polymer science. The diffusion properties of macromolecular systems reveal information about the mobility and conformation. New polymer structures are developed in order to adjust the conformation. Of particular interest is the realm single chain folding. With the precise installation of folding points or conformational triggers the chains are modified to perform specific tasks. As nature is the paragon of folded polymers, scientists aim to mimic peptides, proteins and nucleic acid. DOSY has proven to be a adquate tool to investigate various folding motifs. In this work diffusion measurements were applied to single chain polymers with functionalised folding points. The host-guest system of the so called Hamilton wedge with the cyanuric acid terminus forms a hydrogen bond network that forces the single chain nanoparticle to collapse. Adding a protic solvent disrupts the hydrogen bonds and the polymer chain is unfolded. Consequently the DOSY analysis was able to determine the conformational change. Furthermore, two light induced polymer foldings were monitored with DOSY. The first system is polystyrene with 4-carboxy-2,2,6,6-tetramethylpiperidine-1-oxyl (4-carboxy-TEMPO) groups, which are intramolecularly crosslinked with (2-hydroxy-40-(2-hydroxyethoxy)-2-methylpropiophenone under UV irradiation. The diffusion analysis proves the reversible folding/ unfolding behavior of the single chain polymer. Secondly, a block copolymer is introduced with photoswitchable α-bisimine units. Diffusion ordered NMR spectroscopy is able to determine the formation of block polymers.
The method of single chain folding is expanded to the incorporation of a second folding point adding metal complexation to the aforementioned Hamilton wedge/ cyanuric acid system. Even with a more variety of changes in conformation, DOSY measurements provide sufficient information about the folding behaviour. However, further investigation has revealed the complexity of the folding. Structural elucidation of the Hamilton wedge/

cyanuric acid moiety identified the effect of the added palladium induces folding group. As DOSY measurements have gained more application over the last years, a number of new improved diffusion experiments were fabricated. The new sequences enhance many aspects and enable novel experiments. This work introduces a new DOSY pulse sequence, that reduces the experiment time drastically. The accelareted experiments utilise the Ernst angle excitation scheme, which is a sophisticated method used in NMR and magnetic resonance imaging (MRI). However, the implementation of the low flip angle procedure creates phase distortion in the DOSY experiment caused by J modulation. Here, we introduce the isotropic mixing sequence *DIPSI-2* to recover the effect of coupling evolution. The newly derived pulse sequence accelarates the experiment immensely without suffering from phase distortion. The pulse sequence is called β Excited Time Accelerated DOSY, or **BETA DOSY**. Moreover, the concept of convection compensation was inserted to supress the effect of thermal flow. The convection compensated **BETA DOSY** enables the spectroscopist to monitor the diffusion of macromolecular systems and small molecule mixtures alike. This work introduces a robust, yet fast way to determine diffusion and its applicability on dispers systems with the assignment of precise molecular weight distribution.

3. Zusammenfassung

Seit der Entdeckung der Kernspinresonanzspektroskopie (NMR Spektroskopie) in der Mitte des letzten Jahrhundert hat sich die Methode als wichtiges Werkzeug in der Analytik etabliert und ein breites Feld an Anwendungen gefunden. Aufgrund der nicht invasiven Eigenschaft spielt NMR eine wichtige Rolle in Biologie, Chemie und Materialwissenschaften bis hin zu pharmakologischen Untersuchungen. Zudem ergänzt die NMR Spektroskopie weitere Methoden der Strukturaufklärung. Die Vielseitigkeit der NMR ermöglicht es Wissenschaftlern weltweit unter anderem den molekularen Aufbau und die dynamischen Prozesse aufzuklären. Multidimensional Experimente wie COSY, TOCSY, NOESY, HMBC, oder HSQC sind ein fundamentaler Bestandteil in der analytischen Chemie geworden. Folglich haben sich viele Wissenschaftler zum Ziel gesetzt neue Pulssequenzen zu entwickeln und diese zu verbessern.
Durch das Aufkommen der Diffusion NMR Spektroskopie (DOSY) hat sich diese als beliebte Methode in der Polymerwissenschaft durchgesetzt. Die Diffusion von makromolaren Systemen gibt Aufschluss über deren Mobilität und Aufbau. Neue Polymersysteme werden entwickelt, um den molekularen Aufbau gezielt zu steuern und verändern. Von besonderem Interesse sind die Einzelkettenfaltungspolymere. Durch das präzise Einfügen von Faltungspunkten, bzw. Konformationstriggern kann das Polymer gezielt modifiziert werden, wodurch bestimmte Eigenschaften hervorgerufen werden. Dabei dient die Natur als Vorbild für Faltungstrukturen, wodurch Wissenschaftler die Eigenschaften von Peptiden, Proteinen und Nukleinsäuren nachzuahmen versuchen. DOSY hat sich als hilfsreiches Werkzeug bewiesen, um die verschiedenen Faltungsmotive zu untersuchen. Diese Arbeit zeigt, wie die Diffusions NMR Spektroskopie auf verschieden Einzelketten mit Faltungspunkten angewendet wurde. Das Schlüssel-Schloss System der sogenannten Hamilton wedge/ cyanuric acid bildet ein Wasserstoffbrückennetzwerk aus, welches die Polymerkette zur Faltung bringt. Dennoch können durch die Zugabe eines protischen Lösungsmittel diese Wasserstoffbrücken unterbrochen werden. Folglich ist es möglich mittels DOSY dieses Faltungsverhalten zu beobachten. Desweiteren wurden auch zwei lichtinduzierte Polymerfaltungssysteme mittels DOSY untersucht. Als erstes wurde ein Polystyrolsystem untersucht, welches mit 4-carboxy-2,2,6,6-tetramethylpiperidine-1-oxyl (4- carboxy-TEMPO) Gruppen funktionalisiert wurde, was unter UV Einstrahlung durch (2-hydroxy-40- (2-hydroxyethoxy)-2-methylpropiophenone verbunden wird. Die DOSY Analyse konnte den Faltungs-, bzw. Entfaltungsprozess bestätigen. Das zweite lichtinduzierte Faltungsmolekül ist ein Block Copolymer mit einem α-bisimine Lichtschalter. Die Formation des Blockpolymeres konnte mittels DOSY beobachtet werden.
Die Einzelkettenfaltung wurde erweitert durch den Einbau eines zweiten Faltungspunktes. Neben der oben aufgeführten Hamilton wedge/ cyanuric acid wurde ein Metallkomplex-

ierungspunkt eingebaut. Trotz der Erhöhung von Faltungszuständen konnte die Diffusionsmessung die Faltungsänderungen erfolgreich bestimmen. Allerdings konnten weitere intensive Untersuchungen die Komplexität der Faltung beschreiben. Durch Strukturaufklärungsuntersuchungen konnte der Effekt des palladiuminduzierten Faltungsmotivs aufgeklärt werden.
Die Zahl der DOSY Anwendungen hat in den letzten Jahren stark zugenommen. In Folge dessen wurden Diffusion NMR Experimente stets verbessert und neue Pulssequenzen entwickelt, welche die vielseitigen Aspekte der modernen Forschung dienlich sind. In dieser Arbeit wird eine neue DOSY Sequenz vorgestellt, welche die Experimentdauer drastisch verkürzt durch die Anwendung des etablierten Prinzip der Ernst Winkel Anregung. Dieses Prinzip wird in vielen NMR Experimenten verwendet und findet auch Anwendung in der Kernspintomographie. Jedoch verursacht der Prozess mit kleinen Anregungswinkel Phasenverzerrung im DOSY Spektrum durch Kopplungsentwicklung. Anbei wird der Einsatz der isotropen Mischsequenz *DIPSI-2* vorgestellt, welche den Effekt der Kopplungsevolution verhindert. Folglich wird die Diffusionsanalyse beschleunigt, ohne Phasenverzerrung in Kauf nehmen zu müssen. Die neu entwickelte Pulssequenz heißt β Excited Time Accelerated DOSY, mit **BETA DOSY** abgekürzt. Darüber hinaus konnte das Konzept der Konvektionskompensation mit der neuen Sequenz verbunden werden, um thermische Flusseffekte zu unterdrücken. Das konvektionskompensierte **BETA DOSY** ermöglicht es die Diffusion von kleinen Molekülgemischen bis hin zu makromolaren Systemen zu untersuchen. Diese Arbeit stellt eine zuverlässige und dennoch schnelle Pulssequenz vor, um die genaue Bestimmung der Kettenlängenverteilung von dispersiven Polymeren zu bestimmen.

4. Theory

The aim of this chapter is to give the reader a brief overview into the theory of nuclear magnetic resonance spectroscopy.
To understand the benefits of the newly derived pulse sequence one has to understand what J modulation is and how isotropic mixing prevents this effect. Therefore, we need to highlight the essentials of product operator formalism. Moreover, the concept of Ernst angle excitation is summerised. Furthermore, this chapter tackles the theory of diffusion measurement with NMR pulse sequences. As diffusion is commonly used on macromolecular system this chapter is completed with a brief introduction of macromolecules.

4.1. NMR Basics

Nuclear **M**agnetic **R**esonance spectroscopy (NMR) is an essential method in chemistry, phsysics, biology and in medical studies. Most atomic nuclei possess a spin, which is referred to I and has integer ($I = 1, 2, 3 \cdots$), or half integer ($\frac{1}{2}, \frac{3}{2} \cdots$) values. The most common nuclei in organic chemistry are ^{1}H and ^{13}C with $I = \frac{1}{2}$. This intrinsic property is the basis of NMR and is linked to a magnetic moment. The magnetic moment aligns in a static magnetic field dependent on its gyromagnetic ratio γ.

4.1.1. Energy Levels and Matrix Representation

The fundamental concept of spectroscopy is $h\nu = \Delta E$. Radiation of a specific frequency manipulates energy levels. In NMR these energy levels are caused by the nuclear spin in a static magnetic field.

$$\Delta E = h\nu = \hbar\omega = \hbar\gamma B_0 \tag{4.1}$$

With $I = \frac{1}{2}$ the spins have two possible energy levels $m = \pm\frac{1}{2}$. A Common nomenclature in NMR is to call $m = +\frac{1}{2} = \alpha$ and $m = -\frac{1}{2} = \beta$. The Zeeman splitting is given in figure 4.1. The energy difference depends on the magnetic field and the gyromagnetic ratio γ.

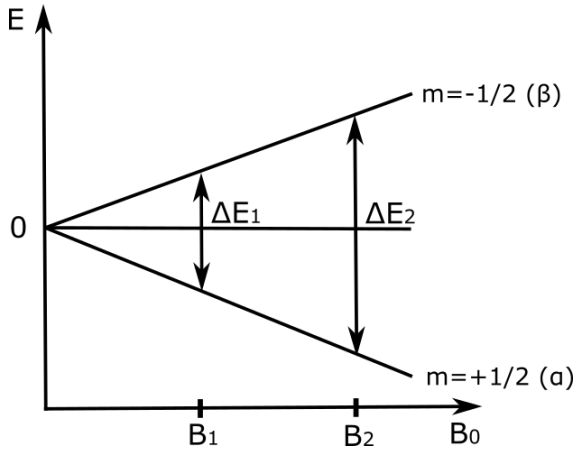

Figure 4.1: Zeeman splitting of spin $\frac{1}{2}$ nuclei in a magnetic field.

The energy level approach helps to understand the origin of NMR. However, the concept has disadvanteges when explaining the outcome of simple pulse sequences. The application of radio frequency pulses rotate the aligned spins. Moreover, the spins precess around the B_0 field with the Larmor frequency (ω), that is the origin of the detected free induction decay (FID). Consquently, the description of NMR experiments is given by rotations [4; 5]. The angular momentum of the z component is represented by the operator $\hat{I}_z$, analog are $\hat{I}_x$ and $\hat{I}_y$. The matrix representations are given in 4.2:

$$\hat{I}_x = \begin{pmatrix} 0 & \frac{1}{2} \\ \frac{1}{2} & 0 \end{pmatrix} \hat{I}_y = \begin{pmatrix} 0 & -\frac{i}{2} \\ \frac{i}{2} & 0 \end{pmatrix} \hat{I}_z = \begin{pmatrix} \frac{1}{2} & 0 \\ 0 & -\frac{1}{2} \end{pmatrix} \hat{1} = \begin{pmatrix} 1 & 0 \\ 0 & 1 \end{pmatrix} \tag{4.2}$$

These operators are in the centre of the product operator formalism, that is introduced in the next section. To obtain the matrix representation we skipped many calculations as it is not important to apply them later.

4.1.2. Product Operator Formalism

The calculation of NMR experiments is achieved by using a combination of basis operators. The product operator is an exact tool of describing the outcome of pulse sequences. Although in practice the sample has many spins that interact with each other, summarising identical spins into a so called ensemble of spins simplifies the calculation [5].

Introducing the spin density operator simplifies the calculation. A detailed description of the deviation of the spin density is given in literature and is beyond the scope of this book [4; 5].

$$\hat{\rho} = \overline{|\Psi\rangle \langle\Psi|} \tag{4.3}$$

Starting with the spin density operator it is important to understand how it evolves over time. The time evolution is given by the Liouville-von Neumann equation:

$$\frac{\partial}{\partial t}\hat{\rho}(t) = -i\big[\hat{H}, \hat{\rho}(t)\big] \tag{4.4}$$

The squared brackets signify the commutator of $\hat{H}$ and $\hat{\rho}$. A simplification is given by the magic formula and is applicable on the product operator approach:

$$A \xrightarrow{\phi B} \begin{cases} A & \text{if } [A,B] = 0 \\ A\cos(\phi) + i\sin(\phi)[A,B] & \text{if } [A,B] \neq 0 \end{cases} \tag{4.5}$$

The commutator rules of cartesian product operators are given by:

$$[\hat{I}_\alpha, \hat{I}_\beta] = i\varepsilon_{\alpha\beta\gamma}\hat{I}_\gamma \text{ with } \alpha,\beta,\gamma \in \begin{cases} +1\ x,y,z & \text{cyclic} \\ -1\ x,z,y & \text{anti-cyclic} \end{cases} \tag{4.6}$$

ε represents the Levi-Citiva-Symbol which signifies the permutation rules. In a cyclic permutation (e.g. x, y, z) $\varepsilon = 1$, in an anticyclic permutation (e.g. x, z, y) $\varepsilon = -1$. Further commutator rules with context to the product operator formalism to simplify the calculations:

$$[AB, CD] = 0 \quad \text{e.g.} \quad [\hat{I}_{1x}\hat{I}_{2x}, \hat{I}_{1y}\hat{I}_{2y}] = 0 \tag{4.7}$$

$$[AC, BC] = [A, B] \quad \text{e.g.} \quad [2\hat{I}_{1x}\hat{I}_{2z}, \hat{I}_{1z}\hat{I}_{2z}] = [\hat{I}_{1x}, \hat{I}_{1z}] = -i\hat{I}_{1y} \tag{4.8}$$

$$[AC, B\hat{1}] = [A, B] \quad \text{e.g.} \quad [2\hat{I}_{1z}\hat{1}_{2z}, \hat{I}_{1x}] = [\hat{I}_{1z}, \hat{I}_{1x}]\hat{I}_{2z} = 2\hat{I}_{1y}\hat{I}_{2z} \tag{4.9}$$

The utility of describing the NMR experiment with the help of the product operator formalism is illustrated at the so called spin echo [4]. The sequence consists of an excitation pulse β, a delay τ a inversion pulse and a second delay of the same length τ. The graphical scheme of the spin echo is given in figure 4.2.

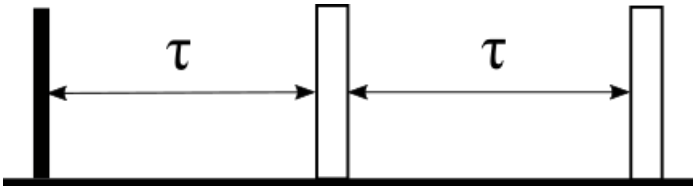

Figure 4.2: Graphical representation of the spin echo sequence

Starting with the longitudinal magnetisation $\hat{I}_z$ and applying a pulse from x direction. The Hamiltonian of the excitation pulse is $\hat{H}_{x,pulse} = \beta\hat{I}_x$ and leads to:

$$\hat{I}_z \xrightarrow{\beta\hat{I}_x} \cos(\beta)\hat{I}_z - \sin(\beta)\hat{I}_y \tag{4.10}$$

After the pulse the delay τ follows. With no external disturbance the system precesses freely. The Hamiltonian of free precession is $\hat{H}_{free} = \Omega\hat{I}_z$. This indicates a rotation around the z axis. Therefore the term $\cos(\beta)\hat{I}_z$ is uneffected by the rotation and can be excluded in the next step. Only the term $-\sin(\beta)\hat{I}_y$ evolves during τ. This leads to:

$$\xrightarrow{\Omega\tau\hat{I}_z} \cos(\beta)\hat{I}_z + \Big\{ -\sin(\beta)\cos(\Omega\tau)\hat{I}_y + \sin(\beta)\sin(\Omega\tau)\hat{I}_x \Big\} \tag{4.11}$$

The subsequent inversion pulse is about y, consequently the term $\sin(\beta)\hat{I}_y$ is unaffected. The Hamiltonian of the 180° pulse is $\hat{H}_{y,t_\pi} = \omega t_\pi \hat{I}_y$. t_π is the duration of the pulse. This term can be simplyfied to $\hat{H}_{y,t_\pi} = \pi\hat{I}_y$ and leads to:

$$\xrightarrow{\pi\hat{I}_y} -\cos(\beta)\hat{I}_z + \Big\{ -\sin(\beta)\cos(\Omega\tau)\hat{I}_y - \sin(\beta)\sin(\Omega\tau)\hat{I}_x \Big\} \tag{4.12}$$

To get to the right side we used $\cos(\pi) = -1$ and $\sin(\pi) = 0$. Unsurprisingly the π pulse inverts the sign to $-\cos(\beta)$ and $-\sin(\beta)\sin(\Omega\tau)\hat{I}_x$. The term $\hat{I}_y$ is uneffected by the y rotation. After the 180° pulse the second delay τ follows with the Hamitonian of free precession:

$$\begin{aligned}\xrightarrow{\Omega\tau\hat{I}_z} -\cos(\beta)\hat{I}_z + \Big\{ &+\sin(\beta)\cos(\Omega\tau)\cos(\Omega\tau)\hat{I}_y - \sin(\beta)\cos(\Omega\tau)\sin(\Omega\tau)\hat{I}_x \\ &+\sin(\beta)\sin(\Omega\tau)\cos(\Omega\tau)\hat{I}_x + \sin(\beta)\sin(\Omega\tau)\sin(\Omega\tau)\hat{I}_y \Big\}\end{aligned} \tag{4.13}$$

The result of the spin echo seems rather complex. However, the term in the brackets can be simplified. At first the $\hat{I}_x$ terms can be cancelled. $-\sin(\beta)\cos(\Omega\tau)\sin(\Omega\tau)\hat{I}_x + \sin(\beta)\sin(\Omega\tau)\cos(\Omega\tau)\hat{I}_x = 0$. The result is given:

$$= -cos(\beta)\hat{I}_z \Big\{ +\sin(\beta)\cos^2(\Omega\tau)\hat{I}_y + \sin(\beta)\sin^2(\Omega\tau)\hat{I}_y \Big\} = -\cos(\beta)\hat{I}_z + \sin(\beta)\hat{I}_y \tag{4.14}$$

To get to the right side we used the identity $\cos^2(\Theta) + \sin^2(\Theta) \equiv 1$. With the help of product operator formalism result of the spin echo with β-excitation is calculated easily. Starting with $\sin(\beta)\hat{I}_y$ we end in $\sin(\beta)\hat{I}_y$ again. Therefore the chemical shift evolution is refocused. On the other hand the $\cos(\beta)\hat{I}_z$ term is transferred into $-\cos(\beta)\hat{I}_z$, due to the inversion pulse. In figure 4.2 the second delay τ is followed by an additional 180° pulse. The result is easily computed as $\pi\hat{I}_y$ changes the sign of the term $-\cos(\beta)\hat{I}_z$ and leaving $\sin(\beta)\hat{I}_y$ uneffected.

$$\xrightarrow{\pi\hat{I}_y} \cos(\beta)\hat{I}_z + \sin(\beta)\hat{I}_y \tag{4.15}$$

The result in equation 4.15 illustrate the effect of the β pulse on the longitudinal magnetisation. Neglecting the effect of relaxation the β pulse stores the unexcited magnetisation. Moreover arranging the 180° pulses in constant delays τ stores the z magnetisation and recovers the chemical shift evolution.

4.2. **Planar Mixing**

After the brief overview of product operator formalmism on the spin echo we expand to a two spin system. The utility of the product operator formalism is eminent when calculating coupled spins. In a single spin system we used only four operators, namely $\hat{I}_x, \hat{I}_y, \hat{I}_z$ and $\hat{1}$. In two spin systems the density operator is expressed in a linear combination of 16 operators. Starting with spin 1 the four corresponding operators are $\hat{I}_{1x}, \hat{I}_{1y}, \hat{I}_{1z}$ and $\hat{1}$. Analog spin 2 operatores are: $\hat{I}_{2x}, \hat{I}_{2y}, \hat{I}_{2z}$ and $\hat{2}$. Thus, the number of linear combinations is 16. However, the combination of $\hat{1}\hat{2}$ does not give rise to observable magnetisation. Moreover a combination with the unity operator can be abbreviated simply to the operator of the other spin, e.g. $\hat{I}_{1x}\hat{2}$ is simply $\hat{I}_{1x}$.

The necessity of computing two spin operators is to describe coupling effects. Scalar coupling is of particular interest as it is an intramolecular effect and gives structural information [6; 7]. During free evolution coupling evolves along side with the offset. The Hamiltonian of two spins is given by:

$$\hat{H}_{twospins} = \Omega_1 \hat{I}_{1z} + \Omega_2 \hat{I}_{2z} + 2\pi J_{12} \hat{I}_{1z} \hat{I}_{2z} \tag{4.16}$$

Ω_1 and Ω_2 are the offsets of spin 1 and spin 2 respectively. J_{12} is the scalar coupling constant, which has to be multiplied by 2π in order to get the angular frequency as J is commonly given in Hertz. In a coupled spin system the experimenter has to consider more than just offset effects. The existance of scalar coupling evolution, often referred to J modulation, generates anti-phase terms. Anti-phase is transformed into a doublet with peaks of opposite sign. Consequently J modulation leads to distorted spectra in a multi spin system.
In this section we introduce the concept to recover the effect of J modulation. With planar mixing conditions during free evolution, the peaks in the spectrum are in phase. In literature there are many different pulse sequences that generate planar mixing conditions [8; 9; 10; 11; 12]. Planar mixing experiments are designed to preserve a specific component of magnetisation. As an example the planar mixing Hamiltonian of x calculates the results in x magnetisation. The Hamiltonian is:

$$\hat{H}_{planar,x} = 2J\pi(\hat{I}_{1y}\hat{I}_{2y} + \hat{I}_{1z}\hat{I}_{2z}) \tag{4.17}$$

Starting with $\hat{I}_{1x}$ term and applying planar mixing conditions. Because the operator commute with each other, the order in which the operators are applied is irrelevant. At first we start with $2J\pi\Delta(2\hat{I}_{1z}\hat{I}_{2z})$

$$\xrightarrow{2J\pi\Delta(2\hat{I}_{1z}\hat{I}_{2z})} \hat{I}_{1x}\cos(\pi J\Delta) + 2\hat{I}_{1y}\hat{I}_{2z}\sin(\pi J\Delta) \tag{4.18}$$

In anticipation of rather complex calculations we abbreviate $\cos(\pi J\Delta) = C$ and $\sin(\pi J\Delta) = S$. Calculating further:

$$\xrightarrow{2J\pi\Delta(2\hat{I}_{1y}\hat{I}_{2y})} \hat{I}_{1x}CC + 2\hat{I}_{1y}\hat{I}_{2z}SC - 2\hat{I}_{1z}\hat{I}_{2y}CS + \hat{I}_{2x}SS \tag{4.19}$$

Next we examine the outcome of planar mixing on $\hat{I}_{2x}$ using the aforementioned abbreviation:

$$\xrightarrow{2J\pi\Delta(2\hat{I}_{1z}\hat{I}_{2z})} \hat{I}_{2x}C + 2\hat{I}_{1z}\hat{I}_{2y}S \tag{4.20}$$

$$\xrightarrow{2J\pi\Delta(2\hat{I}_{1y}\hat{I}_{2y})} \hat{I}_{2x}CC + 2\hat{I}_{1z}\hat{I}_{2y}SC - 2\hat{I}_{1y}\hat{I}_{2z}CS + \hat{I}_{1x}SS \tag{4.21}$$

Next we simply add the results of $\hat{I}_{1x}$ and $\hat{I}_{2x}$ in order to obtain the effect of planar mixing on the x magnetisation.

$$\begin{aligned}\hat{I}_{1x} + \hat{I}_{2x} = \hat{I}_{1x}CC + \hat{I}_{1x}SS + \hat{I}_{2x}CC + \hat{I}_{2x}SS + 2\hat{I}_{1y}\hat{I}_{2z}SC - 2\hat{I}_{1z}\hat{I}_{2y}CS \\ -2\hat{I}_{1y}\hat{I}_{2z}CS + 2\hat{I}_{1z}\hat{I}_{2y}SC\end{aligned} \tag{4.22}$$

On the left side of the results, we use the identity $\cos^2(\Theta) + \sin^2(\Theta) \equiv 1$ in order simplify the equation. The terms on the right side are aligned in order to visualise that they cancel each other. After the modification we find:

$$\hat{I}_{1x} + \hat{I}_{2x} \xrightarrow{\hat{H}_{planar,x}} \hat{I}_{1x} + \hat{I}_{2x} \tag{4.23}$$

This concludes that the x magnetisation does not evolve under planar mixing conditions with the active Hamiltonian $\hat{H}_{planar,x} = 2J\pi(\hat{I}_{1y}\hat{I}_{2y} + \hat{I}_{1z}\hat{I}_{2z})$. The planar mixing conserves the spin state of x. Next we perform the calculation for $\hat{I}_{1y}$ with $\hat{H}_{planar,x}$. This time we start with $2J\pi\Delta(2\hat{I}_{1y}\hat{I}_{2y})$:

$$\hat{I}_{1y} \xrightarrow{2J\pi\Delta(2\hat{I}_{1y}\hat{I}_{2y})} \hat{I}_{1y} \tag{4.24}$$

Unsurprisingly the state of $\hat{I}_{1y}$ is preserved. Next the $2J\pi\Delta(2\hat{I}_{1z}\hat{I}_{2z})$ is applied and leads to:

$$\xrightarrow{2J\pi\Delta(2\hat{I}_{1z}\hat{I}_{2z})} \hat{I}_{1y}C - 2\hat{I}_{1x}\hat{I}_{2z} \tag{4.25}$$

Analog to $\hat{I}_{1y}$ we calculate the result of $\hat{I}_{2y}$. In the first step the $\hat{I}_{2y}$ component is preserved:

$$\hat{I}_{2y} \xrightarrow{2J\pi\Delta(2\hat{I}_{1y}\hat{I}_{2y})} \hat{I}_{2y} \tag{4.26}$$

Next we calculate the outcome of the $2J\pi\Delta(2\hat{I}_{1z}\hat{I}_{2z})$ term on $\hat{I}_{2y}$. The result of the calculation is given:

$$\xrightarrow{2J\pi\Delta(2\hat{I}_{1z}\hat{I}_{2z})} \hat{I}_{2y}C - 2\hat{I}_{1z}\hat{I}_{2x} \tag{4.27}$$

Finally we add the results of $\hat{I}_{1y}$ and $\hat{I}_{2y}$. The evolution of $\hat{H}_{planar,x}$ in y magnetisation is:

$$\hat{I}_{1y} + \hat{I}_{2y} = \hat{I}_{1y}C - 2\hat{I}_{1x}\hat{I}_{2z} + \hat{I}_{1y}C - 2\hat{I}_{1x}\hat{I}_{2z} \tag{4.28}$$

The magnetisation of y is not refocused. It evolves during $\hat{H}_{planar,x}$. The same holds true for z magnetisation. Consequently, $\hat{H}_{planar,x}$ is only applicable for preserving x magnetisation. This illustrates the limits of planar mixing. It only recovers one component, while the spins in the other directions evolve.

4.3. **Isotropic Mixing**

In order to conserve the state of all three components the so called isotropic mixing conditions are used. The Hamiltonian is isotropic and therefore x, y and z are refocused [13]. The Hamiltonian $\hat{H}_J$ is given:

$$\hat{H}_J = 2\pi \sum_{k>j} J_{k,j} \cdot (\hat{I}_{kz}\hat{I}_{jz} + \hat{I}_{ky}\hat{I}_{jy} + \hat{I}_{kx}\hat{I}_{jx}) \tag{4.29}$$

To illustrate the effect of the isotropic mixing we compute the evolution of $\hat{I}_{1y} + \hat{I}_{2y}$. We can skip the calculation of $2J\pi\Delta(2\hat{I}_{1y}\hat{I}_{2y})$, because it has no effect on y magnetisaton. We use the same abbriviation of 4.2 with $\cos(\pi J\Delta) = C$ and $\sin(\pi J\Delta) = S$. Continuing with $2J\pi\Delta(2\hat{I}_{1z}\hat{I}_{2x})$ we have:

$$\hat{I}_{1y} \xrightarrow{2J\pi\Delta(2\hat{I}_{1z}\hat{I}_{2z})} \hat{I}_{1y}C - 2\hat{I}_{1x}\hat{I}_{2z} \tag{4.30}$$

Next we calculate the outcome of $2J\pi\Delta(2\hat{I}_{1x}\hat{I}_{2x})$ on the magnetisation:

$$\xrightarrow{2J\pi\Delta(2\hat{I}_{1x}\hat{I}_{2x})} \hat{I}_{1y}CC - 2\hat{I}_{1x}\hat{I}_{2z}SC + 2\hat{I}_{1z}\hat{I}_{2x}CS + \hat{I}_{2y}SS \tag{4.31}$$

analog to the calculation of $\hat{I}_{1y}$ we get the results of $\hat{I}_{2y}$:

$$\xrightarrow{2J\pi(\hat{I}_{1x}\hat{I}_{2x}+\hat{I}_{1y}\hat{I}_{2y}+\hat{I}_{1z}\hat{I}_{2z})} \hat{I}_{2y}CC - 2\hat{I}_{1z}\hat{I}_{2x}SC + 2\hat{I}_{1x}\hat{I}_{2z}CS + \hat{I}_{1y}SS \tag{4.32}$$

To illustrate the effect of the isotropic mixing conditions on the y magnetisation we add the results of $\hat{I}_{1y}$ and $\hat{I}_{2y}$:

$$\begin{aligned}\hat{I}_{1y} + \hat{I}_{2y} = \hat{I}_{1y}C^2 + \hat{I}_{1y}S^2 + \hat{I}_{2y}C^2 + \hat{I}_{2y}S^2 - 2\hat{I}_{1x}\hat{I}_{2z}SC + 2\hat{I}_{1z}\hat{I}_{2x}CS \\ +2\hat{I}_{1x}\hat{I}_{2z}CS - 2\hat{I}_{1z}\hat{I}2xSC\end{aligned} \tag{4.33}$$

The result may look complicated at first, but we use the same simplification from section 4.2. The left side of the results can be reduced with the identity $\cos^2(\Theta) + \sin^2(\Theta) \equiv 1$. On the right side the terms have been optically aligned in anticipation of the similar cancelation of section 4.2. After the simplificatio we have:

$$\hat{I}_{1y} + \hat{I}_{2y} \xrightarrow{2J\pi(\hat{I}_{1x}\hat{I}_{2x}+\hat{I}_{1y}\hat{I}_{2y}+\hat{I}_{1z}\hat{I}_{2z})} \hat{I}_{1y} + \hat{I}_{2y} \tag{4.34}$$

Isotropic mixing refocuses the y magnetisation entirely. In addition, isotropic mixing preseves all spin components namely x, y and z.

$$\hat{I}_{1x} + \hat{I}_{2x} \xrightarrow{2J\pi(\hat{I}_{1x}\hat{I}_{2x}+\hat{I}_{1y}\hat{I}_{2y}+\hat{I}_{1z}\hat{I}_{2z})} \hat{I}_{1x} + \hat{I}_{2x} \tag{4.35}$$

$$\hat{I}_{1z} + \hat{I}_{2z} \xrightarrow{2J\pi(\hat{I}_{1x}\hat{I}_{2x}+\hat{I}_{1y}\hat{I}_{2y}+\hat{I}_{1z}\hat{I}_{2z})} \hat{I}_{1z} + \hat{I}_{2z} \tag{4.36}$$

4.4. **Fast Pulsing**

Most experiments in NMR spectroscopy start with a 90° pulse as an excitation pulse. The aim is to have full signal intensity, because all longitudinal magnetisation is rotated into the transversal plain. However this implies to have long relaxation delays to recover the z magnetisation before the next scan. Moreover, a repetetive pulse scheme is typical in NMR experiments to gain sufficient sensitivity. Therefore it is in the experimenters interest to have fast repetition to accumulate signals. In this chapter we will introduce the fast pulsing scheme of Ernst. This introduction uses the same nomenclature to describe the low flip angle concept of Ernst [14; 15; 16].

Assuming a low flip angle and short relaxation delay (T) the longitudinal magnetisation does not reach its equilibrium state M_0 at the beginning of the next transient. However, after a small number of repetition the magnetisation reaches dynamic equilibrium. In this steady state the amount of excited magnetisation equals the amount of recoverd magnetisation. The z magnetisation before the pulse is called $M_Z(0_-)$ with the magnetisation after the recycle delay being $M_Z(T)$. It follows that in the steady state $M_Z(0_-) = M_Z(T)$. Applying the the next β pulse the resulting magnetisation is:

$$M_Z(0_+) = M_Z(0_-)\cos(\beta) \tag{4.37}$$

The magnetisation evolves until the end of the recycle time to:

$$M_Z(T) = M_Z(0_+)E_1 + M_0(1 - E_1) \tag{4.38}$$

with $E_1 = exp\Big(-{}^{T}/_{T_1}\Big)$ and T_1 being the longitudinal relaxation time. It follows:

$$M_Z(0_-) = M_0\frac{1 - E_1}{1 - E_1\cos(\beta)} \tag{4.39}$$

Next we want to observe the signal in this dynamic equlibrium. The transversal magnetisation after the pulse is denoted as $M_X(0_+)$. After β excitation the initial amplitude of the FID is:

$$M_X(0_+) = M_0\frac{1 - E_1}{1 - E_1\cos(\beta)}\sin(\beta) \tag{4.40}$$

Consequently the maximum signal is found with an excitation pulse different from a 90° pulse. The optimal pulse (β_{opt}) is now determined by the relation:

$$\cos(\beta_{opt}) = E_1 = exp(-{}^{T}/_{T_1}) \tag{4.41}$$

Knowing the longitudinal relaxation time the experimenter can set relaxation delay and β_{opt} to optimise the signal to noise ration per experiment time. The short flip angle method has many applications and is known as Ernst angle. It is implemented in magnetic resonance imaging (MRI) to speed up clinical measurement time [17]. Additioanlly the method is commonly used in NMR spectroscopy. Therefore the measuremnet time of multidimensional NMR experiments can be reduced drastically [18; 19].

4.5. **Diffusion Ordered Spectroscopy**

This section gives a brief introduction into Diffusion Ordered NMR Spectroscopy (DOSY) [20; 21; 22; 23]. This method uses gradients to monitor the diffusion with NMR. DOSY has become a very popular methods in analytics [24]. Its application ranges from small molecule mixtures [25], pharmaceuticals [26], biomolecules [27; 28] to macromolecules [29]. Moreover, DOSY measurements complement other analytical methods in detecting diffusion or particle size [30]. It rivals chromatography in determining particle size and weight distribution [31; 32; 2].

4.5.1. **Diffusion**

Self-diffusion describes the random translational displacement of particles (ions or molecules). This random motion is caused by the thermal energy of the system and implies that no external force is applied, in contrast to convection caused by a concentration gradient. The self-diffusion in an isotropic system is described by the probability $P(r_0, r, t_d)$. So starting at the position r_0 after the time t_d the probability of the particle being at position r is:

$$P(r_0, r, t_d) = (4\pi D t_d)^{-3/2} exp\Big(- \frac{(r - r_0)^2}{4 D t_d} \Big) \tag{4.42}$$

D is the self-diffusion coefficient. Equation 4.42 describes gaussian distribution of the occupied volume relative to the initial position, that broadens with increasing diffusion time t_d. The diffusion root-mean-square displacement $\Big(\langle X^2 \rangle\Big)^{1/2}$ is described by the Einstein equation:

$$\Big(\langle X^2 \rangle\Big)^{1/2} = \Big(n D t_d\Big)^{1/2} \tag{4.43}$$

with n being 2, 4, or 6 for one-, two, or three-dimensional diffusion. The measurement of the diffusion coefficient is of particular interest to the experimenter as it is directly related to the particle size. With the Einstein-Smolukowski equation:

$$D = \frac{k_b T}{f} = \frac{RT}{Nf} \tag{4.44}$$

the diffusion coefficient is connected to the hydrodynamic friction f [33; 34]. T is the absolute temperature, k_b is the Boltzmann constant, N is Avogadro's number and R is the gas constant. With the approximation of a spherical conformation and the viscosity η, f is given by the Stokes Equation:

$$f = 6\pi\eta r_{hyd} \tag{4.45}$$

The friction is dependent on the hydrodynamic radius r_{hyd} of the particle. Combining equation 4.45 and 4.44 leads to the well known Stokes-Einstein equation:

$$D = \frac{k_b T}{6\pi\eta r_{hyd}} \tag{4.46}$$

This equation links the particle size to its self-diffusion [35; 36]. Although, the hydrodynamic radius is dependent on the molecular conformation and solvent interaction, the relationship in equation 4.46 relates the molecular size to the diffusion to a good approximation.

4.5.2. **Pulsed Field Gradients**

Diffusion ordered spectroscopy in NMR utilises magnetic field gradients in order to label the position of the nuclear spins. The concept of using external gradients to monitor diffusion was introduced by Hahn [37] and has been the target of many additions and improvements [38; 39; 40; 41]. However, all DOSY experiments can be reduced to the basic concept.

Equation 4.47 describes the effect of the external magnetic gradients:

$$G = \frac{\partial B_Z}{\partial x}\hat{i} + \frac{\partial B_Z}{\partial y}\hat{j} + \frac{\partial B_Z}{\partial z}\hat{k} \tag{4.47}$$

with $\hat{i}$, $\hat{j}$ and $\hat{k}$ being the unit vectors for x, y and z directions. In conclusion, magnetic field at position r is given by the relationship:

$$B(r) = B_0 + Gr \tag{4.48}$$

A homogeneous static field B_0 receives an additional spatially dependent magnetic contribution due to the gradient. Therefore, the nuclear spins precess with the angular frequency of:

$$\omega(r) = -\gamma B(r) \tag{4.49}$$

The amount of the gradient contribution is given by the phase angle Φ. The development of Φ depends linearly on the magnetic field and the duration of the gradient δ. Most experiments use only z gradients, as the NMR tube elongates along z, the spatially dependent phase is given by:

$$\Phi(z) = -\gamma B(z)\delta \tag{4.50}$$

The applied gradient pulse creates a corkscrew pattern of the magnetisation [42]. On the left side of figure 4.3 the applied pulsed gradient changes the phase Φ dependent on the z position. The second gradient has opposite sign and therfore refocuses the phases. The full recovery of the signals, ignoring relaxation, only occurs without diffusion in the NMR tube. However the pulsed field gradients are utilised to monitor diffusion.

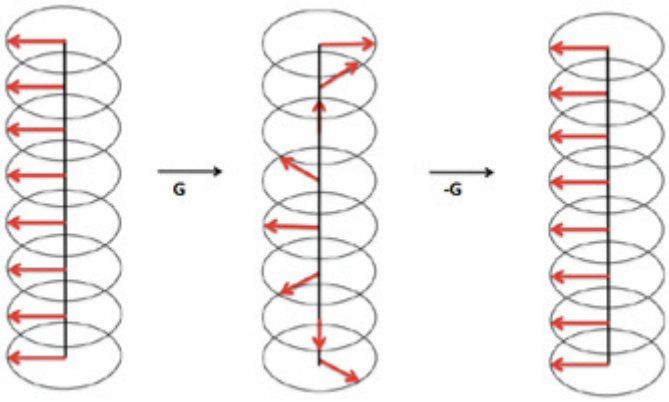

Figure 4.3: Spatially dependent phase development of a pulsed field gradient. G encodes the spins, the subsequent -G refocuses the excited spins.

4.5.3. **Pulsed Gradient Spin Echo**

In this part the knowledge of self diffusion and the effect of the pulsed field gradient lead to the development of the simplest DOSY experiment called the Pulsed Gradient Spin Echo (PGSE). The pulse sequence scheme is desribed in figure 4.4. The first black bar represents a 90° pulse and excites the magnetisation. After the excitation the transversal magnetisation is dephased by the first gradient pulse with the fixed pulse duration of δ. The dephasing is equal to figure 4.3. With the end of the encoding gradient pulse the a delay Δ is applied. This delay is referred to as the diffusion delay. Instead of applying a second gradient pulse with opposite sign a 180° pulse is applied in the centre of the sequence. A 180° pulse is represented by an empty box. This results in an inversion of the magnetisation, i.e. magnetisation on x is flipped to -x. Going back to figure 4.3 the corkscrew pattern is reversed. Consequently the second gradient pulse leads to decoding in a similar manner of a gradient pulse of opposite sign without application of an inversion pulse.

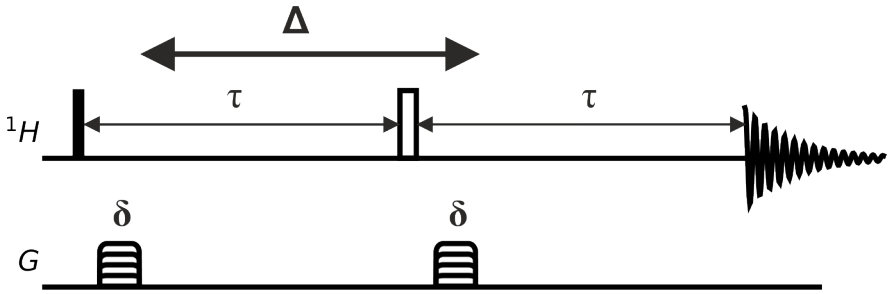

Figure 4.4: Graphical representation of the Pulsed Gradient Spin Echo Sequence.

The benefit of this pulse sequence was evaluated in 4.1.2. The spin echo refocusses the chemical shift evolution. Without any translational motion the signals are recovered. However with diffusion present phase shifts caused by the gradients differ and consequently the echo signal is not fully recovered. The first gradient pulse gives the spins spatial information and the second gradient reads out the spatial information. Due

to diffusion the spins are not located at their initial position. Therefore, the signal attenuates dependent on the diffusion coefficient D of the particles. This attenuation is described by the Stejskal-Tanner equation [43]:

$$ln\left(\frac{I_{(2\tau,G)}}{I_{2\tau,0}}\right) = -\gamma^2 G^2 \delta^2 (\Delta - {}^{\delta}/_{3}) D = -bD \tag{4.51}$$

Δ is the diffusion time, δ is the gradient length, γ is the gyromagnetic constant and G is the gradient strength. The term $I_{(2\tau,G)}$ describes the intensity of the signal after 2τ and with the application of the gradient G. Thus, the term $I_{(2\tau,0)}$ describes the intensity without the gradient. Consequently the Stejskal-Tanner equation describes the decay of the signal intensity caused by diffusion with the application of a gradient. The term - $\gamma^2 G^2 \delta^2 (\Delta - {}^{\delta}/_{3}) D$ is often simplyfied to $-bD$. The value b represents the parameters of the experiment and is set by the experimenter. Although, δ or Δ can be adapted in the experiment, it is beneficial to change G. Adapting either delay to monitor diffusion would counteract the sequences constant time. With τ being constant in each step the T_2 relaxation is seperated from the diffusion attenuation. The DOSY experiment increases the gradient strength stepwise and plots the signal attenuation to calculate the diffusion constant.

4.5.4. **Pulsed Gradient Stimulated Echo**

In order to monitor the diffusion sufficiently the spectroscopist has to set the gradient strength and gradient length as well as the diffusion time. The gradient performance is dependent on the spectrometer hardware and is limited to some extent. Therefore Δ is a adjusted easyly. However, the signals decay with the transversal relaxation time T_2. Ultimately, the diffusion delay is limited. The stimulated echo is an improvement of the diffusion measurement as it is able to circumvent the transversal relaxation. The graphical represantation of the stimulated echo (STE) is given in figure 4.5. After the first gradient a second 90° pulse is applied. This pulse flips the transversial magnetisation into z direction. With the spins being transversial they relax with the longitudinal relaxation time T_1 [44]. With $T_1 \geq T_2$ the diffusion time can be increrased. In order to rephase the magnetisation a second 90° pulse flips the magnetisation back into the transverial plain after the duration of τ_m.

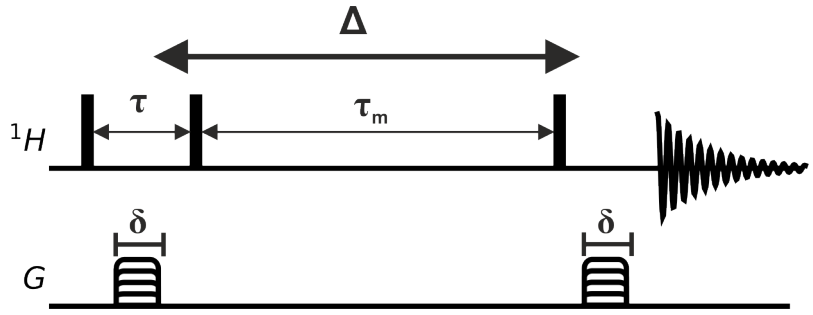

Figure 4.5: Graphical representation of the stimulated echo sequence.

4.6. **BPLED and dSTE**

Before discussing the newly derived pulse sequence, we have to remind ourselves of what is commonly applied in diffusion measurement with NMR.
The development of DOSY lead to number of different pulse sequences. Two sequences, **BPLED** and **dSTE** are discussed in the following pages, as they are common pulse sequences and therefore popular with spectroscopists.

4.6.1. **Bipolar Longitudinal Eddy Current Delay**

First we start with so called **B**i**P**olar **L**ongitudinal **E**ddy current **D**elay sequence (**BPLED**). The graphical representation of the **BPLED** is shown in figure 4.6.
Like the Spin Echo sequence, the basic principle remains the same which shall be recited shortly. After excitation, a gradient spacially encodes the spins in the sample, which are decoded with a second gradient of opposite sign. The signal, otherwise recovered (ignoring relaxation), is attenuated by the particles diffusion. Although, the **BPLED** pulse sequence looks somewhat more complicated, this simple concept still holds true. Nevertheless the additions made, improve the quality of the DOSY measurement.

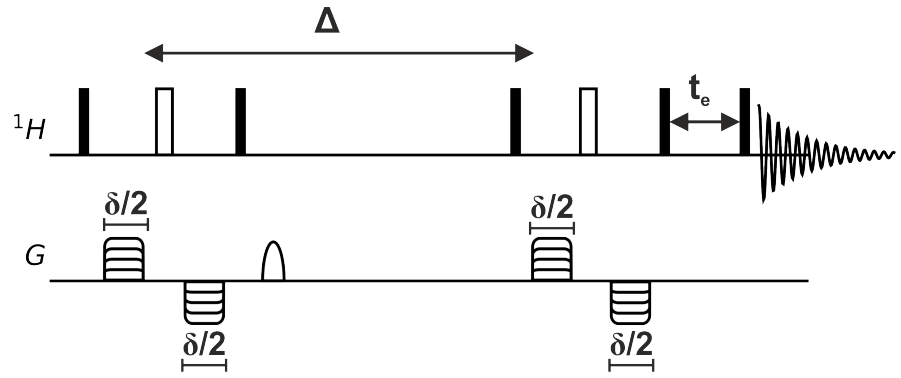

Figure 4.6: Graphical representation of the **BPLED** pulse sequence.

Dissecting the term **BPLED**, three modification are made. Firstly, both encoding and decoding gradient pulses are changed to so called bipolar gradient pulses [45; 46]. Instead of having one gradient the pulse is split into two pulses with half length $\left({}^{\delta}/_{2}\right)$. Additionally, they are of opposite sign with a 180° pulse in the centre. With the pulse power staying the same and total pulse length unchanged the decoding and encoding effects remain.
The benefit of the implementation of bipolar gradients is that the lock signal is less affected. Pulsed field gradients dephase the deuterium magnetisation as well, therefore the lock signal will shift. Bipolar gradients refocus both proton and deuterium and ultimatly supress possible frequency shift artefacts. In addition, bipolar gradient pulse sequences are beneficial when studying systems with a slow rate of exchange [47].

The next term is longitudinal. After the first gradient pair a 90° pulse is applied, which is called a stimulated echo and was intoduced by Hahn [37]. Before the 90° pulse

the magnetisation is in the transversal plain, so this pulse flips the spins along the z axis. Therefore, the pulse sequence is called longitudinal. The reason for having the magnetisation along z and not in the xy plane is the effect of coupling evolution. As described in 4.2 the Hamiltonian of coupling in the weak coupling limit is $\hat{H} = 2\pi J_{12}\hat{I}_{1z}\hat{I}_{2z}$. Having the magnetisation aligned along the z axis during the diffusion delay has no effect on the coupling evolution. This improves the DOSY measurement of spin-spin coupled system. Moreover, having the magnetisation longitudinal also leads to the relaxation being longitudinal. With T_1 being longer than T_2, especially for larger molecules, the application of diffusion measurement expands to larger molecules. This enables the diffusion delay Δ to have a longer duration.
The downside of the stimulated echo is that a 90° pulse only flips half the translational magnetisation along z. The remaining half of the spins are unaffected by the pulse, because an x-pulse has no impact on x-magnetisation, same holds true for the y-magnetisation when a y-pulse is applied. Moreover, to suppress unwanted modulation of preserved translational magnetisation an additional gradient has to be implemented. These are often called crusher, or spoil gradients that dephase the spins in the xy-plain.

The last improvement of the DOSY lies in the Eddy Current Delay [48]. Unwanted currents within the spectrometer's probe give rise to spectral distortion. These distortions are removed by a 90° pulse that flips the magnetisation along the z-axis, followed by a short delay for the currents to fade. After the delay the spins are fliped back by a subsequent 90° pulse into the transversal plain for acquisition.

4.6.2. **Double Stimulated Echo**

The next part of this thesis adresses a concept of molecular movement, that is different from diffusion. Unlike the random motion of diffusion, convection describes a constant flow of the solvent. The cause of convection is thermal flow caused by temperature gradients in the sample [49; 50]. This effect is unmonitored by the **BPLED** sequence, therefore an addition is necessary. Similar to diffusion, convection has an effect on the signal attenuation. To monitor diffusion, the effect of convection has to be cancelled [51]. The suppression of convection is crucial in order to obtain exact diffusion coefficients [52]. This might be achieved physically, like reducing the sample diameter [53]. But with clever application of the so called double stimulated echo (**dSTE**) this is achieved unambiguously with a simple extended pulse sequence [54; 55; 56].

To describe the effect of convection we have to discuss the amplitude attenuation. We neglect the effect of relaxation and focus on the gradient dependent decay of the signal. Equation 4.52 describes the gradient effect $f_G(t)$ derived from the Bloch-Torrey equation [23]:

$$f_G(t) = exp\Big[- D\gamma^2 \int_0^t \Big(\int_0^{t'} g^*(t'') \Big)^2 d(t') \Big] \cdot \Big[i\gamma v \gamma^2 \int_0^t \Big(\int_0^{t'} g^*(t'') \Big) d(t') \Big] \tag{4.52}$$

D is the diffusion coefficient, v is the flow velocity and g^* denotes the effective gradient. It is defined as $g^* = p(t) \cdot g(t)$ where $p(t)$ is the coherence order and $g(t)$ the magnetic field gradient at time t. The first term describes the diffusion attenuation. The second term in equatin 4.52 describes the flow-velocity-dependent phase factor. In order to compensate the effect of convection the second term has to become zero. This is achieved by the use of gradients $g(t)$ and coherence order pathway $p(t)$. The pulse sequence leads to:

$$\int_0^t g^*(t')t'dt' = 0 \tag{4.53}$$

It cancels the first-order velocity terms, but the second-order diffusion terms are unaffected. Therefore the experiments compensates the effect of convection [57].

The pulse sequence of the **dSTE** is graphically represented in figure 4.7. Instead of one diffusion delay Δ the sequence is split in two $^{\Delta}/_{2}$ segments. Both stimulated echo blocks contribute to the diffusion attenuation, but the flow-velocity is cancelled. This is achieved by applying coherence order pathways that fulfill equation 4.53.

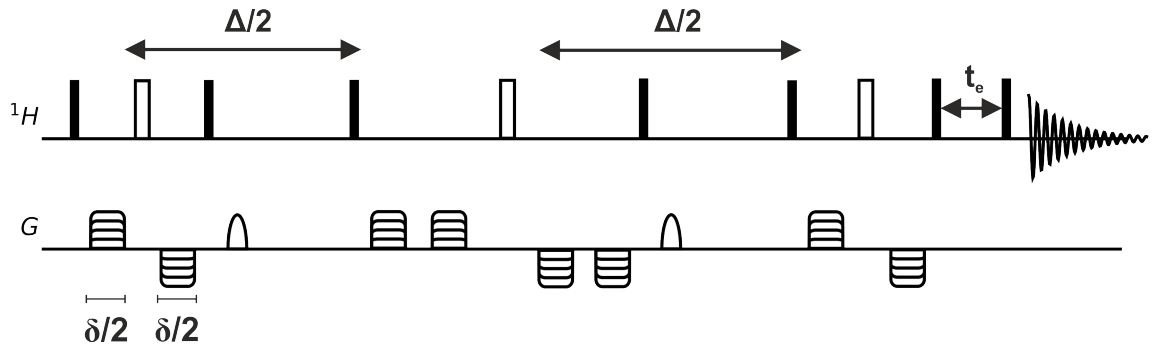

Figure 4.7: Graphical representation of the **dSTE** pulse sequence.

4.7. Macromolecular Systems

In this section the reader will get a brief overview on macromolecules. Starting with the basic concept of polymer chemistry we will outline the field of application. The development of highly defined polymers generate nanostructures with well established functionality [58]. In this work the concept of single-chain folding is investigated as it opens a pathway to mimic biomolecules such as peptides.

4.7.1. Polymers

Polymers are long molecule chains that are covalently connected by specific repeating units. These long chains have unique properties and are an omnipresent class of material. Therefore, polymers are targeted by scientists to generate novel nano architectures. The synthesis of artificial polymers is a wide field of methods [59].

The development of novel macromolecular systems have numerous application. The progress in polymer studies tackles many important issues, for instance climate change,

or the energy crisis. In order to find new sustainable energy solar cells are of pivitol role. New polymer solar cells show very promising solution. They have good mechanical flexibilty, low cost, high degree of stability and a thin active layer [60]. Additionally, polymeric systems have many applications in energy storage technologies [61]. Moreover, polymer electrolytes are facilitated as a safe alternative to Lithium batteries [62; 63]. Hyperbranched polemers have been developed to work as organic semiconductors [64]. Polymers can make a contribution to the climate crisis as studies find a way to capture CO_2 and perform an electrocatalytic reduction [65]. Furthermore, polymers are essential in biomedicinal tasks with their customisable functionality [66].

Polymers are accessible in many synthetic pathways like step growth, chain growth, template design, controlled monomer addition and so on. A listing of all methods is beyond the scope of this work. As an example of polymerisation the so called Atom Transfer Radical Polymerisation (ATPR) is illustrated. It delivers well-defined polymeric structures [67]. The general mechanism of ATPR is that the propagating chains are reveribly trapped with a halide by a metal complex. It generates dormant species that prevents termination of the polymer chain [68; 69].

4.7.2. **Single Chain Folding**

With the advent of highly controlled polymer synthesis scientists are aiming to control the physical properties as well. In nature precisely defined folding of polymers form functional nanostructures that fulfill many tasks. Consequently the goal is to mimic biological systems in their tertiary structure, such as peptides and proteins. Therefore, the rather unstructured synthetic polymer chain is modified in order to have specific conformational functions [70]. These molecules are called single chain nanoparticle (SCNP). This is achieved by folding points, which are often introduced by post modification. In literature there are various folding motifs [71; 72]. The concept range from covalent cross-linking, non covalent cross-linking to metal complexation. Having many conformational triggers the field of single chain particles introduces numerous innovations. Systems with different orthogonal self-assembly groups [73], or of photo-induced folding motifs [74] illustrate the possibility for various applications. SCNP's are used in nanomedicine to release active components at predefined location in cancer cells [75; 76].

A alternative approach to the single chain nanoparticle research is formation of foldamers. The idea was first introduced by Gellman and coworkers [77]. Like SCNP's foldamers aim to mimic the conformational function of biological polymers like proteins, or RNA. Here, the macromolecular systems contain polypeptides, or polynucleotides. This approach utilises the intrinsic secondary structural preferences of the polymer chain. The structures are self assembled and are mediated by a network of hydrogen bonds. The foldamer consists of compact well ordered helices. The field of foldamers developed many applications, such as drug delivery[78; 79].

Much effort has been put into the design of novel synthetic macromolecules. With the manipulation of the conformation of these polymer chains a variety of application and novel nano architectures has been developed [80; 81]. The contribution of these systems

will lead to the development of modern technologies in future [82].

4.7.3. **Dispersity**

The process of polymerisation reaction follows statistical principles. Even with a high degree of control the synthesised macromolecules are never homogeneous in size. Consequently molecular weights are distributed. The molecular weight distribution (MWD) is a common property in polymer physics as it gives information about the quality of the synthesis. It is given as the dispersity index Đ, formaly it was called the polydispersity index (PDI) [83]. With regard to the system the dispersity describes the degree of branching, the composition of copolymers, or the microstructure. The dispersity is given by ${}^{M_w}/_{M_n}$. The number average is M_n and M_w is the weight average. It derives from the analysis of size exclusion chromatography (SEC) [84; 85]. SEC separates molecules according to their size in a column filled with porous packing.
Alternatively the dispersity of the polymer samples can be measured indirectly with diffusion ordered NMR spectroscopy. The separation of the different polymer chains results from the different diffusional rates. However the weight is indirectly linked to the polymer diffusion. As 1D NMR spectra are often a measure to monitor the success of the synthesis, the experimenter can record an additional DOSY without extensive sample preparation. The mathematical and experimental background is described in the works of Guo [32; 2] and Roeding [86].

The polymer chain length follows a weight distribution which manifests in distribution of diffusion coefficient. Consequently diffusion follows a probability distribution $P(D)$. Therefore the signal attenuation is described by integral over different exponential decays:

$$I(k) = I_0 \int_0^\infty P(D)\ exp(-kD)dD \tag{4.54}$$

The probability function is unknown, however the gamma distribution describes the distribution quite accurate [87]. The gamma distribution is give with:

$$P_G(D;\kappa,\theta) = D^{\kappa-1}\frac{exp(-D/\theta)}{\Gamma(\kappa)\theta^\kappa} \tag{4.55}$$

Γ is the gamma function, κ is the so called shape parameter and θ is called the scale parameter. It should be mentioned that the gamma distribution is described alternatively by the rate α instead of the shape κ with $\alpha = {}^1/_\kappa$. In this work we continue with the nomenclature of shape and scale. Next we replace $P(D)$ in equation 4.54 with equation 4.55:

$$I(k) = I_0(1 + k\theta)^{-\kappa} \tag{4.56}$$

We use the expression of $\langle D \rangle = \kappa\theta$ and $\sigma_G = \sqrt{\kappa\theta^2}$. The mean self-distribution is given by $\langle D \rangle$ and σ_G is the standard deviation. Replacing γ and θ with $\langle D \rangle$ and σ_G leads to:

$$I(k) = I_0\Big(1 + k\sigma_G^2/\langle D \rangle\Big)^{-\langle D \rangle^2/\sigma_G^2} \tag{4.57}$$

Equation 4.57 describes the signal attenuation distribution with tha gamma model. In order to translate the diffusion distribution into the weight distribution the correlation is given by $D = KM^{-\alpha}$ with K and α being scaling parameters [87]. Ultimately the dispersity measured with diffusion ordered spectroscopy is given by:

$$Đ = \left(1 + \frac{\sigma_G^2}{\langle D \rangle^2}\right)^{1/\alpha^2} \tag{4.58}$$

Equation 4.58 enables the spectroscopist to aquire the dispersity indices of polymer samples with DOSY experiments. Consequently the polymers dynamics can be studied with NMR techniques. As such, the importance of DOSY in macromolecular systems has grown in the last decades [88; 89; 90].

5. DOSY Analysis of Macromolecular Systems

DOSY measurements have a wide range of application. As diffusion gives direct correlation to the molecular size, or molecular weight, DOSYs are frequently used in macromolecular systems and nanotechnologies [91; 92; 93]. The analysis of molecules with many spins, that often have indistinguishable chemical shifts can be quite combersome. Whereas DOSY monitors physical properties, such as mobility, or size, without the need of a high degree of resolution [94; 95]. This is beneficial for monitoring various folding motifs [96] and conformational triggers [97] which is descriped in this chapter.

5.1. SCNP with Spinlabel

As a precursor a polystyrene polymer was functionalised *via* the combination of atom transfer radical polymerisation (ATRP) and direct bromine-azide exchange reaction. Next, an alkyne functional polystyrene polymer featuring an additional hydroxyl functionality, was synthesised by ATRP and connected using copper catalysed azide-alkyne cycloaddition (CuAAc). Furthermore, an alkyne an OH functional Hamilton wedge (HW) group was tethered by CuAAc. This precursor single-chain nanoparticle has the α,ω cyanuric acid/Hamilton wedge folding motif, which is discussed in sections 5.1 and 5.4 of this thesis [98]. The single chain nanoparticles were synthesised in the group of Prof. Christopher Barner-Kowollik (Institut für Technische Chemie und Polymerchemie).
In this work a single-chain nanoparticle modified with a spin label has been studied. The spin label of choice is 4-carboxy-2,2,6,6-tetramethylpiperidine 1-oxyl (4-carboxy TEMPO) and is placed next to the Hamilton wedge functional group. In figure 5.1 the chemical structure is illustrated. In addition, the same SCNP has the TEMPO spin label replaced by methyl group. For brevity reasons the nomenclature is SCNP-TEMPO for the Hamilton wedge/ cyanuric acid polymer with spin label attached. Due to the termination of the free electron by a methyl group the polymer without the spin label is called SCNP-MeTrap.

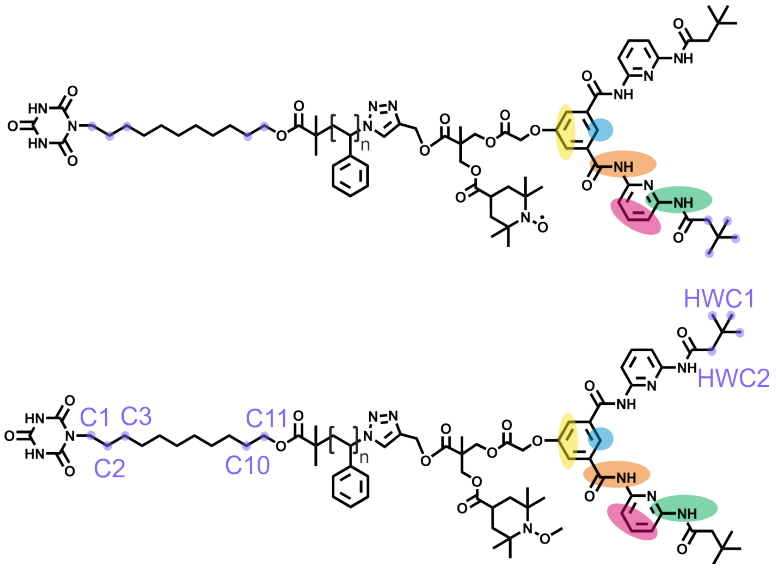

Figure 5.1: Chemical structure of the Hamilton wedge/ cyanuric acid with the TEMPO spin label attached (top). In addition, the free electron was removed by the methylising the spin label (bottom) which depletes the paramagnetic group. This way the effect of paramagnetic relaxation enhancement can be visualised. The effected hydrogen spins of the Hamilton wedge are colour coded. The affected carbon spins are visualised by purple dots.

To monitor the folding behaviour of the α,ω cyanuric acid/Hamilton wedge folding motif DOSY measurements were performed. In its diluted form, the cyanuric acid moiety is linked via hydrogen bonds to the Hamilton wedge terminus. Therefore the conformation of the molecule should be compact. Consequently the diffusion of the nanoparticle should be elevated. Adding a protic solvent, such as methanol, should disrupt the hydrogen bonds and the cyanuric acid end leaves the Hamilton wedge pocket. In this case the molecule has a larger spatial dimension which reduces the diffusion.

The DOSY measurements were performed at a 600MHz spectrometer with cryo probe for enhanced sensitivity. In order to have single chain diffusion only the concentration af the sample needs to be low. With low concentration the cyanuric acid is linked intramolecularly to the Hamilton wedge. To make sure to have sufficiently low concentration and avoiding intermolecular binding of the SCNP, the sample was diluted until we could not see any change in the diffusion coefficient. In this work the concentration was set to $c = 0.49 mol/_l$ with 8.8mg in 600μl CD_2Cl_2. The BPLED pulse sequence was applied with a linear gradient ramp with 32 points starting from 2% to 98%. To have sufficient signal to noise the number of scans was set to 8. To recover the longitudinal magnetisation for maximum signal the relaxation delay was set 4s. The diffusion delay was set to $\Delta = 100$ms with the gradient length being $\delta = 2400\mu$s. The temperature was adjusted to 300K.

The DOSY fits are shown in figure 5.2 applying the Stejskal-Tanner Equation. After completing the measurement of the SCNP-TEMPO sample we added 5μ l of deuterated methanol. The folded SCNP-TEMPO is plotted in blue and the unfolded polymer in

red. In the logarithmic plot it is clearly visible, that the diffusion varies in the folded and unfolded state.

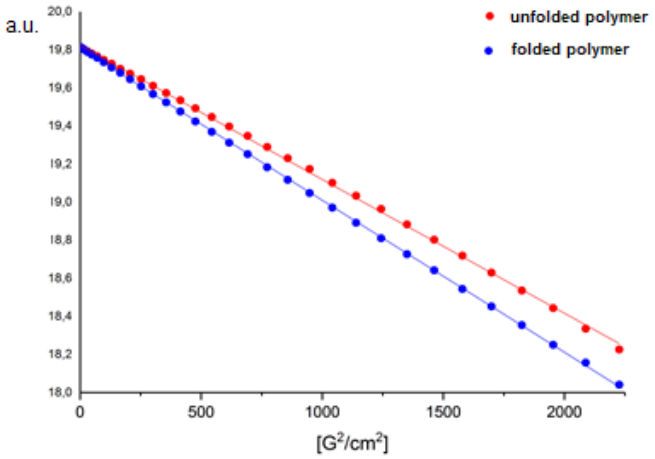

Figure 5.2: DOSY fit of SCNP-TEMPO polymer. The circles represent the experimantal data points. In its diluted form (blue) the polymer is folded. Adding methanol unfolds the polymer (red).

The results of the DOSY analysis are illustrated in table 5.1. To identify the folding of the single-chain polymer the diffusion coefficients are compared. The folded polymer's diffusion rate is $1.69 \cdot 10^{-10} \mathrm{m^2 s^{-1}}$ and it drops to $7.14 \cdot 10^{-11} \mathrm{m^2 s^{-1}}$ after adding methanol. Calculating the hydrodynamic radii with the help of the Stokes-Einstein equation the folded polymer's radius of 3.01nm is increased to 7.33nm. So in conclution, adding a protic solvent to the Hamilton wedge/ cyanuric acid folding motif disrupts the hydrogen bonds and the single-chain nanoparticle is elongated. So the incorporation of the Hamilton wedge/ cynanuric folding scheme acts as a triggerable function that allows to change the polymer's conformation.

Table 5.1: Results of the DOSY measurement of the SCNP-TEMPO and the SCNP-TEMPO with methanol. The Diffusion coefficients are calculated with the Stejskal-Tanner euquation. The hydrodynamic radii are calculated with the Stones-Einstein equation.

	$D[\mathrm{m^2 s^{-1}}]$	R_0 [m]
SCNP-TEMPO	$1.69 \pm 0.01 \cdot 10^{-10}$	$3.01 \pm 0.02 \cdot 10^{-9}$
SCNP-TEMPO + MeOH	$7.14 \pm 0.03 \cdot 10^{-11}$	$7.33 \pm 0.03 \cdot 10^{-9}$

In addition to the analysis with DOSY the spin label is utilised to monitor the folding behaviour. With the spin label being in the vicinity of the Hamilton wedge and cyanuric acid the effect on the spins can be observed [99; 100]. Electrons are fermions and have an intrinsic spin of $s = {}^1/_2$. As electrons are either bound covalently or paired freely the spin

effectively vanishes, because the orbitals are filled with two electrons with different spin orientation, i.e. $m_s = +1/2$ and $m_s = -1/2$. Now with a free radical this concept colapses and the electron spin is preserved. Consequently, the TEMPO moeity has paramagnetic properties that interact with all surrounding spins. Having a strong paramagnetic centre in the proximity of nuclear spins accelerates their relaxation rates [101]. This results in linebroadening of the corresponding signals in the NMR spectrum. This effect used for structural elucidation and is called paramagnetic relaxation enhancement (PRE)[102].

In order to monitor the effect of the spin tag on the neighbouring spins the signals of the single chain nanoparticle have to be assigned. Therefore a number of 1D and 2D spectra were recorded. In addition to ^{1}H 1D spectra especially ^{13}C spectra are important in structure analysis in organic molecules. To examine correlation between each spin additional COSY, TOCSY, HSQC, NOESY and HMBC spectra were recorded. The measurements were performed at 600MHz with a cryo probe for sensitivity improvement. The sample temperature was set to $T = 298$K. With the help of the COSY spectrum geminal couplings are used to identify neighbouring proton signals. Moreover the TOCSY connects ^{1}H spin systems. Additionally, the NOESY determines ^{1}H signals in spatial vicinity. Next heteronuclear coupling are utilised to identify the carbon backbone. The HSQC cross signals signify the carbon atom the hydrogen is bound and with HMBC further carbon atoms can be linked to the specific ^{1}H signal. With all these information the structure of the Hamilton wedge moeity can be constructed to measure the effect of paramegnetic relaxation enhancement on surounding spins.

The examination of the spectra is shown in table 5.2. Of interest are the proton signals of the Hamilton wedge. As shown in figure 5.1 two nitrogen bound protons are present in the Hamilton wedge terminus. They are called NH1 and NH2. Additionaly five aromatic hydrogen signals can be distinguished, HW1, HW2, HW3, HW4 and HW5. These signals are located in the downfield region. Lastly the terminal *tert* butyl group and its neighbouring methylene group have ^{1}H signals in the high field region. In anticipation of the corresponding carbon signals the nomenclature of methylene and *tert* butyl group HWC2 and HWC1 respectively (see figure 5.1).

Moreover, the NMR signals in the cyanuric terminus are of interest as the folding mechanism would cause the cyanuric acis part to be close to the spin label. As described in figure 5.1 five carbons are distinguished. C1, C2 and C3 are positioned next to the cyanuric acid terminus. C11 and C10 are on the opposite side of the alkane chain.

Table 5.2: NMR analysis of SCNP-MeTrap. $\delta(^1H)$, $\delta(^{13}C)$ and corresponding cross signals are given in ppm. The brackets signify that the crosspeak was hardly visible due to high noise level. Some cross peaks were not assigned due to signal overlap. *:^1H signals that correspond to the ^{13}C signals.

	^1H	(^1H,^{13}C)HSQC	(^1H,^1H)COSY	(^1H,^1H)TOCSY	(^1H,^1H)NOESY	(^1H,^{13}C)HMBC
NH1	9.92	-	-	-	8.29/(7.72)/(8.04)/(9.49)	112.19/164.98
NH2	9.49	-	-	(2.39)	2.39/(8.17)/(9.92)	111.46/171.39
HW1	8.29	117.70	-	7.72	9.92	118.51/164.98
HW2	8.17	111.46	7.87	7.87/8.04	(9.49)	112.19
HW3	8.04	112.19	7.87	7.87/8.17	7.87	111.46/141.11
HW4	7.87	141.11	8.04/8.17	8.04/8.17	8.04/8.17	112.19/150.60
HW5	7.72	118.51	-	8.29	(9.92)	118.51/136.2/158.50/164.98
HWC2*	2.39	49.98	-	(9.49)	9.49/(1.15)	29.51/171.39
HWC1*	1.15	29.51	-	-	(2.39)	49.98
C1	3.93	42.15	1.72	1.39/1.72	overlap	28.35/149.60
C2	1.72	28.35	3.93	overlap	overlap	overlap
C3	1.39	25.90	overlap	overlap	overlap	28.35
C10	2.11	31.22	5.18	5.18	overlap	overlap
C11	5.18	58.52	2.11	2.11	overlap	141.80/171.82/(31.22)

The most important resonances are displayed in figure 5.3. To help visualise the effect of the TEMPO spin label on these signals the SCNP-TEMPO (red) polymer is compared to the SCNP-MeTrap (blue). In both cases the cyanuric acid is linked to the Hamilton wedge moiety and therefore the spin label should affect both termini. Starting with the evaluation of SCNP-MeTrap ^{1}H spectra. The seven signals in the downfield region can be assigned to the signals of the Hamilton wedge. Signal NH1 (orange) at 9.92ppm and signal NH2 (green) at 9.49ppm are the nitrogen bound protons. The signals HW1 (yellow) at 7.72*ppm* and HW5 (cyan) at 8.29ppm are located at the central phenyl ring. The remaineing signals (magenta) HW2 at 8.17ppm, HW3 at 8.04ppm and HW4 at 7.87ppm are the carbon bound hydrogen signals in the Hamilton wedge arm. The cross signals in the COSY, NOESY and TOCSY spectra verify these finding. Moreover, with help of TOCSY and NOESY the terminal methylene (HWC2) and *tert*-butyl (HWC1) group are assigned as well with frequencies at 2.39ppm and 1.15ppm, respectively.

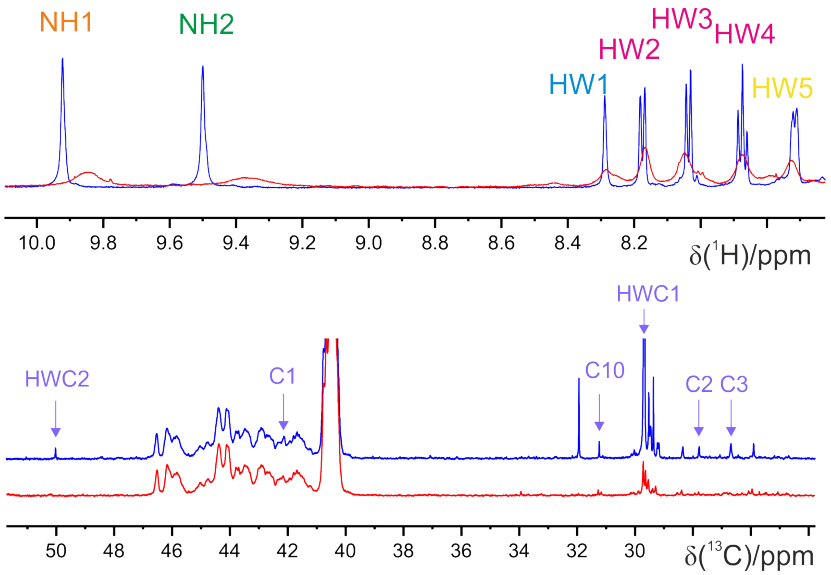

Figure 5.3: Comparison of SCNP-TEMPO (red) and SCNP-MeTrap (blue). On top the ^{1}H spectrum in the downfield region. On the bottom the ^{13}C.

With heteronuclear correlation spectra at hand the ^{1}H signals help identify the carbon signals. As mentioned above the names HWC1 and HWC2 refer to the carbon position. The methylen carbon (HWC2) signal is at 49.98ppm and the *tert* butyl (HWC1) signal is at 29.51ppm. Examining the carbon signals of the alkane chain of the cyanuric acid terminus the investigation of the 2D spectra reveals C1 at 42.15ppm. Its corresponding ^{1}H signal is at 3.93ppm, which is to expected of a CH_2 group next to a nitrogen. The HMBC signal of 149.60ppm confirms this, as it is typical for amids. With additional correlation of HMBC-, COSY- and TOCSY spectra the carbon atoms C2 and C3 are assigned. C2 has carbon resonance at 28.35ppm and has proton signal at 1.72ppm. C3 has the carbon signal at 25.90ppm and hydrogen signal at 1.39ppm. Additionally, C10 and and C11 are characterised at 58.52ppm/5.18ppm and 31.22ppm/2.11ppm respectively, utilising homo- and heteronuclear correlation spectra.

After the successful signal assignment of the SCNP-MeTrap polymer we can apply this knowledge and investigate the SCNP-TEMPO polymer. Both polymers only vary in the free electron. Therefore all signals should approximately remain at the same position in the spectra. On the other hand the free electron spin now effects all surrounding spins. This is clearly visible in the comparisons of the 1D spectra in figure 5.1. The proton signals of the SCNP-MeTrap (blue) are narrow and the splitting due to scalar coupling are visible. In the ^{1}H spectrum of SCNP-TEMPO these lines are broadened. Moreover the splitting of signals HW2, HW3, HW4 and HW5 vanishes. This is due to the paramagnetic relaxation enhancement of the TEMPO radical. The short relaxation leads to linebroadening which ultimately reduces the resolution. In addition, this effect is visable in the ^{13}C spectra. It shows the carbon signals of HWC1, HWC2, C1, C2, C3 and C10 in a range from 24ppm to 50ppm. Although C1 and HWC1 are overlapping, the signals are distinguishable. All other afformentioned signals are isolated. Investigating the carbon spectrum of SCNP-TEMPO the signals of the Hamilton wedge terminus and of the cyanuric acid moiety vanish.

In conclution, the spin label affects the spins in the Hamilton wedge terminus as well as the spins in the cyanuric acid terminus. Therefore the TEMPO moiety is in proximity to both termini, which provides evidence for the folding mechanism. The spin tag investigation and the DOSY measurement of the single chain nanoparticle could succesfully verify the folding mechanism of the Hamilton wedge/ cyanuric acid motif.

5.2. Self-reporting and refoldable profluorescent single-chain nanoparticles

After investigating the folding behaviour of a single chain nanoparticle with the Hamilton wedge/cyanuric acid we introduce the polymer folding with a photoactive crosslinker. In figure 5.4 the reversible folding and unfolding mechanism is illustrated. The folding points are 4-carboxy-2,2,6,6-tetramethylpiperidine-1-oxyl (4-carboxy-TEMPO), which are photochemically crosslinked [103]. The polystyrene backbone was prepared by nitroxide mediated polymerisation (NMP) with a combination of well defined ratios of styrene and 4-(chloromethyl)styrene (CMS) [104; 105; 106]. The synthesis was done in the group of Prof. Christopher Barner-Kowollik (Institut für Technische Chemie und Polymerchemie). The CMS units are the precursors for attaching the TEMPO moiety [107]. In order to trigger the intramolecular collaps the bifunctional photo crosslinker **1** (2-hydroxy-40-(2-hydroxyethoxy)-2-methylpropiophenone) was utillised with external UV radiation (= 320nm)[108]. The unfolding of the SCNP was targeted with metachloroperbenzoic acid (mCPBA) [109].

Figure 5.4 describes the reversible folding mechanism. The initial unfolded form of the single chain nanoparticle **P4'** is irradiated with UV light (= 320nm) which leads to covalent crosslinking with **1**. The resulting folded polymer **P9** is unfolded by mCPBA. Analog the unfolded SCNP **P10** and **P11** are formed with identical procedure. To monitor the folding and unfoldung process many analytical tools were utilised [3]. The existence of unpaired electrons enables the measurement of TEMPO with Electron Paramagnetic Res-

onance (EPR) spectroscopy. **P4'** and **P10** have measurably higher signals than **P9** and **P11**, which confirms the crosslinking with the TEMPO terminus. An additional effect of the TEMPO group is that it quenches the luminescence of the aromatic backbone. After the crosslinking process the luminescence is recovered and therefore the polymer is capable of emitting light. Consequently, the folding can be qualitatively monitored by its light emitting properties caused by the folding behaviour. However, the spatial conformational change is not monitored by these two methods. Therefore, we measured the diffusion of the different states of the polymer folding with DOSY [110].

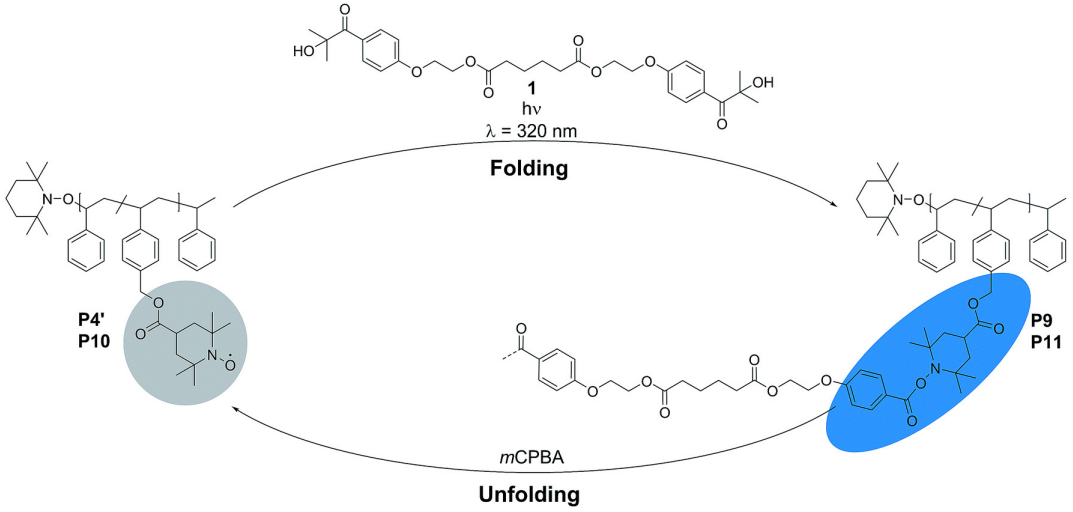

Figure 5.4: Folding and unfolding using UV irradiation mediates thr reversible chemical crosslinking of the SCNP.

DOSY spectra were performed at $T = 298$K. All polymers were solved in deutarated dichloromethane. For the unfolded polymers P4' and P10 the diffusion delay was set to $\Delta = 100$ms with a gradient duration of $\delta = 3000\mu$s. To optimise the diffusion attenuation on the folded polymers the parameters were adapted. The gradient length was set to $\delta = 2400\mu$s and the diffusion time was set to $\Delta = 80$ms. Additonally, the hydrodynamic radii were calculated with the Stokes-Einstein equation with the assumption of a spherical conformation of the single chain nanoparticles.

Table 5.3: Summary of the DOSY experiments. The unfolded polymers P4' and P10 are compared to the folded polymer of P9 and P11.

	D $[10^{-10}\mathrm{m}^2\mathrm{s}^{-1}]$	R_0 $[10^{-9}\mathrm{m}]$
P4'	3.1	3.4
P9	4.0	2.6
P10	3.0	3.5
P11	3.6	2.9

The summary of the DOSY results are collated in table 5.3. With the calculated hydrodynamic radii the folding behaviour is evidently monitored. The initial SCNP **P4'** features an expanded form with $R_0 = 3.4$nm. Adding the bifunctional photolinker and

applying UV-light causes the polymer to collaps. The folded SCNP **P9** has a hydrodynamic radius of $R_0 = 2.6$nm. After applying mCPBA the single chain nanoparticle **P10** prolongs to a radius of $R_0 = 3.5$nm. Finally the polymer **P11** is collapsed again due to the photoinduced intramolecular folding to $R_0 = 2.9$nm. In summary, the diffusion measurement of the SCNP proves its folding mechanism. Moreover, the reversability was monitored as well.

5.3. Photoswitchable Block Copolymers Based on Main Chain α-Bisimines

In this section we present a diblock copolymer with an photoswitchable α-bisimine unit. With the α-bisimine moiety the single chain polymer's conformation can be targeted reversibly. The concept of functionalising macromolecular systems to alter the conformation and dynamic with light irradiation found application in nanomedicine and nanotechnology [111; 112; 113]. Figure 5.5 illustrates the reversible photoswitch method. In its initial condition the α-bisimine units are in the (Z,Z)-configuration. After irradiation with $\lambda_{max} = 254$nm the configuration changes to (E,E) [114]. Consequently, the configuration of the block coplolymer changes. The isomerisation process is reversible and therefore the configuration is reversible as well.

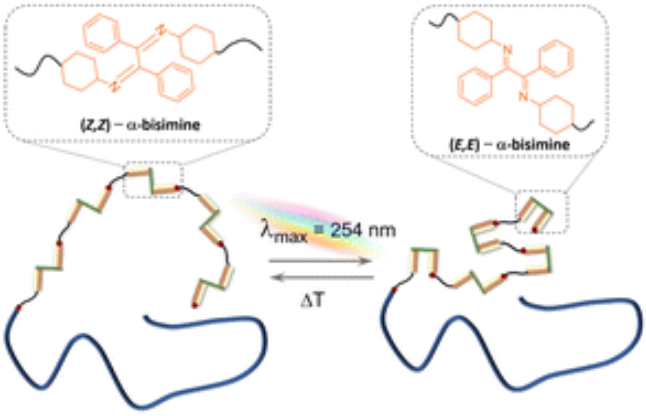

Figure 5.5: Concept of the conformational change with the α-bisimine unit with UV irradiation.

The scheme of the synthesis is described in figure 5.6. The block-copolymer consists of static polystyrene and dynamic ADMET group (acrylic diene metathesis). The desired linear diblock copolymer is catalysed with Hoveyda–Grubbs 2nd generation catalyst, based on the highly selective cross-metathesis reaction between the acrylate and the alkene group. The synthesis was done in the group of Prof. Christopher Barner-Kowollik (Institut für Technische Chemie und Polymerchemie).

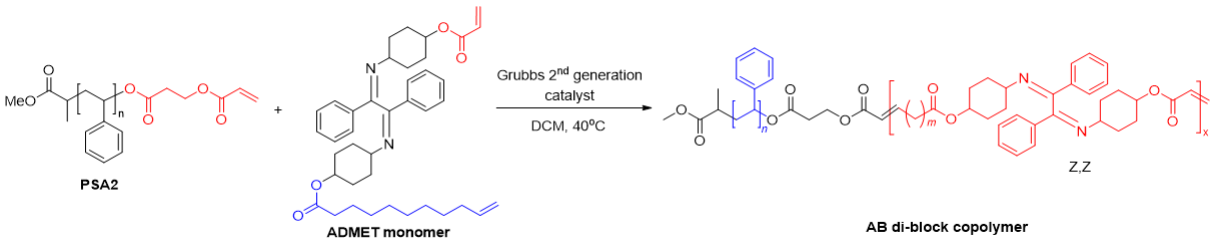

Figure 5.6: Synthesis or di-block copolymer with the light sensitive ADMET block.

The aim of the diffusion measurements is to observe the formation of a block-copolymer as desribed above [115; 116; 117]. Therefore two polystyrene blocks with different chain lengths act as precursors. $PS_{70}A2$ was funtionalised with three different ADMET blocks and $PS_{115}A2$ was functionalised with two ADMET termini. Starting with the $PS_{70}A2$ polymer.
The first copolymer was crafted with five ADMET groups forming the block copolymer $PS_{70}ADMET_5$. In the next step the polystyrene block was linked to seven ADMET units, hence the formation of $PS_{70}ADMET_7$. The implementation of 34 ADMET units was performed with the molecule of $PS_{70}ADMET_{34}$. Analog to the $PS_{70}A2$ polymer, the precursor $PS_{115}A2$ was modified with ten ADMET units froming $PS_{115}ADMET_{10}$. Additionally the $PS_{115}A2$ unit was attatched by 36 ADMET monomers in order to get the bolck colpolymer of $PS_{115}ADMET_{36}$. The synthesis scheme prepared precise copolymers, with a static block and a block with controlled chain length of ADMET units.

In order to compensate the effect of convection, the double stimulated echo (**dSTE**) sequence was used. The **dSTE** experiments were performed at $T = 300$K. All polymers were solved in deutareted chloroform. To have sufficient sensitivity, all DOSY spectra were performed with 16 scans. Additionally, 32 gradient points were measured to monitor the diffusion of the block-copolymers. The results of the DOSY experiments are given in figure 5.4. The precursor polymers were each $PS_{70}A2$ and $PS_{115}A2$ and are compared to their functionalised polymers. In both cases the addition of the ADMET block leads to a reduction of the diffusion coefficient. Moreover it monitors the diffusion relative to the length of the ADMET part. The more ADMET monomers are linked to the α-bisimine moiety, the lower the diffusion rate gets.

Table 5.4: Summary of results for the copolymer experiments.

	D $[10^{-10}\mathrm{m^2s^{-1}}]$
$PS_{70}A2$	1.31
$PS_{70}ADMET_5$	1.16
$PS_{70}ADMET_8$	0.94
$PS_{70}ADMET_{34}$	0.79
$PS_{115}A2$	1.15
$PS_{115}ADMET_{10}$	0.98
$PS_{115}ADMET_{36}$	0.67

The DOSY analysis confirms the formation of the block-copolymers. Therefore the synthesis control of this copolymer is demonstrated. Moreover, the diffusion coefficient monitors the relative growth of the added blocks. This approach enables the analysis nano architectures synthesis, that can be conformationally altered by light.

5.4. Controlling SCNP folding by orthogonal Metal complexation and hydrogen bonding

After analysing the folding behaviour of one folding motif this section expands to a more complex system. Using the aforementioned concept of folding *via* α,ω cyanuric acid/Hamilton wedge an orthogonal folding mechanism is introduced. Metal complexation is an independent folding point within the single-chain nanoparticle. The synthesis was done in the group of Prof. Christopher Barner-Kowollik (Institut für Technische Chemie und Polymerchemie).

Starting with the precursor SCNP described in section 5.1, two phoshene moieties were introduced to the polymer. The first step is by esterification with 11-bromoundecanoic acid. In the second step the triphenylphosphene moieties were linked to the polymer.
In figure 5.7 the complete molecular structure as well as the concept of the dual folding single-chain nanoparticles are illustrated. The red circle with its corresponding black box represents the aforementioned α,ω cyanuric acid/Hamilton wedge motif. The green diamond with the purple counterparts displays metal complexation folding point. The first folding motif is mediated by hydrogen bonds, that can be disrupted by a protic solvent like methanol as shown in section 5.1. The newly incorporated side chains have to be linked by metal complexes. In this work the metal induced folding was performed with dichloro(1,5-cyclooctadien)palladium(II) [118].

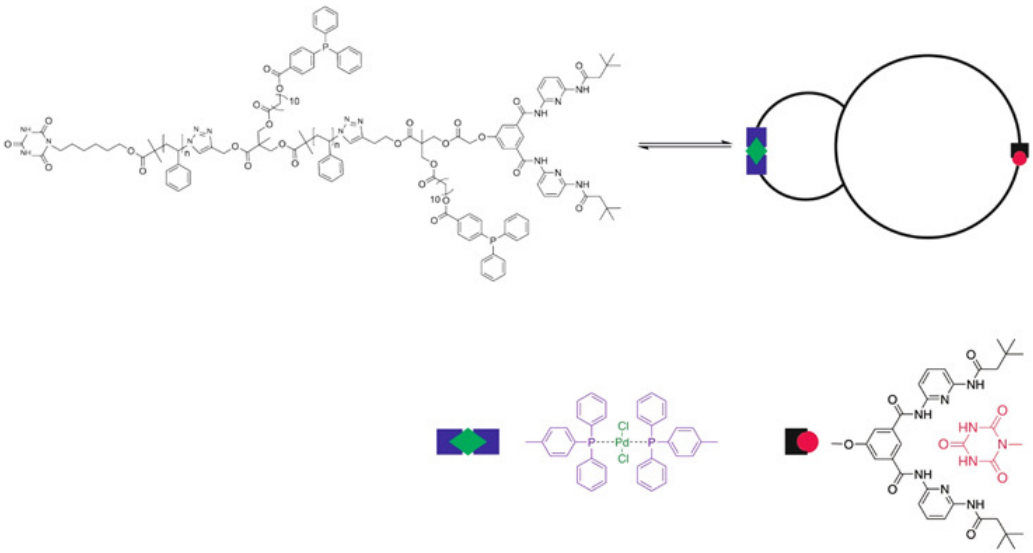

Figure 5.7: Molecular structure of orthogonal folding motif single chain nanoparticle. The black and red circle represent the Hamilton wedge cyanuric acid folding point. Purple and green signifies the Pd induced metal complexation moeity.

Having two orthogonal folding motifs it concludes that the polymer has four different conformations. To differentiate between these states the SCNPs are called **SCNP-d1** and **SCNP-d2**. **SCNP-d1** describes the situation without metal complexation. In this conformation the triphenylphosphene side chains are not linked together. The α,ω cyanuric acid/Hamilton wedge folding point is uneffected and can be opened with methanol. Consequently, **SCNP-d2** is the polymer with the Pd(II) complex binding the two triphenylphosphene moieties. The ^{31}P spectra in figure A.7 verify the metal complaxation of Pd with the triphenylphosphene terminus as the unbound phosphene signal shift upon adding of palladium. A.9 In addition, the Hamilton wedge/ cyanuric acid function can be chemically triggered.

To monitor the different conformations, DOSY measurements were performed [119; 120]. The results of the diffusion measurements are summarised in table 5.5. The diffusion coefficient D is calculated by the Stejskal-Tanner equation. To understand the meaning of the diffusion the Stokes-Einstein equation calculates the hydrodynamic radii r_{hyd} to a good approximation.

Comparing these results illustrate the effect of the individual folding mechanisms. Starting with **SCNP-d1** and **SCNP-d2** before adding a protic solvent it is clearly visible, that the Pd(II) complex effects the diffusion. The diffusion coefficient rises from $2.06 \cdot 10^{-10} m^2 s^{-1}$ to $3.81 \cdot 10^{-10}\mathrm{m^2 s^{-1}}$, which translates into a more compact structure with higher mobility. Consequently the folding motif reduces the hydrodynamic radius from $2.54 \cdot 10^{-09}$m of **SCNP-d1** to $1.37 \cdot 10^{-09}$m of **SCNP-d2**. This is in good agreement with the hypothesis of the metal folding mechanic. Moreover, applying a protic solvents to either polymers reduces the diffusion rate. For **SCNP-d1** it drops to $1.29 \cdot 10^{-10}\mathrm{m^2 s^{-1}}$ and for **SCNP-d2** D is reduced to $3.55 \cdot 10^{-10}\mathrm{m^2 s^{-1}}$. Transfering it into molecule size, the hydrodynamic radii rise to $4.06 \cdot 10^{-09}$m and $1.47 \cdot 10^{-09}$m, respectively.

Table 5.5: DOSY Results dual folding

	D $[10^{-10}\mathrm{m^2s^{-1}}]$	R_{hyd} $[10^{-09}\mathrm{m}]$
SCNP-d1	2.06 ± 0.06	2.54 ± 0.04
SCNP-d1 + MeOH	1.29 ± 0.05	4.06 ± 0.08
SCNP-d2	3.81 ± 0.01	1.37 ± 0.03
SCNP-d2 + MeOH	3.55 ± 0.02	1.47 ± 0.04

The NMR investigations of the dual folding motif revealed an unexpected behaviour of the signals of the Hamilton wedge and cyanuric acid. The Hamilton wedge/ cyanuric acis komplex is very well studied [121], and it could be shown that it is a very dynamic complex with many conformation in exchange. Accordingly, the 1D spectrum of **SCNP-d1** (in figure 5.8 shows signal regions at $\sim$ 9.8ppm, $\sim$ 9.2ppm and a broad hump at $\sim$ 8.6ppm with exchangable hydrogen atoms. Each of the signal regions seems to consist of several individual peaks, underlining the coexistence of exchanging states. Upon addition of Pd, the spectrum of now SCNP-d2 changes significantly. The broad humps disappear and altogether six signals of approximately equal intensities and relatively sharp line widths of $20-40$Hz appear between 9ppm and 12ppm. Also a number of broad peaks are visible in the same region, which we will ignore in the following discussion, as they are either impurities or minor conformers of the complex structure that we will not be able to determine.

The formation of a palladium induced additional binding at the Hamilton wedge terminus increases the resonances of both the Hamilton wedge protons and the cyanuric acid protons, making it six signals in total. Therefore, the cyanuric acid termini are bound to different conformational entities of the Hamilton wedge, which causes a change in the chemical surroundings. This behaviour of the Hamilton wedge group was discussed in prior studies by Maurer-Chronakis [122]. In this work the conformational isomers of the Hamilton wedge are described, of which the cis-cis and the cis-trans conformation feature a possible binding motif for the cyanuric acid to form hydrogen bonds.

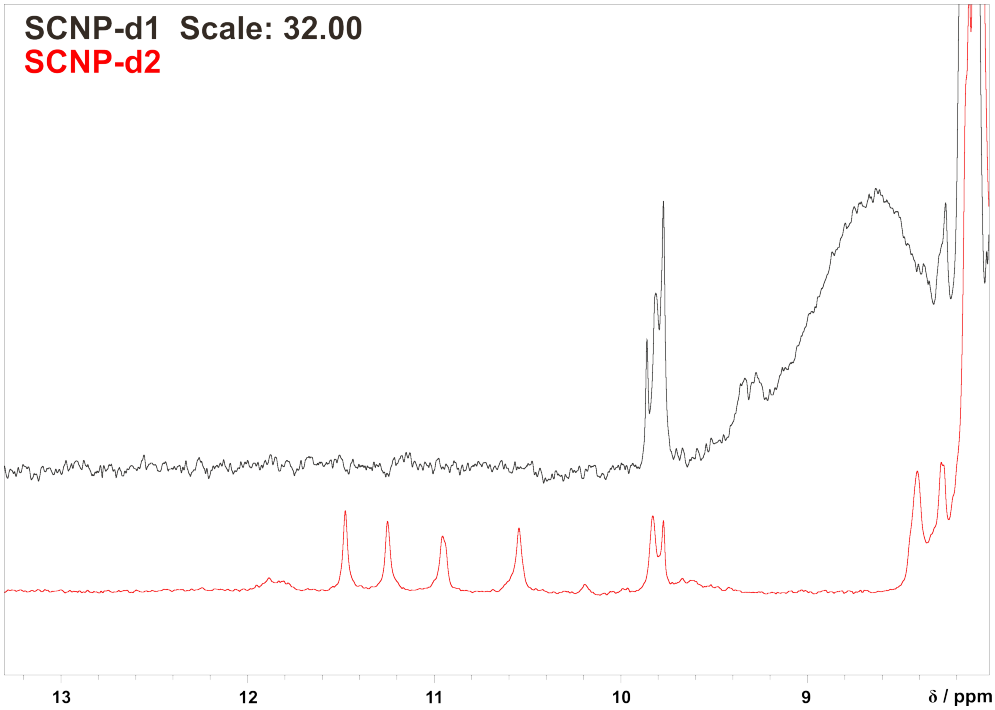

Figure 5.8: 1D spectra of **SCNP-d1** (black) and **SCNP-d2** (red). The application of Pd causes a splitting of the signals in the low field region

A 2D-NOESY spectrum sheds some light onto the structure and a tentative assignment can be performed (figure 5.10). We have altogether six exchange-broadened signals of equal intensities, corresponding to the six NH-groups a1,b1,c1,a2,b2,c2 annotated in figure 5.9. Cross peaks between 11.48ppm, 10.55ppm and 9.86ppm clearly indicate interresidual correlations based on the H-bonded HW/CA complex with 11.48ppm corresponding to b2 and assuming that the aromatic signal at 8.4ppm represents the typical downfield-shifted d1 proton, we can safely assign c1 to 10.55ppm and a1 to 9.86ppm.

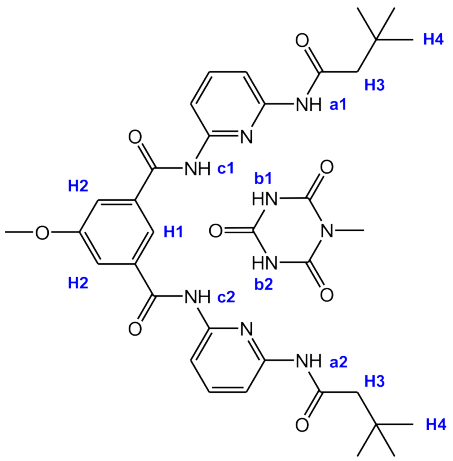

Figure 5.9: Chemical structure of Hamilton wedge/cyanuric acid with corresponding signals

For the second half of the exchanging protons no H-bonding pattern is visible. As

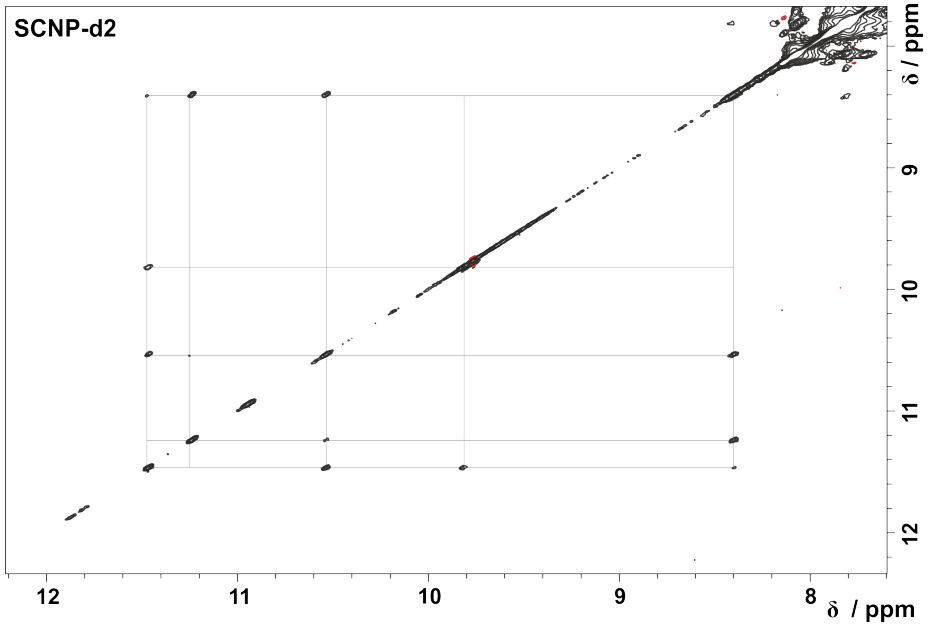

Figure 5.10: NOESY spectrum of **SCNP-d2**. Grey lines indicate the cross-peaks of the Hamilton wedge/ cyanuric acid binding motif. Cross-peaks only occur when the ^{1}H are in close distance. Visible cross-peaks occur between 11.48 ppm (b1), 10.55ppm (c1), 9.82ppm (a1) and 8.41ppm (H1), which indicates, that the cyanuric acid has formed hydrogen bonds with the Hamilton wedge. However, the signals at 11.25ppm (c2), 10.95ppm (a2) and 9.77ppm (b2) show no cross-peaks with signals $>$ 9ppm. Due to the conformational condition of the Pd induced configuration, the 1H of the cyanuric acid are too far away from the Hamilton wedge to create NOE signals

the signal formation is due to the addition of Pd, it must be assumed that some sort of complex is formed with Pd, either as a direct chelate with Pd alone, or a chelation together with the triphenylphosphene moiety. Due to the cross peak with d1 and the weak correlation with c1, we can assign c2 of the second, Pd-bound HW-arm to 11.25ppm. It then follows that signals without cross peaks may be assigned to b2 (10.95ppm) and a2 (9.76ppm), where the corresponding ppm values are chosen because of closest resemblance of chemical shifts of b1 and a1.

To study the influence of triphenylphosphene, we also looked at precursor molecules **D1** and **D2**, which do not contain known Pd chelating groups. The molecular structure of the precursor single chain nano particles are giving in figure 5.11. The resulting 2D-NOESY spectrum of **D2** with Pd salt added is shown in figure 5.12.

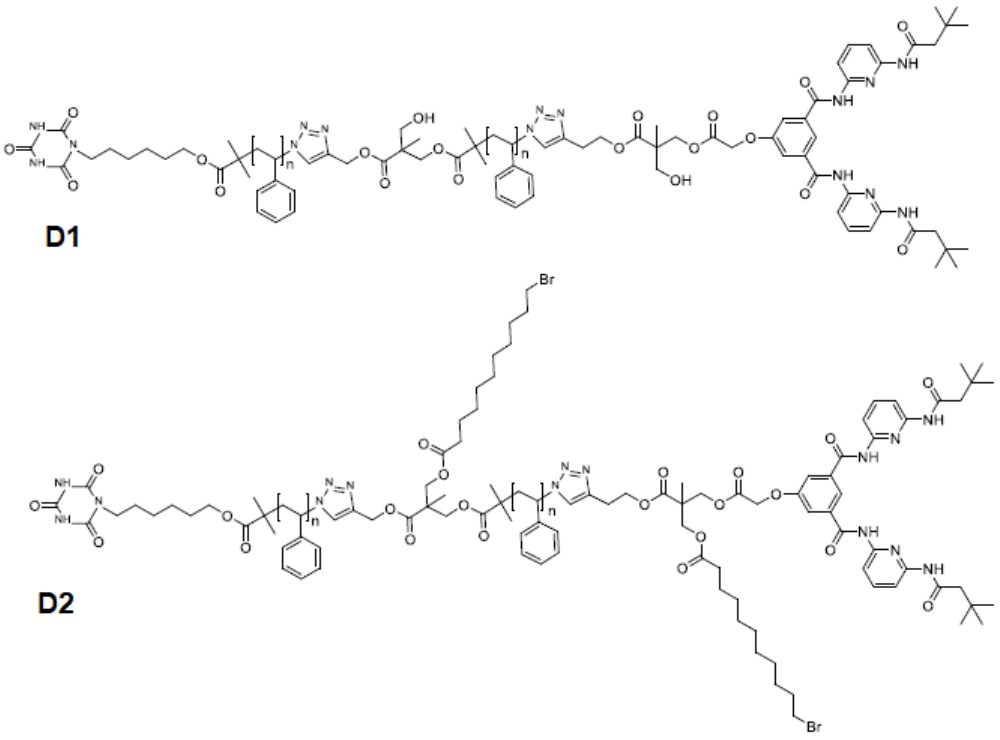

Figure 5.11: Molecular structure of the precursor single chain nanoparticles **D1** and **D2**

To obtain sufficient sensitivity as well as resolution to find cross-peaks due to hydrogen bonds formed by the Hamilton wedge/ cyanuric acid folding motif, each of the NOESY spectra were measured over the total experiment time two and a half days. The mixing time (τ_m) was set to 700ms. The sweep width in both dimensions is 15ppm, with 8k points in F2 and 2k points in F1, resulting in spectral resolution of 2.2Hz and 8.8Hz respectively. In addition with 40 scans for each point, we are able to observe occurring cross-peaks of the diluted SCNPs.

The first notion is a downfield change of chemical shifts of all exchanging protons. This can only be interpreted by the absence of a strongly chemical shift-shifting moiety, the phosphine group. As such, we can answer the previously open question if Pd itself, or Pd in complex with the phosphene is present in **SCNP-d2**. The aromatic groups must be close to Hamilton wedge/ cyanuric acid and so the chelation must happen with the phosphine group on one side and 1, 2, or 3 NH protons from HW/CA on the other side.

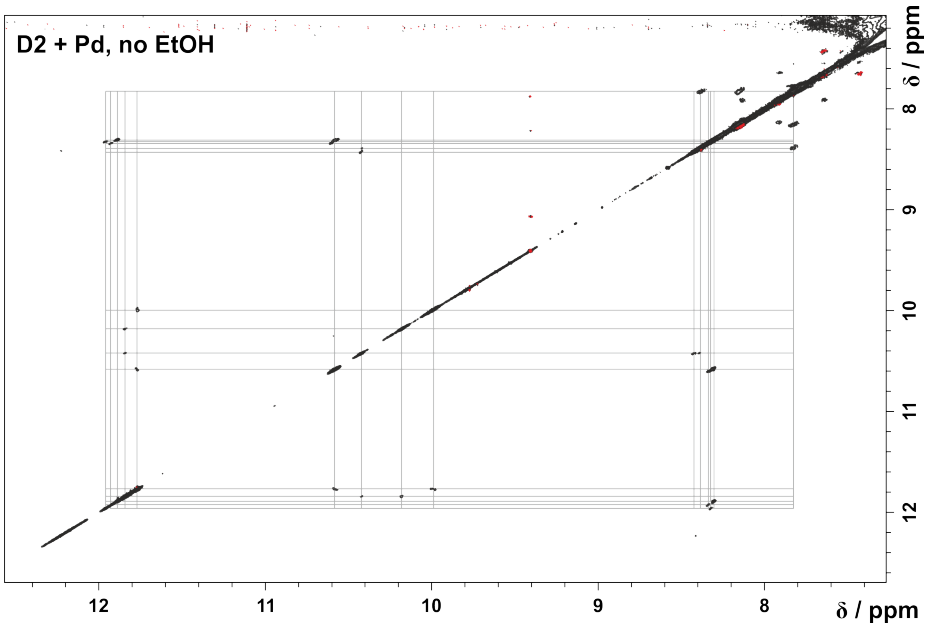

Figure 5.12: The NOESY spectrum of **D2** shows multiple cross-peaks of the Hamilton wedge/cyanuric acid in the downfield region. The visible cross-peaks occur at 10.58ppm/8.31ppm, 10.43ppm/8.42ppm, 11.89ppm/8.31ppm, 11.77ppm/9.99ppm, 11.85ppm/10.18ppm, 11.85ppm/10.43ppm and 11.77ppm/10.58ppm

Besides the chemical shift change, the complex of **D2** with Pd added also results in at least triplicate of the number of cross peaks. Following the cross peak patterns in the 2D NOESY spectrum, at least three conformations exist with the typical Hamilton wedge/ cyanuric acid H-bonding pattern of one arm. As peaks are relatively sharp, it must be assumed that Pd binds again to HW/CA, but apparently in several stable conformers, probably indicating several approximately energetically equivalent binding sites of the metal. At least three conformations are present with c1,b1,a1,d1 at 10.0ppm, 11.75ppm, 10.6ppm, 8.3ppm, visible on the separation of the 3 chemical shifts at d1, and another at least 2 conformers with chemical shifts around 10.2ppm, 11.85ppm, 10.4ppm, 8.4ppm can be identified. The cross peaks for the Pd-bound second arm of the Hamilton wedge can only be identified for b2, for which correlations to d1 indicate at least 4 conformers with b2 chemical shifts above 12ppm.

The addition of EtOH, finally, leads to spectra shown in figure 5.13. Clearly all NOE cross peaks indicating the formation of the Hamilton wedge/ cyanuric acid complex disappear upon addition of ethanol, indicating the expected result that protic EtOH is a strong competitor in H-bond formation of the complex. Interestingly, all other cross peaks remain at their position, being evidence for a maintained Hamilton wedge complex with Pd.

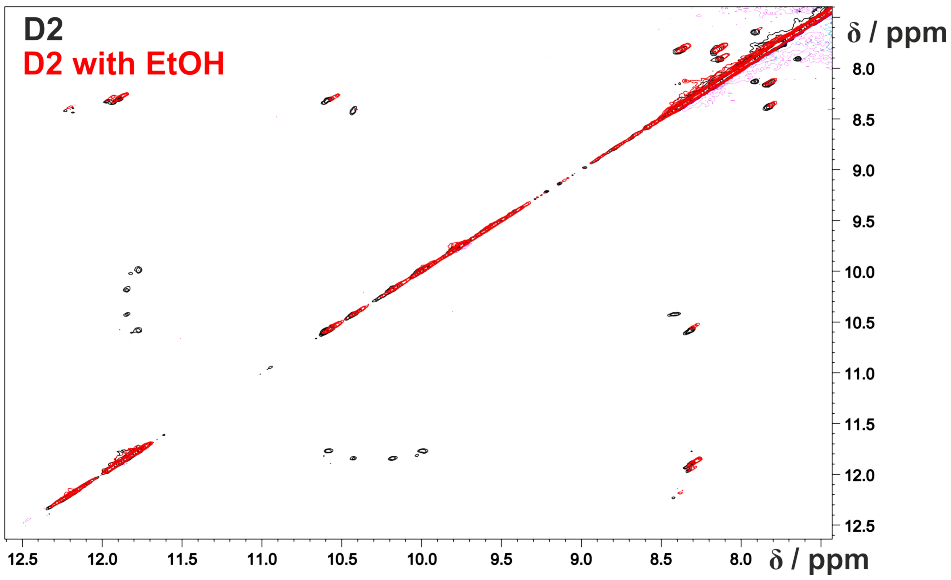

Figure 5.13: In black (**D2**) is the initial state of the SCNP. The spectrum in red is with the application of ethanol.

To investigate the influence of the polar hydroxyl group in the backbone of the **SCNP-d1** extensive NOESY spectra were recorded (figure A.8). With the same parameters in the NOESY sequence, the sensitivity as well as the resolution should be suitable to find all occurring cross-peaks of the Hamilton wedge an the cyanuric acid. However, zooming in the region with $\delta > 9$ppm, there are no cross signal visible at all. At this point, we added no protic solvent that might break the hydrogen bonds of the aforementioned folding motif. The amount of water within the solvent of dichloromethane was measured and found to be lower than $n = 1\mu$mol and therefore should not be able to effectively break the hydrogen bonds. Consequently, the effect of the missing cross-peaks comes from the hydroxyl group in the backbone of **D1**. The polar group close to the Hamilton wedge terminus prohibits the formation of hydrogen bonds between the cyanuric acid and the Hamilton wedge.

In conclusion the triphenylphosphene/palladium Complex and Hamilton wedge/ cyanuric acid folding motif reveals some insight. Palladium shows inherent affinity to the Hamilton wedge. However, as desired, the HW/CA complex can be formed independent of the presence of Pd. If the complex of two PPh2 groups with Pd is formed cannot be unambiguously deduced. However, a HW/CA-Pd-PPh2 complex is certainly formed, according to the DOSY investigation. Furthermore the HW/CA-Pd and HW-Pd complexes are also formed with several resulting conformations in the absence of PPh2 groups.

6. Fast Pulsing DOSY Experiments

After summarising the theory of NMR, fast acquisition and the concept of DOSY, this chapter will merge these parts. The aim was to find a fast, yet robust pulse sequence for diffusion measurement in NMR. To monitor diffusion with NMR, many pulse sequences have been developed and applied for various systems [123]. All these pulse sequences are modifications to improve certain aspects, such as measurement time, resolution, etc.. To understand the advantages of **BETA DOSY** we need to compare it with standard DOSY sequences, which were explained in section 4.6. For comparison **BPLED** and **dSTE** results are shown in this part. Throughout this chapter the reader can follow the development of the **BETA DOSY** and understand the benefit of combining Ernst angle excitation with isotropic mixing.

6.1. β-excited DOSY

The Ernst angle scheme is well known in NMR spectroscopy for reducing the measurement time [124]. Therefore the aim was to implement the Ernst angle excitation into the DOSY sequence. A short flip angle excites enough magnetisation for observable signals and stores polarisation along z. In order to conserve the longitudinal magnetisation, the pulse sequence has to be adapted. Any 90° pulse would counteract this conservation as it would flip the longitudinal magnetisation into the transversal plain. For that reason a stimulated echo sequence should be avoided. However, a spin echo sequence does not remove the remaining longitudinal spin reservoir. Building from this concept the excitation pulse is replaced by a short flip angle, usually a $\beta = 30°$ pulse. After the excitation a pulsed field gradient echo monitors the diffusion of the molecules. As mentioned in section 4.6.1 a bipolar gradient pair has advantages. With just one 180° pulse centering both gradients it would not destroy the longitudinal magnetisation. The graphical representation of the β excited DOSY is given in figure 6.1.The excitation starts with a β pulse. Both the encoding and decoding gradient pulses are bipolar. The diffusion delay Δ begins with the first gradient and ends with the start of the second bipolar gradient. To set the diffusion delay the time between the second and third inversion pulse τ_m can be employed manually.

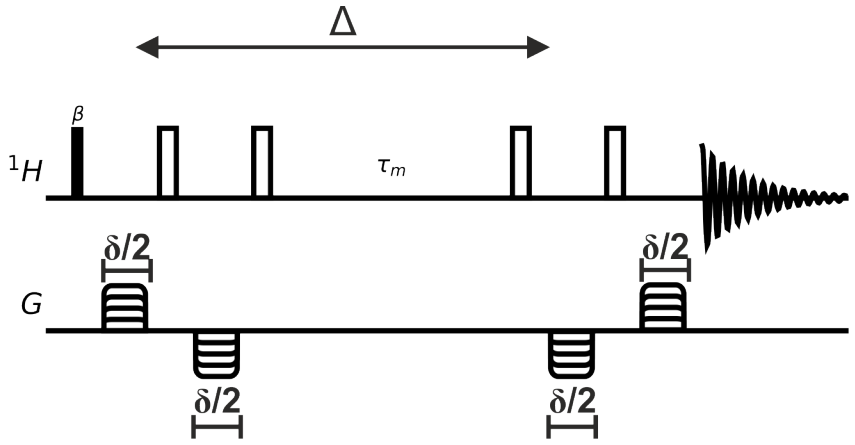

Figure 6.1: Graphical representation of the β BPSE pulse sequence.

After the first bipolar gradient pulse an additional 180° pulse is implemented into the pulse sequence. This pulse flips the reservoir of longitudinal magnetisation from -z to +z. This is crucial for rapid repetition. At the end of each scan, the bulk part of the magnetisation should be along z for subsequent excitation. So, during long delays, like $\tau_m > 50$ms, the magentisation reservoir should be stored along z. Consequently, the second bipolar gradient would rotate the magnetisation along -z and counteract the quick excitation scheme. In order to have the spins stored along z an additional 180° pulse is applied before the second gradient pulse. With four 180° pulses in total the magnetisation is preserved along z. The pulse sequence is called β bipolar spin echo (β BPSE). Although, a spin echo has an inversion pulse in the centre of the gradients, the symmetry of the building block recovers some part of chemical shift evolution.

The pulse sequence was tested on various samples. To illustrate the β BPSE quality in measuring the diffusion it was compared the **BPLED**. Figure 6.2 shows the comparison of DOSY fits between newly derived pulse sequence and the standard. The DOSYs were performed at 300K on menthol in deuterated chloroform. In both sequences the diffusion delay was set to $\Delta = 70$ms and the gradient length was set to $\delta = 1600\mu$s. The measurement duration of the **BPLED** is approximately 15 minutes. On the other hand the total experimental time of the β BPSE is just 14 seconds. This makes the β BPSE 64 times faster than the **BPLED** sequence. This is a significant acceleration of experimental time and could lead to a reduction of spectometer workload.

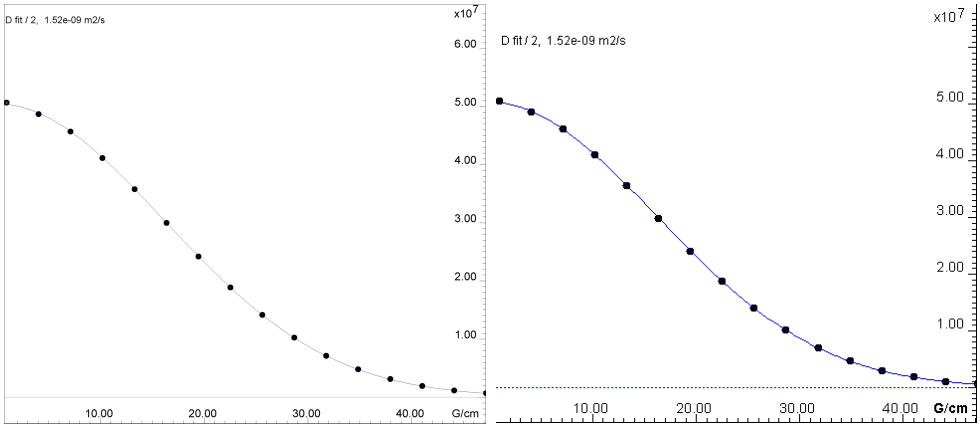

(a) **BPLED** DOSY fit. (b) β BPSE DOSY fit.

Figure 6.2: DOSY fit of menthol in deuterated chloroform. Comparison of the quality of the signal attenuation between BPLED and β BPSE.

The signals at 3.44ppm were plotted and the parameter were fitted with the Skejstal-Tanner Equation. The sigmoidal display of the DOSY results show the correct adjustment of the DOSY parameters. Both trends of DOSY fits are similar, therefore the β BPSE pulse sequence monitors the diffusion with certain accuracy.

Additionally, the performance of the β BPSE was investigated on a camphor sample and on the sequence defined decamer in figure 6.17 [125]. The results are displayed in table 6.1. The diffusion coefficients obtained from the β BPSE are simililar to the diffusion rate obtained by the **BPLED** sequence. The deviation of the diffusion is 5.5% for camphor, 5.0% for menthol and 2.2% for the decamer. Consequently, the rapid acquisition of the β BPSE aquires comparable diffusion coefficents to the standard DOSY.

Table 6.1: Diffusion values of the BPLED sequence and the β BPSE sequence

	D(**BPLED**) [m^{2}s^{-1}]	D(β-BPSE) [m^{2}s^{-1}]
Camphor	$1.38 \cdot 10^{-9}$	$1.31 \cdot 10^{-9}$
Menthol	$1.51 \cdot 10^{-9}$	$1.59 \cdot 10^{-9}$
Decamer	$2.29 \cdot 10^{-9}$	$2.24 \cdot 10^{-9}$

However, the rapid acquisition scheme presented in the β BPSE comes with disadvantages. After the excitation pulse the transversal magnetisation remains in the x/y plain. The 180° pulses are simply changing the signs of x and y magnetisation. Therefore the spins are not aligned along z. In section 4.2 the Hamilton operator of a two spin system was introduced: $\hat{H}_{twospins} = \Omega_1 \hat{I}_{1Z} + \Omega_2 \hat{I}_{2Z} + 2\pi J_{12} \hat{I}_{1Z} \hat{I}_{2Z}$. Each term describes a rotation around the z axis. Longitudinal z magnetisation is unaffected, whereas transversal magnetisation is affected by these z rotations.

Looking at 1D projection of the β BPSE sequence of the menthol sample the effect of the coupling evolution is clearly visible. In figure 6.3, the 1D spectrum is processed in

phase sensitive mode. As a result of J modulation all signals are distorted due to anti phase. Having all signals distorted reduces the chemical shift resolution of the DOSY spectrum. To obtain positive signals, which is crucial for integrating the signals, the spectrum has to be processed in magnitude mode. Downsides are, that the lines get broader.

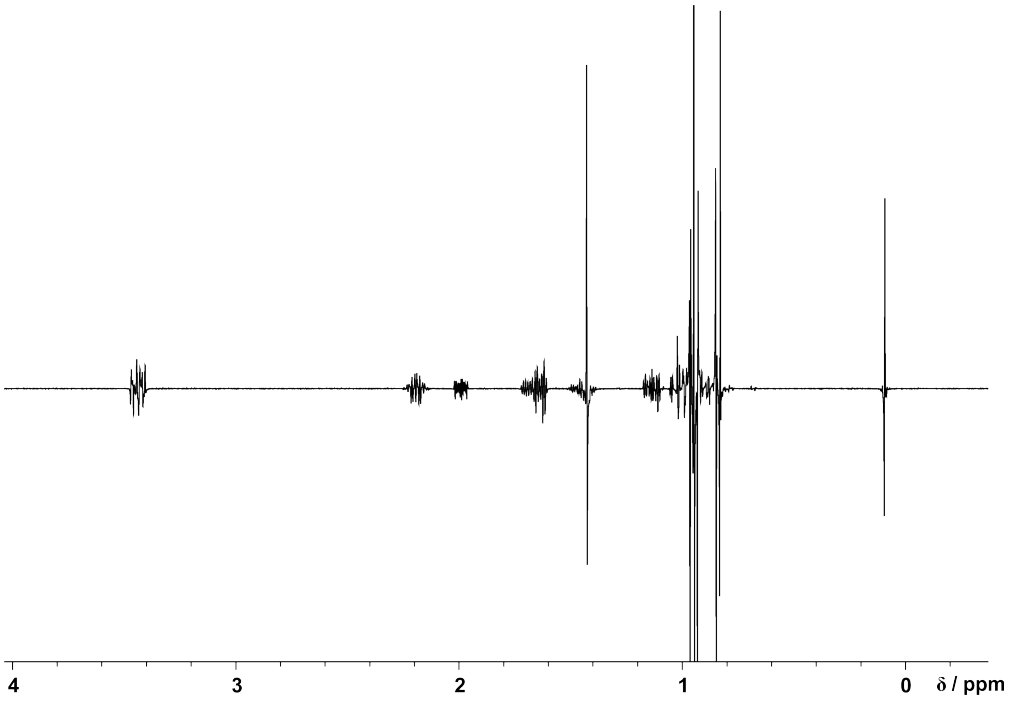

Figure 6.3: ^1H 1D projecion of the β BPSE of menthol in deuterated chloroform

Concluding the fast scan scheme of the β BPSE, the comparison of diffusion coefficients illustrates the utility of the β BPSE. Especially the reduction of overall experimental time can be emphasised. Unfortunately, the coupling evolution present during the diffusion delay averts a wide range of applications. Overlapping signals in molecules with more spins can hardly be measured with the β BPSE pulse sequnce.

6.2. **BETA DOSY**

The previous section illustrated the fast DOSY measurement using the Ernst angle method. Although the experimental time was vastly reduced the evaluation of the β BPSE also identified disadvantages. In order to have a rapid DOSY aquisition the J modulation issue has to be taken care of. In section 4.3 the topic of isotropic mixing was discussed. This section combines the Ernst angle excitation method with isotropic mixing during the diffusion delay.

Preserving the concept of β excitation and using bipolar gradient pulses additional pulse sequence elements are implemented. To achieve isotropic mixing conditions a so called *DIPSI-2* element is inserted during the diffusion delay. *DIPSI-2* was developed

by Rucker and Shaka [126] to improve broadband homonuclear cross-polarisation experiments. It rivals other mixing sequences like the *WALTZ-16*[127; 128] or *MLEV-16* [129] and is utilisied in this work. The graphical representation of the pulse sequence is given in figure 6.4. The pulse sequence is named **B**eta **E**xcitaion **T**ime **A**ccelerated **DOSY**, or short **BETA DOSY**.

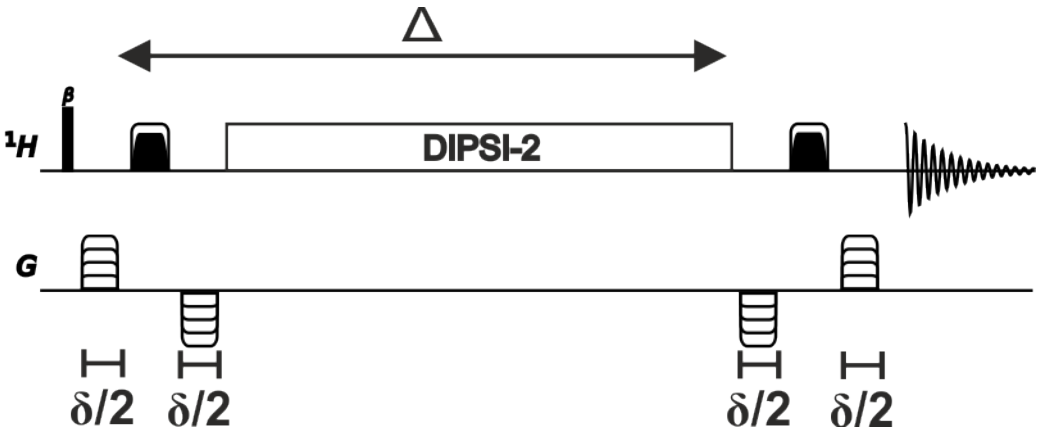

Figure 6.4: Graphical representation of the **BETA** DOSY pulse sequence.

The fundamental concept of DOSY still holds true for the **BETA DOSY**. After excitation a first encoding gradient pulse spatially labels the spins. Afterwards a delay is implemented in which the molecules are moving randomly due to self diffusion. At the end of the delay a second gradient refocuses the spins for acquisition. In the **BETA DOSY** we start with β excitation. The flip angle can be adjusted to suit the observed system. Instead of using one gradient pulse at a time the idea of bipolar gradient pulses remains as it did in the β BPSE. To tackle the issue of the coupling evolution the isotropic mixing sequence *DISPI-2* during Δ, which starts right after the first gradient pair and is applied until the start of the second bipolar gradient. For brevity reasons the *DISPI-2* element is condensed into one block, although in detail it contains a series of pulses with different angles and phases. For a more detailed description the interested reader is referred to [130; 131]. The important information about the *DISPI-2* block is that it provides isotropic mixing conditions. The β pulse excitation scheme works with the conservation of z magnetisation. In order to store the reservoir of z magnetisation the composition of inversion pulses are eminent. In section 4.1.2 we calculated the outcome of repetitive 180° pulses on $\hat{I}_z$.

$$+\cos(\beta)\hat{I}_z \xrightarrow{\pi\hat{I}_y} -\cos(\beta)\hat{I}_z \xrightarrow{\pi\hat{I}_y} +\cos(\beta)\hat{I}_z \tag{6.1}$$

With an even-numbered repetition of inversion pulses the z magnatisation is stored. Consequently the rapid excitation scheme is applicable in the **BETA DOSY** sequence. Moreover, the effect of the isotropic mixing was calculated in section 4.3. The *DISI-2* block refocuses the effect of J modulation in the **BETA DOSY** sequence.

The benefit of utilising the *DIPSI-2* sequence is illustrated in figure 6.5. The **BETA DOSY** was recorded at $T = 300$K. The diffusion delay was set to $\Delta = 71.5$ms and the gradient pulse duration was set to $\delta = 2000\mu$s. The 1D projection of the β BPSE (black) shows phase distortions. With isotropic mixing conditions during the diffusion delay the spectrum regains phase sensitivity. All signals are in phase after the DOSY sequence.

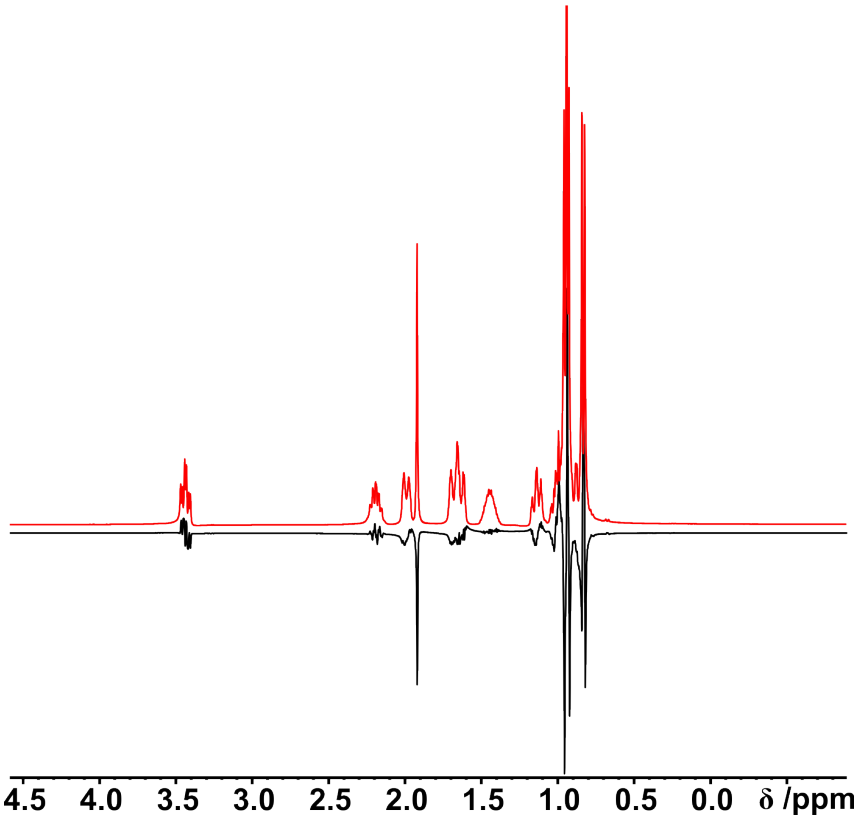

Figure 6.5: 1D projection of menthol in deuterated chlorform. Comparison of the **BETA DOSY** (red) sequence with β BPSE (black) sequence.

The isotropic mixing sequence clearly removes the effect of J modulation. Therefore the DOSY analysis with **BETA DOSY** gives rise to phase sensitive processing and circumvents the necessity of magnitude mode. This is beneficial for the spectral resolution. Ultimately the DOSY quality depends on decent chemical shift resolution as well as discriminating different diffusion coefficients. To achieve sufficient diffusion discrimination either the diffusion delay Δ or the gradients themselves must be adjusted. With longer diffusion delay the signal attenuates additionally due to relaxation, therefore increasing Δ is somewhat limited. In order to achieve better diffusion differentiation, stronger gradients have to be applied. In figure 6.6 the **BETA DOSY** was performed with varying gradient. Starting with 5% (red) of the maximum gradient and increasing it to 20% (blue) and 50% (green). With increasing gradient the sensitivity decreases as expected. The signals were scaled to monitor possible phase distortion. Nevertheless, the phases sensitivity remains intact. This illustrates the **BETA DOSY**s robustness to various gradients strengths and therefore it can be applied in most DOSY measurements.

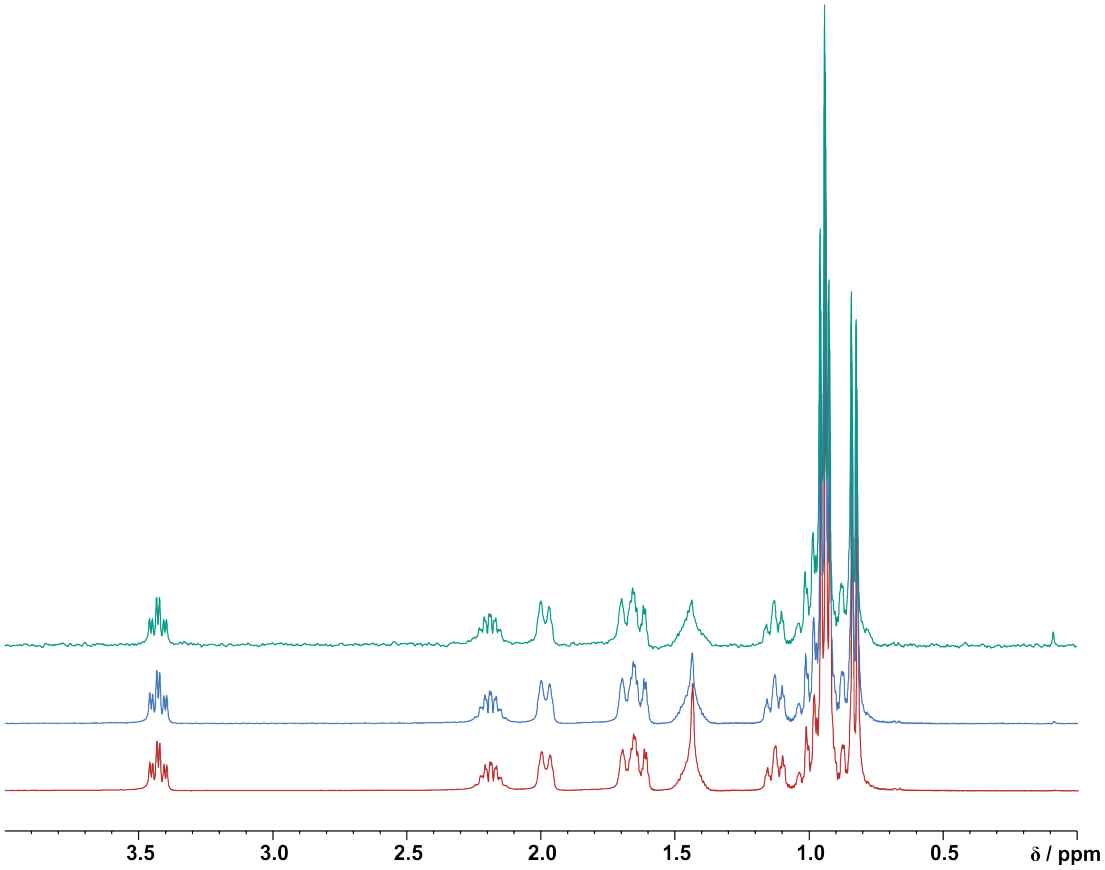

Figure 6.6: **BETA DOSY** of menthol in deuterated chloroform. 1D projections for various gradient strengths: 5% (red), 20% (blue) and 50%. The signal intensity is scaled for tha peak at $\sim$ 3.5ppm in order to observe an effect with increasing gradient strength.

After examining the quality of the isotropic mixing of the **BETA DOSY** we continue to explore the reduction of experimental time. The theory of small flip angle excitation depends on the conservation of longitudinal magnetisation after acquisition. Consequently the next transient can start circumventing long relaxation delays. Therefore the overall experimental duration is shortend drastically. This effect is utilised in the **BETA DOSY** to accelerate the measurement time. In order to reduce the experimental time the optimal flip angle needs to be adjusted. Reciting the theory of section 4.4 the optimal flip angle depends on the magnetisation builtd-up and therefore the longitudinal delay.

Using the model derived for β-excited (AL)SOFAST experiments [16], normalized signal-to-noise-ratios ($\frac{S}{N}$) are measured for the signal at 3.4ppm of menthol in $CDCl_3$. The calcuation was provided by B. Luy. In order to achieve steady state conditions for the polarisation 16 dummy scans were performed. The β-pulse duration was increased incrementally followed by single scan acquisition. Additionally the overall repetition time (T_R) was set to different values, starting with a short repetition time of $T_R = 0.5$s going up to larger repetition of $T_R = 10$s. The fits are illustrated in figure 6.7a. The open symbols represent a single scan 1D experiment with the corresponding fit function. The results are compared to the intensities of the 90° excited **BPLED** sequence represented with filled symbols. With smaller flip angles β and shorter repetition times T_R the signal to noise ($\frac{S}{N}$) is reduced, but more experiments can be acquired in the same overall

measurement time. Therefore the time-normalized signal-to-noise-ratio ($\frac{S}{Nt^{\frac{1}{2}}}$) is more relevant for an appropriate comparison and is illustrated in figure 6.7b. It is evident that shorter repetition times come with no penalty in overall sensitivity for a given experimental time, while more data points can be acquired. In all cases the sensitivity of the **BETA DOSY** experiments by far exceeds **BPLED**.

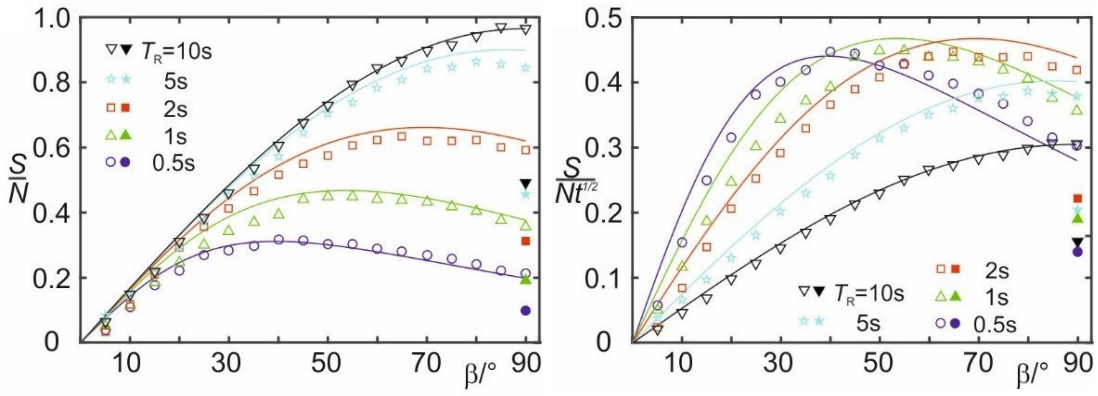

(a) Signal to noise ratio ($\frac{S}{N}$) of different relaxation delays.

(b) Time-normalized signal-to-noise-ratio ($\frac{S}{Nt^{\frac{1}{2}}}$) with different relaxation delays.

Figure 6.7: Calculation (provided by B. Luy) of the optimal flip angle. The signal to noise ratios of the **BETA DOSY** (empty symbols) are compared to the BPLED sequence.

6.3. Convection Compensated BETA DOSY

The previous section highlighted the **BETA DOSY**'s applicability and time acceleration. The newly derived diffusion experiment saves measurement time without having to suffer from resolution reduction. Therefore the **BETA DOSY** rivals the **BPLED** sequence. However, in section 4.6.2 the standard **BPLED** sequence was modified in order to compensate convection [132]. Consequently the aim in this study to rival the **dSTE** with presented rapid DOSY scheme. In this section the findings of the **BETA DOSY** are combined with the double stimulated echo in order to supress the convectional attenuation.

The pulse sequence is given in figure 6.8. The sequence starts with a β excitation pulse and is followed by a bipolar gradient. Each gradient has the gradient length of $\delta/2$. However, the time between the first bipolar gradient and the second bipolar gradient is changed to $\Delta/2$. This is similar to the convection compensation of **dSTE**. The diffusion delay Δ is split into two parts with $\Delta/2$. The length of both segments is equal. In the second segment the gradient composition is of opposite sign relative to the first segment. In order to have a successful β excitation scheme the number of inversion pulses must be even-numbered. In section 4.1.2 we calcuated the outcome of $\hat{I}_z$.

$$+\cos(\beta)\hat{I}_z \xrightarrow{\pi\hat{I}_y} -\cos(\beta)\hat{I}_z \xrightarrow{\pi\hat{I}_y} +\cos(\beta)\hat{I}_z \xrightarrow{\pi\hat{I}_y} -\cos(\beta)\hat{I}_z \xrightarrow{\pi\hat{I}_y} +\cos(\beta)\hat{I}_z \tag{6.2}$$

Analog to the **BETA DOSY** sequence in section 6.2 the spin reservoir is conserved with the composition of even-numbered inversion pulses. The same holds true for the refocussing of J modulation of the *DIPSI-2* sequence.

In section 4.6.2 the method of convection compensation was explained. In order to suppress the flow-velocity-dependent phase factor q_k the coherence order pathway and the effective gradients have to be adjusted:

$$q_k(t) = \int_0^t P(t)G(t)dt \tag{6.3}$$

$q_k(t)$ is function of the dephasing with k being in x, y, or z direction [133]. In figure 6.8 the coherence order pathway (red dotted line) is drawn. The excitation pulse changes the coherence order by $P = \pm 1$ and an inversion pulse inverts the sign of the coherence. In NMR spectroscopy the acquisition is at $P = -1$. So the pathway drawn in figure 6.8 leads to observable magnetisation. The effect of the gradient on the q_k terms is multiplied with the coherence order. For simplicity we normalise the amplitude of the gradient to 1. Now only the sign of the gradient is of interest. Each gradient pulse changes the phase factor q_k. So the contribution to q_k was calculated gradient pulse after gradient pulse.

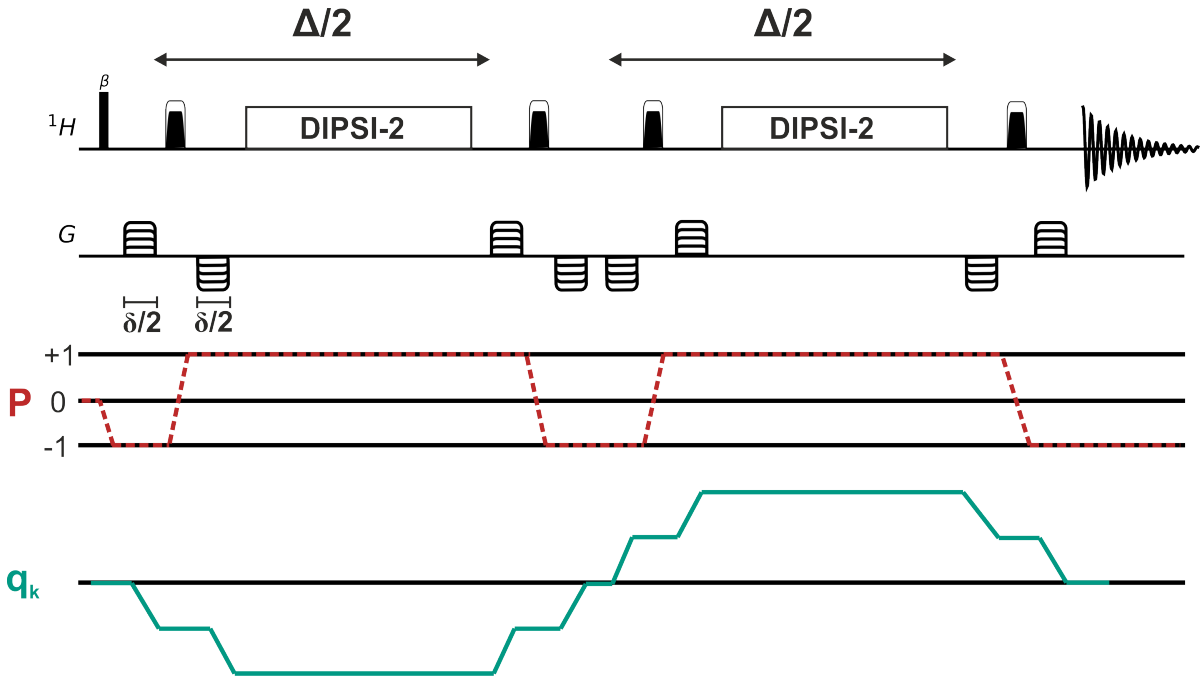

Figure 6.8: Convection compensation BETA DOSY pulse sequence with the schematic representation of the q_k term (green). As both halves are of opposite signs the experiment is convection compensated.

The first gradient is positive, but the coherence is negative. Therefore the contribution to q_k is negative. The result of all gradients are displayed as a green line at the bottom of figure 6.8. After the calculation of all gradient pulses the weigthed sum of the

phase factor is zero. So the composition of gradients and the coherence order pathway compensates laminar convection. Therefore the pulse sequence is called convection compensated **BETA DOSY** (**ccBETA**).

To illustrate the quality of the **ccBETA DOSY** it is applied on many samples. Figure 6.9 shows the 1D projection on menthol in deuterated chloroform. The **ccBETA DOSY** (green) is compared to the **dSTE** (red), the **BPLED** (blue) and the **BETA DOSY** (magenta). The area of 1.9ppm to 2.3ppm is highlighted. The spectra were recorded with a single scan. It is clearly visible that the **BETA DOSY** and the **ccBETA DOSY** show higher sensitivity than their standard counterpart. The **BETA DOSY**'s signal to noise ratio is larger by the factor of two. Applying a stimulated echo flips only half the magnetisation along z. The remaining transversial magentisation is removed by spoiler gradients and consequently does not contribute to the observed signal. Having two stimulated echos reduces the signal intensity by the factor of four. Therefore the **ccBETA DOSY** has a signal to noise ratio roughly four times larger than the **dSTE** sequence.

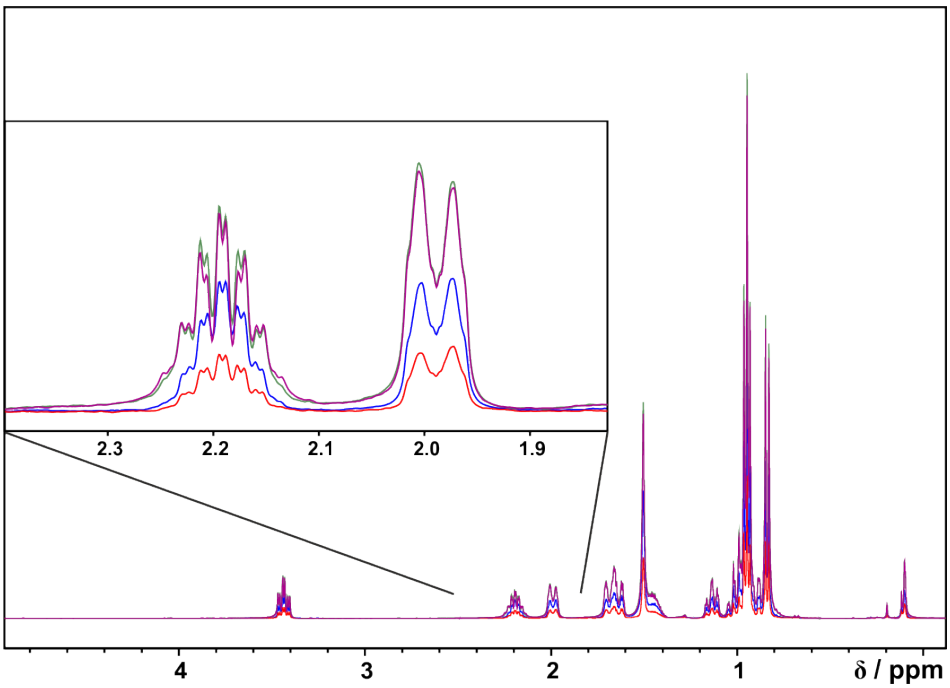

Figure 6.9: Menthol in deuterated chloroform. Comparison of **BPLED** (blue), **dSTE** (red), **BETA DOSY** (magenta) and **ccBETA DOSY** (green). Each spectum was performed with one scan to highlight the signal loss of the stimulated echo by the factor of 2 for **BPLED** and the factor of 4 for the **dSTE**.

6.4. Small molecules and mixtures

Both the **BETA DOSY** and the convection compensated **BETA DOSY** have been introduced in the prior sections. Including the isotropic mixing sequence and applying the concept of Ernst angle excitation reduce the experiment duration without suffering

from sensitivity or resolution reduction. Next the newly derived pulse sequences are applied to various samples. As diffusion NMR plays an important role in analysing small molecule mixtures in organic chemistry [134; 135; 136; 137], or pharmaceutical science [138; 139]. This section illustrates the **BETA DOSY**s potential to analyse these mixtures [140].

6.4.1. Catechin and Flavone

The first mixture of small molecules we introduce is catechin and flavone. The molecular structure is shown in figure 6.10. Both samples have similar molecular weight (catechin: $M(cat) = 290\text{gmol}^{-1}$ flavone: $M(fla) = 222\text{gmol}^{-1}$). The samples were solved in deuterated dimethyl sulfoxide (DMSO-d6). The initial weight of catechin was 15.4mg solved in 1ml of DMSO-d6. Therefore the concentration was set to $c_{cat} = 53\text{mM}$. Analog the concentration of flavone was set to $c_{fla} = 47\text{mM}$ by solving 10.4mg in $1m$l of DMSO-d6. The NMR tube was sealed with a teflon cap in order to minimise evaporation.

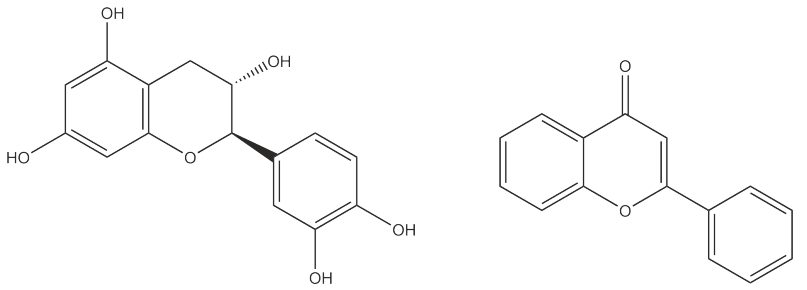

(a) catechin (b) flavone

Figure 6.10: Molecular structure of the small molecule mixture.

The DOSY plot is given in figure 6.11. The **BETA DOSY** experiment was performed at $T = 300\text{K}$. The diffusion delay was set to $\Delta = 150\text{ms}$ and the gradient length was set to $\delta = 4000\mu\text{s}$. The overall experiment duration was reduced to $9s$ and excels the standard **BPLED**. The solvent signal as well as the residual water signal are isolated at 2.51ppm and 3.30ppm respectively. The grey boxes represent all signals of the a diffusion coefficient in a certain range. Therefore these signals belong to the same molecule.

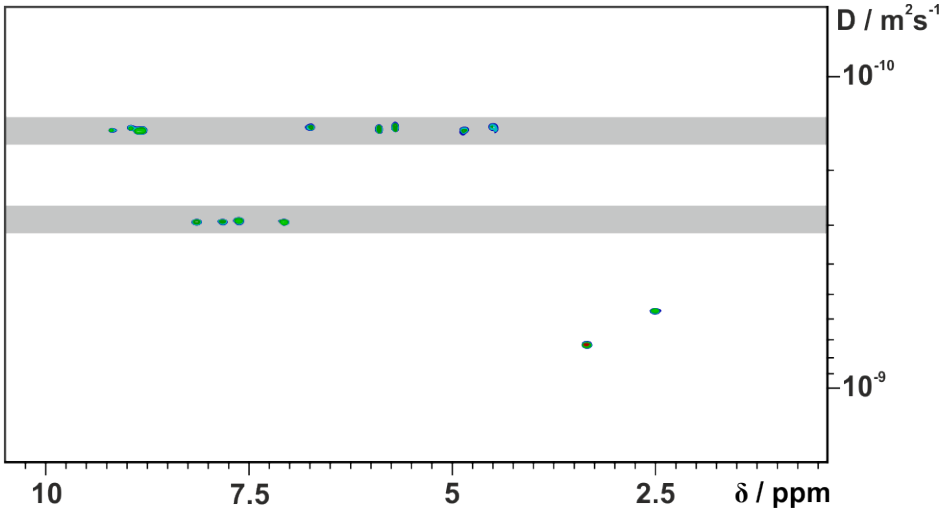

Figure 6.11: **BETA DOSY** plot of the catechin/flavone mixture in DMSO-d6

The results of the **BETA DOSY** are compared to the results of the BPLED. In table 6.2 the diffusion coefficients of catechin and flavone are collated. The diffusion of catechin measured by **BETA DOSY** is $2.92 \cdot 10^{-9}(\pm 0.03)\mathrm{m^2s^{-1}}$ and it is in good agreement with the **BPLED** data. With different diffusion coefficient of $1.48 \cdot 10^{-9}(\pm 0.01)\mathrm{m^2s^{-1}}$ the favone signals are clearly distinguishable from the catechin peaks.

Table 6.2: Diffusion coefficients of catechin/ flavone via BPLED and **BETA DOSY**

	D(**BPLED**)$[10^{-9}\mathrm{m^2s^{-1}}]$	D(**BETA DOSY**) $[10^{-9}\mathrm{m^2s^{-1}}]$
catechin	3.00 ± 0.05	2.92 ± 0.03
flavone	1.49 ± 0.05	1.48 ± 0.01

This example illustrates the **BETA DOSY**'s applicability on mixtures. The analysis of the catechin/ flovone mixture was performed in less than ten seconds. Therefore the analytical performance can be accelerated and the spectrometers workload decreases. In order to illustrate the time optimised sensitivity the sample was acquired with different flip angles. To achieve steady state conditions 16 dummy scans were performed prior to the acquisition. Figure 6.12 illustrates the signal to noise ratio dependent on the flips angle.

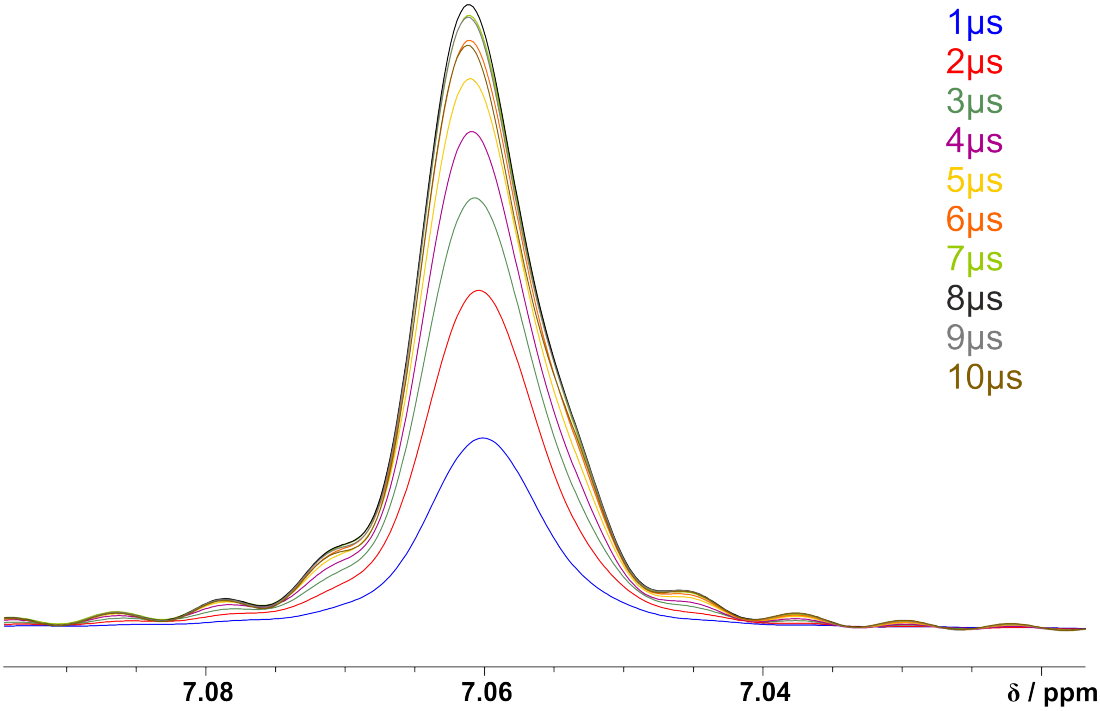

Figure 6.12: Excition pulse duration on the catechin flavone with the resulting signal intensity.

In order to perform the **BPLED** on ideal conditions the 90° pulse was calibrated to 10.1μs. Therefore the β pulse in figure 6.12 was iteratively increased by 1μs starting with 1μs raising β up to 10μs. The maximum intensity is found at 8μs. Furthermore, this stacked representation illustrates that the excitation pulses of $6 - 10\mu$s show signals of similar intensities. This goes to show that the β excitation scheme is robust against deviation of the optimal flip angle.

6.4.2. Glucose, Sucrose and Cholate

After the investigation of a two compound system, the application of the **BETA DOSY**was expanded on a three compound mixture. In this part glucose, sucrose and cholate were dissolved in deutareted dimethyl sulfoxide (DMSO-d6). The concantration was set to 2mM of each compound in order to test the limit of detection. The sample was recorded at $T = 303K$. The diffusion delay was set to $\Delta = 88$ms and the gradient length was set to $\delta = 4000\mu$s. The experiment duration of the **BETA DOSY** was 14s. The results of the DOSY analysis is given in figure 6.13.

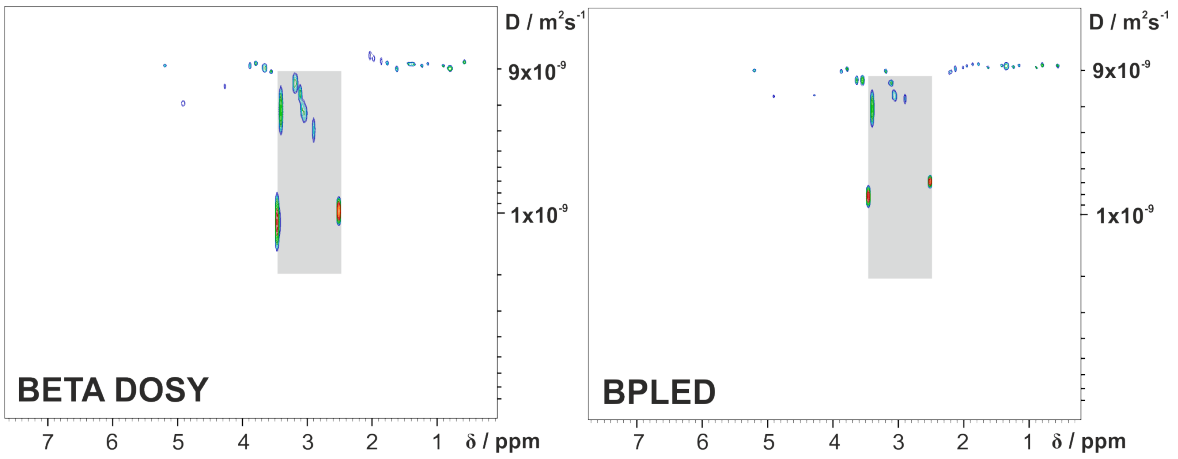

Figure 6.13: DOSY spectra of glucose, sucrose and cholate. Comparison of the **BPLED** with the **BETA DOSY** sequence. The grey box indicates signal overlap with the solvent signal and residual water.

Both DOSY spectra show a region of overlap caused by the solvent signal and residual water. Moreover, the signals of sucrose and glucose are indistuingishable. In both spectra the cholate diffusion is seperated from glucose and sucrose. However, the cholate signals in the downfield region have different diffusion rates measured with the **BETA DOSY**. Therefore, a qualitative differentiation of low concentrated sample could be achieved by the **BETA DOSY**. Yet, the analysis of exact diffusion coefficients at this concentration is erroneous. To circumvent that, the experimental time should be increased to achieve adequate diffusion coefficients.

6.4.3. Menthone, Limonene and Thymole

To highlight the **ccBETA DOSY**s ability to distinguish individual molecule diffusion in mixtures an additional composition of small molecules was investigated. In this study we used menthone, limonene and thymole dissolved in deuterated pyridine. In figure 6.14 the molecular structure as well as the molar mass are illustrated. Both the structure and the mass of these molecules are similar.

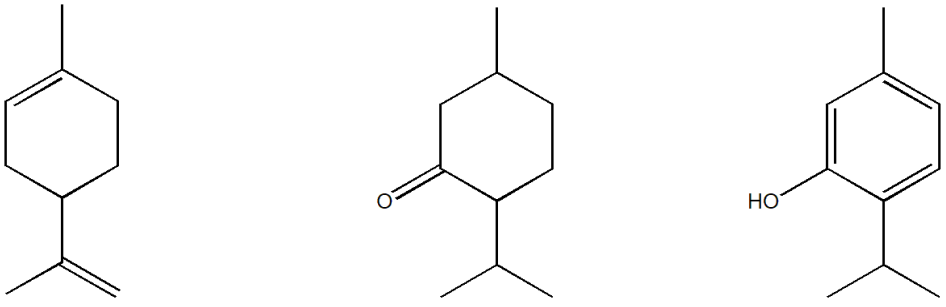

(a) Limonene; $M = 136\text{gmol}^{-1}$ (b) Menthon; $M = 154\text{gmol}^{-1}$ (c) Thymole; $M = 150\text{gmol}^{-1}$

Figure 6.14: molecular structure

The small molecule mix was prepared using 1.4μl of both limonene and menthone with 1.4mg thymole in 500μl pyridine-d5. The DOSY measurments were performed at

$T = 298$K. The diffusion time was set to $\Delta = 147.1$ms and the gradient length was set to $\delta = 2000\mu$s.

Figure 6.15 shows the contour plot of the **dSTE** experiment. The thymole resonances are highlighted with the red bar. The blue box represents the menthone signals. In yellow the limonene signals are indicated. The grey box shows signal overlap in the region of $1.0 - 2.5$ppm. The three pyridine signals $(7.28, 7.68, 8.61$ppm$)$ and the risudual water (5ppm) are not highlighted explicitly.

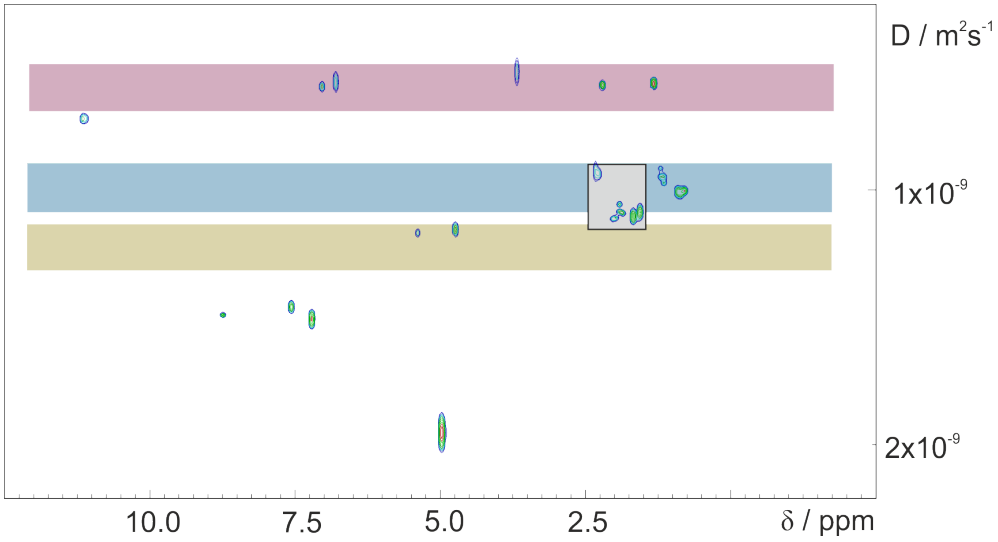

Figure 6.15: dSTE spectrum of limonene, thymole and menthone mixture. The red bar represents the thymole signals, blue bar shows menthone and the yellow bar shows limonene resonances. The grey box shows signal overlap.

After investigating the small molecule mixture with the standard **dSTE** the mixture was analysed with the newly derived pulse sequence. The **ccBETA** was performed in 9 seconds. Figure 6.16 shows the contour plot of the limonene, menthone, thymole mixture. The red bar indicates the thymole signals. Menthone is highlighted by the blue bar. The yellow bar shows the limonene peaks. Comparing the results of the standard DOSY with the **ccBETA** proves the applicability of the **ccBETA** sequence.

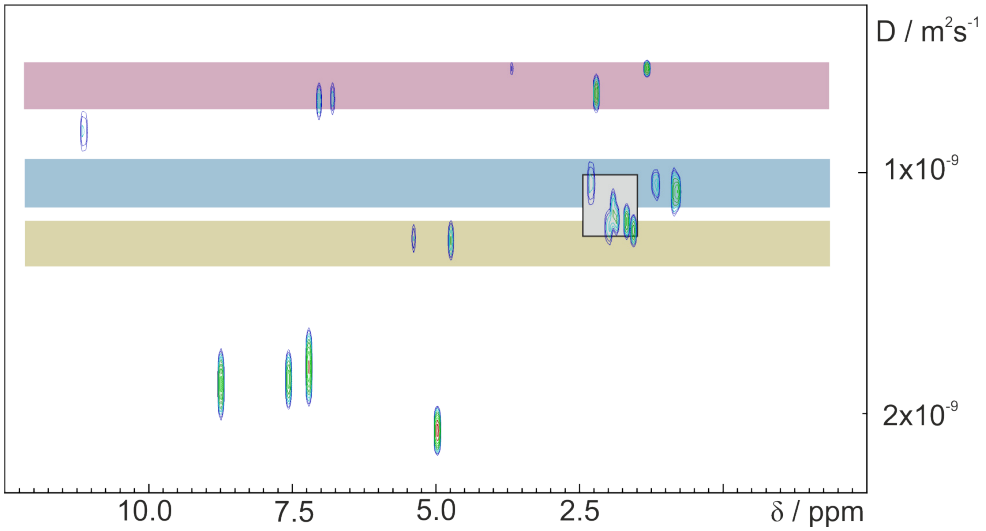

Figure 6.16: ccBETA DOSY spectrum of limonene, thymole and menthone mixture. The total expariment duration was 9 seconds.

The results of the DOSY mexperiments are given in table 6.3. The measured diffusion coefficients by the **ccBETA DOSY** show no signifcant discrepancy from the standard. The deviation is below 1% with 0.3% deviation of the thymole diffusion, 0.9% of limonene and 0.7% of the diffusion coefficient of menthone.

Table 6.3: Summary of the DOSY results of thymole, limonene and menthone. Comparison of the diffusion values of **dSTE** and **ccBETA DOSY**.

	D(**dSTE**) [m^{2}s^{-1}]	D(**ccBETA**) [m^{2}s^{-1}]
thymole	$(7.46 \pm 0.12) \cdot 10^{-10}$	$(7.48 \pm 0.11) \cdot 10^{-10}$
limonene	$(1.12 \pm 0.12) \cdot 10^{-9}$	$(1.13 \pm 0.16) \cdot 10^{-9}$
menthone	$(9.73 \pm 0.10) \cdot 10^{-10}$	$(9.66 \pm 0.14) \cdot 10^{-10}$

All three examples highlight the applicability of **BETA DOSY** and the **ccBETA DOSY** sequence to monitor accurate diffuson of small molecule mixtures. Limonene, thymole and menthone have similar structure and molecular weight, nevertheless the **ccBETA DOSY** was able to distinguish each diffusion coefficent in just 9 seconds of experiment duration.

6.5. Macromolecules and Polymers

After investigating small molecule mixtures with the newly derived sequences we expand the measurement to macromolecules. DOSY measurement play an important role in polymer science. The diffusion coefficient of polymers gives information about its synthesis, cross-linking, size and dynamics [141; 142; 143; 144]. Moreover, the application of diffusion analysis is able to observe polymer mixtures [31].

6.5.1. Decamer

A sequence defined decamer [125] is the first target of the analysis with the new experiment. The synthesis of highly controlled macromolecular systems has been the object of scientists in resent years. In this approach a step growth method is able to design a decamer with selectable side chain. Moreover, the Passerini three-component reaction (P-3CR) generates a perfectly defined macromolecule in a multi-gram scale [145; 146; 147; 2]. The molecular structure is shown in figure 6.17. The backbone consists of the same repeating unit, however the side chains vary in each step.

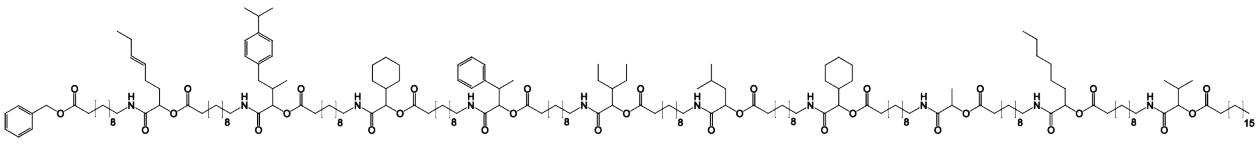

Figure 6.17: Molecular structure of the sequence defined decamer.

The decamer was dissolved in deuterated dichloromethane and the DOSY experiments were performed at $T = 298$K. The difusion time was adjusted to $\Delta = 104$ms with a gradient length of $\delta = 3200\mu$s. The experiment duration of the **ccBETA DOSY** was 46s. The signals of the decamer are stretched in the spectrum from 1ppm up to 7ppm. However the the diffusion coefficients of all signals align in the DOSY plot in figure 6.18. The grey bar entails all decamer resonances signifying that they all belong to one single molecule. The grey box at 5.3ppm underlines the solvent signal of methylene chloride.

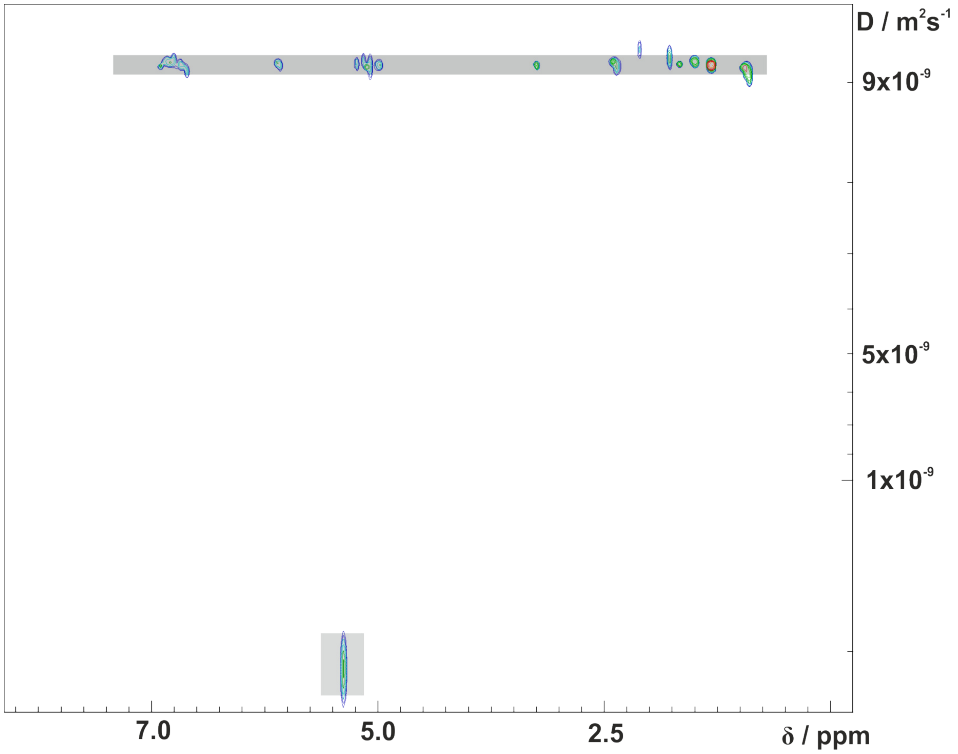

Figure 6.18: DOSY plot of the sequence defined decamer. The grey bar signifies the decamer signals, the grey box shows dichloromethane.

The obtained diffusion coefficient from **ccBETA DOSY** is $D_{ccBETA} = 1.88 \pm 0.02 \cdot 10^{-10}$ m^{2}s^{-1}. For the confirmation of the adequate diffusion the result is compared to the standard **dSTE**. The diffusion coefficient of the **dSTE** experiment is $D_{dSTE} = 1.89 \pm 0.01 \cdot 10^{-10}$m^{2}s^{-1}. The deviation is 0.5%.

6.5.2. Polystyrene

After the defined decamer, the investigation proceeds to unmodified polystyrene. In this study the **ccBETA DOSY** is applied onto polystyrene with approximatly $M_w = 700\,\mathrm{g\,mol^{-1}}$. The polymer was dissolved in deuterated dichloromethane. The sample was measured in at $T = 298$K. The gradient length was set to $\delta = 3200\mu$s and the diffusion delay was set to $\Delta = 145$ms.

The diffusion coefficient measured by double stimulated echo is given in red. In blue the diffusion obteined by the **ccBETA DOSY**. Both signals align and therefore present the same result. In contrast to the convection compensated experiments the **BPLED** is shown as well. The purple signals exhibit different diffusion value. The solvent signal at 5.3ppm is highlighted by the grey box. Due to residual water in the NMR tube the signals overlap at 1.55ppm. This effect is most dominant in the **BPLED** sequence.

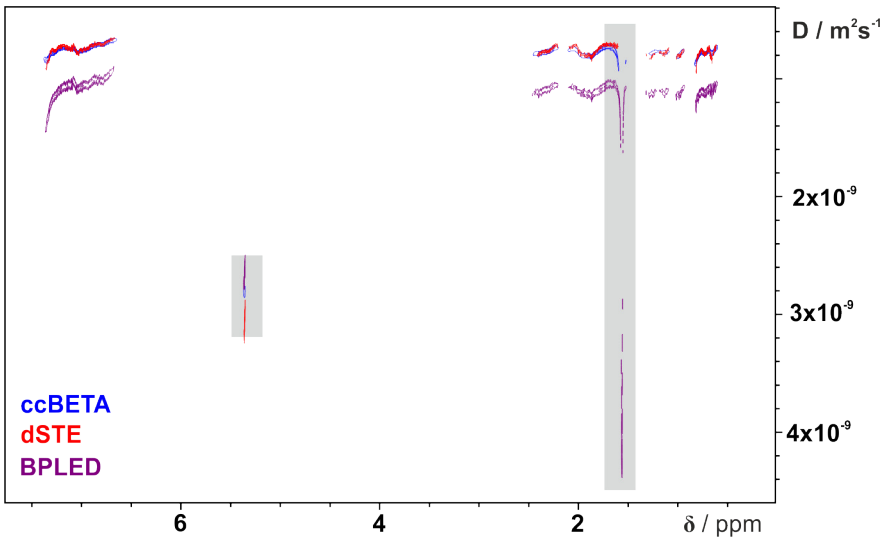

Figure 6.19: DOSY plot of polystyrene in deutareted methylene chloride. Comparison of diffusion coefficent of **BPLED**, **dSTE** and **ccBETA**. Due to convection the **BPLED** sequence gives false D value.

6.6. Dispersity Measurements

To expand the application of the **ccBETA DOSY** to investigate polymer properties, the newly derived pulse sequence is used to determine the dispersity. In section 4.7.3 the theoretical background elucidated the potential of DOSY experiments to obtain the weight distribution of polymers [148; 149; 150]. In this study the **ccBETA DOSY** pulse sequnce measured the diffusion coefficient distribution of macromolecular system. The calculations were perforemed in python. The code is displayed in A.5 and was written in collaboration with Katharina Spies, Felicia Bohnert and Jens Haller.

6.6.1. Decamer Dispersity

The first measured macromolecule was the sequence defined decamer. Due to its highly defined primary structure the molecules are uniform in size and consequently in diffusion. The dispersity index of the decamer is Đ≈ 1 and was confermed by the work of Guo [2]. In order to obtain the dispersity the experimental data were modelled with help of the gamma distribution. The results are summarised in figure 6.20. The blue diamonds represent the experimental points of the **ccBETA DOSY**. The points represent the integral values of the region between 7.502ppm and 6.986ppm. The signal attenuation is fitted with the Stejskal-Tanner equation, given by the orange line. The blue line is the fit with the gamma model.

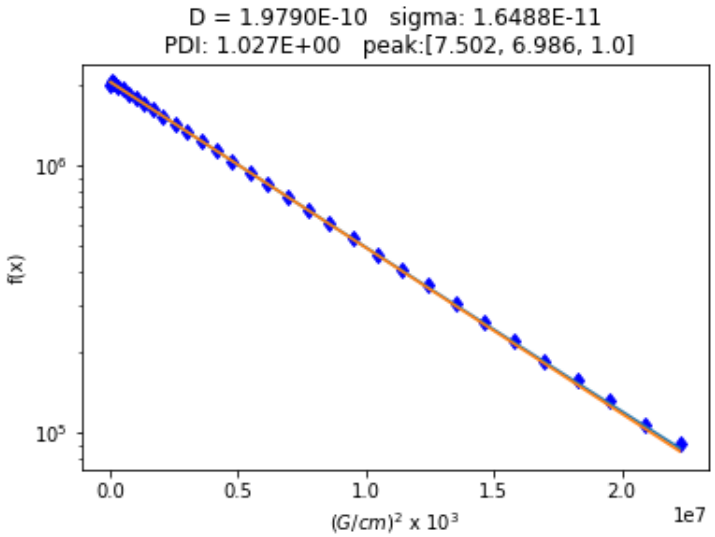

Figure 6.20: DOSY fit of the sequence defined decamer. The blue diamond are the experimental points. The orange line the Stejskal Tanner fit. In blue the data are fited with the gamma model in order to measure the dispersity.

The orange line and the blue line are hardly distinguishable. That signifies the decamers uniformity. The diffusion coefficient is $D = 1.979 \cdot 10^{-10}\mathrm{m}^2\mathrm{s}^{-1}$ and the calculated standard deviation is $\sigma_G = 1.6488 \cdot 10^{-11}$. The dispersity of the decamer is Đ= 1.027, which is in agreement to the work of Guo [2]. This concludes, that the **ccBETA DOSY** sequence gives rise to the same dispersity index and highlights its applicability.

6.6.2. Polystyrene Dispersity

In this study the newly derived DOSY sequence is tested on statistical polymers. Unlike the aformentioned decamer, polystyrene is not uniform. Therefore the dispersity index different is from 1. In order to compare the **ccBETA DOSY** to the dispersity measurement of size exclusion chromatography the analysed polystyrene is a certified standard sample. The sample is part of a calibration kit for the precise measurement of weight distribution. The polystyrene was taken from the calibration kit *PSS-PSKITH* of the company PSS Polymer Standard Service GmbH. In this work the polymer *PSS-PS700* is analysed.

According to the analytic information of the company the values of the SEC are $M_w = 764\mathrm{g\ mol}^{-1}$ and $M_n = 666\mathrm{g\ mol}^{-1}$. Therefore the aquired dispersity index is Đ= 1.15. The corresponding GPC results are given in figure A.10.

The **ccBETA DOSY** experiment was performed at $T = 300\mathrm{K}$. The diffusion delay was set to $\Delta = 145ms$ and the gradient length was set to $\delta = 3200\mu\mathrm{s}$. The total experiment duration was $13s$. In figure 6.21 the DOSY data are fitted. The blue diamonds represent the according integral region (7.643-6.305) values at each gradiend step. The orange line represents the diffusion attenuation with the Stejskal-Tanner equation. The blue curve is the fit with the gamma model. The diffusion coefficient is $D = 7.75850^{-10}\mathrm{m}^2\mathrm{s}^{-1}$.

With help of the gamma model the aquired dispersiy indix is Đ= 1.145. The calculated dispersity of the **ccBETA DOSY** has a deviation of just 0.44% compared with the SEC data.

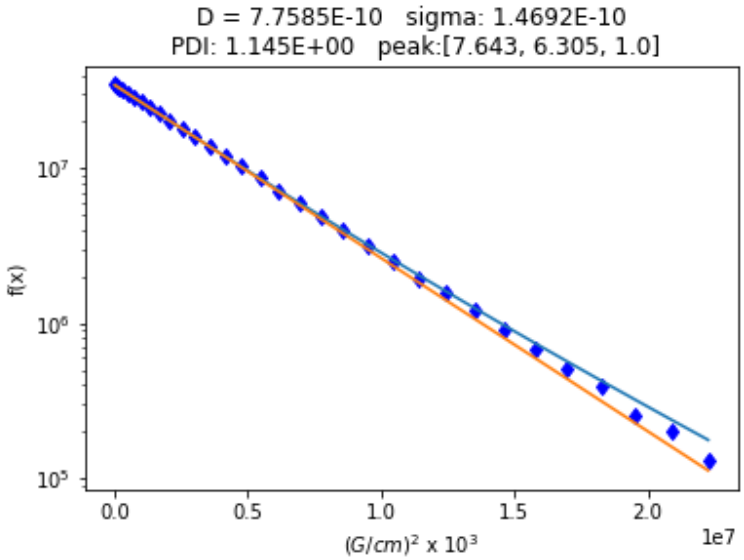

Figure 6.21: DOSY fit of polystyrene.

Moreover, the diffusion distribution of the polystyrene sample *PSS-PS700* is calculated with the gamma distribution in equation 4.55. The calculated values of the scale (θ) and the shape (κ) of the gamma bell are $\theta = 2.78226072774 \cdot 10^{-11}$ and $\kappa = 27.8854613925$. The gamma plot is given in figure 6.22.

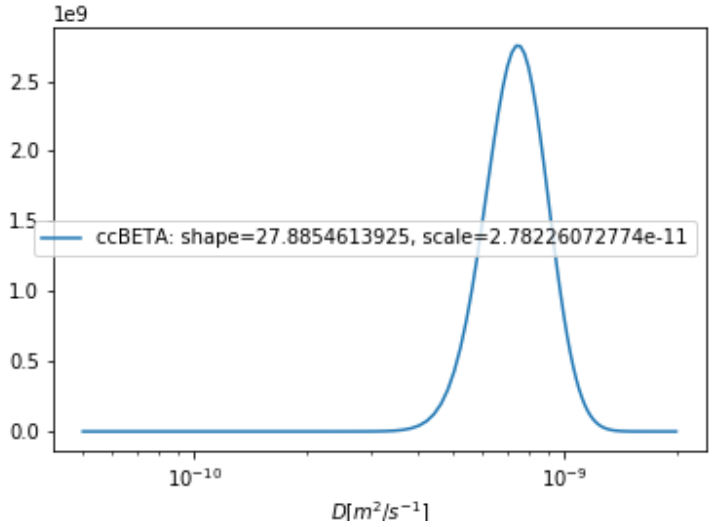

Figure 6.22: Diffusion distribution of *PSS-PS700* calculated with the gamma distribution.

The calculated diffusion coefficient distribution shows a narrow gamma bell. This is in good agreement with low value of the dispersity index. Therefore the diffusion rates

of the different polymer chains are similar. In plolymer analytics the quality control is commonly given in weight distribution. As described in section 4.7.3 the diffusion distribution is indirectly linked to the weight distribution. The correlation between the diffusion distribution and the weight distribution is given with equation 6.4:

$$D = KM^{-\alpha} \tag{6.4}$$

with α and K being scaling parameters specific to the studied material. Therefore the findings of the diffusion distribution are converted to the weight distribution. The value α represents the proportional radius of the particle and is in the regime $\alpha \sim 0.5 - 0.8$ [151]. In literature the value for polystyrene is given with $\alpha = 0.51$ and was applied in this study. Moreover, the value of K was set to $K = 2 \cdot 10^{-8}$ according to former studies of Williamson [152]. The results of the molecular weight distribution is given in figure 6.23.

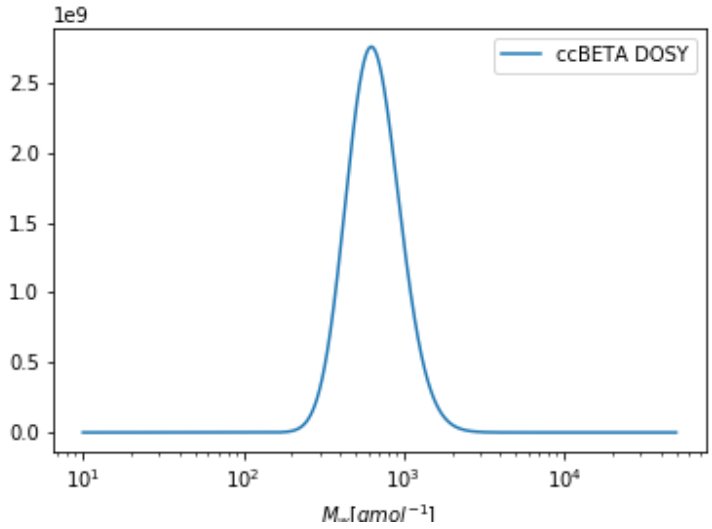

Figure 6.23: Molecular weight distribution of *PSS-PS700* calculated with the gamma distribution.

The molecular weight distribution of *PSS-PS700* shows a narrow distribution. This is in agreement with the low dispersity index of 1.145. Moreover, the comparison the SEC data of PSS indicates that the distribution obtained by the **ccBETA DOSY** is similar. We have to remind ourselves, that the resolution of the SEC is linked to the retention time. Having short chain lengths the chromatographic approach detects single molecule entities. Therefore, the SEC results seem like a multi peak spectrum. However, the envelope of all curves is comparable the DOSY results.

The **ccBETA DOSY** sequence obtains the molecular weight distribution of *PSS-PS700* was measured in just 13 seconds of experiment time. The accelerated DOSY measurement illustrates its applicability on polymer systems. In addition it highlights that **ccBETA DOSY** is fast alternative, if not a substitute for the chromatography analyis.

7. Conclusion

The field of single chain folding has attracted a lot of interest in recent years. The aim to mimic natural polymers in conformational precision and functionality would ultimately lead to a vast field of application. The concept of implementing specific folding points or controlling the step growth reaction are sophisticated methods of single chain nanoparticles. First promising results in medicinal studies highlight the benefit of innovation. The introduction of new single chain species goes hand in hand with the introduction of novel methods. DOSY has proven to be a sufficient tool to help reveal complex folding mechanisms. Additionally, synthesis control is obtained with DOSY as it enables to measure the diffusion distribution that is directly linked the the molecular weigth distribution.
In general, the analysis of the diffusion measuremnt with NMR is deap-seated in the scientific community and analytical departments alike. Consequently, the improvements in DOSY experiments are employed in many applications. The removal of coupling evolution and phase distortion have been the target of many approaches, like the Oneshot45 sequence [153], the isotropic perfect echo [154], or the application of purge elements [155]. All of the above sequences remove occuring anti-phase terms. The benefit of the newly derived **BETA DOSY** is its simplicity as it utilises the well established *DIPSI-2* block. The implementation of the pulse sequence elements is straightforward, without the use of extensive coherence order pathways of calibration of pulses.
In addition to the removal of coupling effects, the **BETA DOSY** convinces with the reduction of experiment duration. Fast excitation schemes are common in NMR as efficient spectrometer workload is of the essence. That implies DOSY experiments as well [156; 157; 158]. The benefit of the **BETA DOSY** lies in its applicability. The **BETA DOSY** was tested on various samples, ranging from small molecule mixtures to macromolecular system. Having an experiment duration of under 10 seconds the DOSY is recorded without suffering in spectral quality. The sensitivity has proven to be sufficient to monitor adequate diffusion coefficients. Moreover, the **ccBETA DOSY** was able to accurately identify the dispersity index of polymer samples.
Ultimately, this work introduces a versatile DOSY sequence for various applications. The sequence is fast, yet precise and can be implemented in the analytical routine of analytical departments to reduce the spectrometer workload.

Appendices

Bibliography

[1] L. D. Thai, T. R. Guimaraes, S. Spann, A. S. Goldmann, D. Golberg, H. Mutlu, and C. Barner-Kowollik, "Photoswitchable block copolymers based on main chain α-bisimines," *Polymer Chemistry*, vol. 13, no. 39, pp. 5625–5635, 2022.

[2] X. Guo, K. S. Wetzel, S. C. Solleder, S. Spann, M. A. R. Meier, M. Wilhelm, B. Luy, and G. Guthausen, "^{1}H PFG-NMR diffusion study on a sequence-defined macromolecule: Confirming monodispersity," *Macromolecular Chemistry and Physics*, vol. 220, aug 2019.

[3] T. S. Fischer, S. Spann, Q. An, B. Luy, M. Tsotsalas, J. P. Blinco, H. Mutlu, and C. Barner-Kowollik, "Self-reporting and refoldable profluorescent single-chain nanoparticles," *Chemical Science*, vol. 9, no. 20, pp. 4696–4702, 2018.

[4] J. J. Keeler, "Understanding nmr spectroscopy," 2011. Description based upon print version of record.

[5] M. H. Levitt, *Spin dynamics*. Chichester: Wiley, 2. ed., repr. ed., 2011. Includes bibliographical references.

[6] M. Karplus, "bvicinal proton coupling in nuclear magnetic resonance/b," *Journal of the American Chemical Society*, vol. 85, pp. 2870–2871, sep 1963.

[7] P. Schmieder, M. Kurz, and H. Kessler, "Determination of heteronuclear long-range couplings to heteronuclei in natural abundance by two- and three-dimensional NMR spectroscopy," *Journal of Biomolecular NMR*, vol. 1, pp. 403–420, nov 1991.

[8] K. Takegoshi, K. Ogura, and K. Hikichi, "A perfect spin echo in a weakly homonuclear j-coupled two spin- system," *Journal of Magnetic Resonance (1969)*, vol. 84, pp. 611–615, oct 1989.

[9] Z. Mádi, B. Brutscher, T. Schulte-Herbrüggen, R. Brüschweiler, and R. Ernst, "Time-resolved observation of spin waves in a linear chain of nuclear spins," *Chemical Physics Letters*, vol. 268, pp. 300–305, apr 1997.

[10] O. Schedletzky, B. Luy, and S. J. Glaser, "Analytical polarization and coherence transfer functions for three coupled spins 1/2 under planar mixing conditions," *Journal of Magnetic Resonance*, vol. 130, pp. 27–32, jan 1998.

[11] B. Luy and S. J. Glaser, "Analytical planar mixing transfer functions for two coupled spin-1 nuclei," *Journal of Magnetic Resonance*, vol. 153, pp. 210–214, dec 2001.

[12] B. Luy and S. J. Glaser, "Transverse magnetization transfer under planar mixing conditions in spin systems consisting of three coupled spins 1/2," *Journal of Magnetic Resonance*, vol. 164, pp. 304–309, oct 2003.

[13] A. Garon, R. Zeier, and S. J. Glaser, "Visualizing operators of coupled spin systems," *Physical Review A*, vol. 91, p. 042122, apr 2015.

[14] R. R. Ernst and W. A. Anderson, "Application of fourier transform spectroscopy to magnetic resonance," *Review of Scientific Instruments*, vol. 37, pp. 93–102, jan 1966.

[15] R. R. Ernst, G. Bodenhausen, and A. Wokaun, *Principles of nuclear magnetic resonance in one and two dimensions*. No. 14 in The @international series of monographs on chemistry, Oxford [u.a.]: Clarendon Press, repr. ed., 2004. Literaturverz. S. [565] - 596.

[16] M. R. Koos and B. Luy, "Polarization recovery during ASAP and SOFAST/ALSOFAST-type experiments," *Journal of Magnetic Resonance*, vol. 300, pp. 61–75, mar 2019.

[17] A. Haase, J. Frahm, D. Matthaei, W. Hanicke, and K.-D. Merboldt, "FLASH imaging. rapid NMR imaging using low flip-angle pulses," *Journal of Magnetic Resonance (1969)*, vol. 67, pp. 258–266, apr 1986.

[18] D. Schulze-Sünninghausen, J. Becker, M. R. Koos, and B. Luy, "Improvements, extensions, and practical aspects of rapid ASAP-HSQC and ALSOFAST-HSQC pulse sequences for studying small molecules at natural abundance," *Journal of Magnetic Resonance*, vol. 281, pp. 151–161, aug 2017.

[19] J. Becker, M. R. Koos, D. Schulze-Sünninghausen, and B. Luy, "ASAP-HSQC-TOCSY for fast spin system identification and extraction of long-range couplings," *Journal of Magnetic Resonance*, vol. 300, pp. 76–83, mar 2019.

[20] Y. Cohen, L. Avram, and L. Frish, "Diffusions-NMR-spektroskopie in der supramolekularen und kombinatorischen chemie: ein alter parameter - neue erkenntnisse," *Angewandte Chemie*, vol. 117, pp. 524–560, jan 2005.

[21] C. Johnson, "Diffusion ordered nuclear magnetic resonance spectroscopy: principles and applications," *Progress in Nuclear Magnetic Resonance Spectroscopy*, vol. 34, pp. 203–256, may 1999.

[22] D. Sinnaeve, "Diffusional attenuation," mar 2016.

[23] P. T. Callaghan, "Translational dynamics and magnetic resonance," 2011. Description based on publisher supplied metadata and other sources.

[24] C. S. J. Jr., "ChemInform abstract: Diffusion ordered nuclear magnetic resonance spectroscopy: Principles and applications," *ChemInform*, vol. 30, pp. no–no, jun 2010.

[25] J. A. Aguilar, R. W. Adams, M. Nilsson, and G. A. Morris, "Suppressing exchange effects in diffusion-ordered NMR spectroscopy," *Journal of Magnetic Resonance*, vol. 238, pp. 16–19, jan 2014.

[26] A. R. Bilia, M. Bergonzi, F. F. Vincieri, P. L. Nostro, and G. A. Morris, "A diffusion-ordered NMR spectroscopy study of the solubilization of artemisinin by octanoyl-6-o-ascorbic acid micelles," *Journal of Pharmaceutical Sciences*, vol. 91, pp. 2265–2270, oct 2002.

[27] S. Viel, D. Capitani, L. Mannina, and A. Segre, "Diffusion-ordered NMR spectroscopy: a versatile tool for the molecular weight determination of uncharged polysaccharides," *Biomacromolecules*, vol. 4, pp. 1843–1847, sep 2003.

[28] A. Ambrus and D. Yang, "Diffusion-ordered nuclear magnetic resonance spectroscopy for analysis of DNA secondary structural elements," *Analytical Biochemistry*, vol. 367, pp. 56–67, aug 2007.

[29] J. K. Young, G. R. Baker, G. R. Newkome, K. F. Morris, and C. S. Johnson, ""smart" cascade polymers. modular syntheses of four-directional dendritic macromolecules with acidic, neutral, or basic terminal groups and the effect of pH changes on their hydrodynamic radii," *Macromolecules*, vol. 27, pp. 3464–3471, jun 1994.

[30] S. M. Patil, D. A. Keire, and K. Chen, "Comparison of NMR and dynamic light scattering for measuring diffusion coefficients of formulated insulin: Implications for particle size distribution measurements in drug products," *The AAPS Journal*, vol. 19, pp. 1760–1766, aug 2017.

[31] A. Jerschow and N. Müller, "Diffusion-separated nuclear magnetic resonance spectroscopy of polymer mixtures," *Macromolecules*, vol. 31, pp. 6573–6578, aug 1998.

[32] X. Guo, E. Laryea, M. Wilhelm, B. Luy, H. Nirschl, and G. Guthausen, "Diffusion in polymer solutions: Molecular weight distribution by PFG-NMR and relation to SEC," *Macromolecular Chemistry and Physics*, vol. 218, nov 2016.

[33] A. Einstein, "Eine neue bestimmung der moleküldimensionen," *Annalen der Physik*, vol. 324, pp. 289–306, jan 1906.

[34] A. Waldeck, P. W. Kuchel, A. J. Lennon, and B. E. Chapman, "NMR diffusion measurements to characterise membrane transport and solute binding," *Progress in Nuclear Magnetic Resonance Spectroscopy*, vol. 30, pp. 39–68, mar 1997.

[35] R. Cotterill, *Biophysik*. Bachelor, Weinheim: WILEY-VCH, 1. aufl. ed., 2008. Originaltitel publ. 2002, Wiley.

[36] P. W. Atkins, "Physikalische chemie," 2022. Die Originalausgabe Atkins' Physical Chemistry, Eleventh Edition, wurde 2017 in Englisch publiziert.

[37] E. L. Hahn, "Spin echoes," *Physical Review*, vol. 80, pp. 580–594, nov 1950.

[38] M. Foroozandeh, L. Castañar, L. G. Martins, D. Sinnaeve, G. D. Poggetto, C. F. Tormena, R. W. Adams, G. A. Morris, and M. Nilsson, "Ultrahigh-resolution diffusion-ordered spectroscopy," *Angewandte Chemie International Edition*, vol. 55, pp. 15579–15582, nov 2016.

[39] M. G. Concilio, P. Kiraly, and G. A. Morris, "Diffusional attenuation during soft pulses: A zangger-sterk pure shift iDOSY experiment," *Journal of Magnetic Resonance*, vol. 301, pp. 85–93, apr 2019.

[40] I. A. Thomlinson, M. G. Davidson, C. L. Lyall, J. P. Lowe, and U. Hintermair, "Fast and accurate diffusion NMR acquisition in continuous flow," *Chemical Communications*, vol. 58, no. 59, pp. 8242–8245, 2022.

[41] W. S. Price and M. Wälchli, "NMR diffusion measurements of strong signals: the PGSE-iq/i-switch experiment," *Magnetic Resonance in Chemistry*, vol. 40, nov 2002.

[42] P. Groves, "Diffusion ordered spectroscopy (DOSY) as applied to polymers," *Polymer Chemistry*, vol. 8, no. 44, pp. 6700–6708, 2017.

[43] E. O. Stejskal and J. E. Tanner, "Spin diffusion measurements: Spin echoes in the presence of a time-dependent field gradient," *The Journal of Chemical Physics*, vol. 42, pp. 288–292, jan 1965.

[44] J. E. Tanner, "Use of the stimulated echo in NMR diffusion studies," *The Journal of Chemical Physics*, vol. 52, pp. 2523–2526, mar 1970.

[45] R. Cotts, M. Hoch, T. Sun, and J. Markert, "Pulsed field gradient stimulated echo methods for improved NMR diffusion measurements in heterogeneous systems," *Journal of Magnetic Resonance (1969)*, vol. 83, pp. 252–266, jun 1989.

[46] R. Karlicek and I. Lowe, "A modified pulsed gradient technique for measuring diffusion in the presence of large background gradients," *Journal of Magnetic Resonance (1969)*, vol. 37, pp. 75–91, jan 1980.

[47] D. Sinnaeve, "The stejskal-tanner equation generalized for any gradient shape-an overview of most pulse sequences measuring free diffusion," *Concepts in Magnetic Resonance Part A*, vol. 40A, pp. 39–65, mar 2012.

[48] S. J. Gibbs and C. S. Johnson, "A PFG NMR experiment for accurate diffusion and flow studies in the presence of eddy currents," *Journal of Magnetic Resonance (1969)*, vol. 93, pp. 395–402, jun 1991.

[49] M. Nilsson and G. A. Morris, "Improving pulse sequences for 3d DOSY: Convection compensation," *Journal of Magnetic Resonance*, vol. 177, pp. 203–211, dec 2005.

[50] I. Swan, M. Reid, P. Howe, M. Connell, M. Nilsson, M. Moore, and G. Morris, "Sample convection in liquid-state NMR: Why it is always with us, and what we can do about it," *Journal of Magnetic Resonance*, vol. 252, pp. 120–129, mar 2015.

[51] E. Caytan, H. M. Foster, L. Castañar, R. W. Adams, M. Nilsson, and G. A. Morris, "Recovering sensitivity lost through convection in pure shift NMR," *Chemical Communications*, vol. 59, no. 84, pp. 12633–12636, 2023.

[52] N. Esturau, F. Sánchez-Ferrando, J. A. Gavin, C. Roumestand, M.-A. Delsuc, and T. Parella, "The use of sample rotation for minimizing convection effects in self-diffusion NMR measurements," *Journal of Magnetic Resonance*, vol. 153, pp. 48–55, nov 2001.

[53] T. Iwashita, T. Konuma, E. Harada, S. Mori, and K. Sugase, "Use of glass capillaries to suppress thermal convection in NMR tubes in diffusion measurements," *Magnetic Resonance in Chemistry*, vol. 54, pp. 729–733, apr 2016.

[54] A. Jerschow and N. Müller, "Suppression of convection artifacts in stimulated-echo diffusion experiments. double-stimulated-echo experiments," *Journal of Magnetic Resonance*, vol. 125, pp. 372–375, apr 1997.

[55] A. Jerschow, "Thermal convection currents in NMR: Flow profiles and implications for coherence pathway selection," *Journal of Magnetic Resonance*, vol. 145, pp. 125–131, jul 2000.

[56] N. M. Loening and J. Keeler, "Measurement of convection and temperature profiles in liquid samples," *Journal of Magnetic Resonance*, vol. 139, pp. 334–341, aug 1999.

[57] P. T. Callaghan and Y. Xia, "Velocity and diffusion imaging in dynamic NMR microscopy," *Journal of Magnetic Resonance (1969)*, vol. 91, pp. 326–352, feb 1991.

[58] G. G. Odian, "Principles of polymerization," 2004. Use copy Restrictions unspecified star MiAaHDL.

[59] A. Khokhlov and F. Kremer, "Basic concepts and polymer properties," in *Polymer Science: A Comprehensive Reference*, pp. 1–2, Elsevier, 2012.

[60] X.-J. Li, G.-P. Sun, Y.-F. Gong, and Y.-F. Li, "Recent research progress of n-type conjugated polymer acceptors and all-polymer solar cells," *Chinese Journal of Polymer Science*, vol. 41, pp. 640–651, feb 2023.

[61] F. Mahdavian, A. Allahbakhsh, A. R. Bahramian, D. Rodrigue, and M. K. Tiwari, "Flexible polymer hydrogels for wearable energy storage applications," *Advanced Materials Technologies*, vol. 8, jun 2023.

[62] M. Jagan and S. P. Vijayachamundeeswari, "A comprehensive investigation of lithium-based polymer electrolytes," *Journal of Polymer Research*, vol. 30, jun 2023.

[63] W. Chae, B. Kim, W. S. Ryoo, and T. Earmme, "A brief review of gel polymer electrolytes using in situ polymerization for lithium-ion polymer batteries," *Polymers*, vol. 15, p. 803, feb 2023.

[64] Z. Zhou, N. Luo, X. Shao, H.-L. Zhang, and Z. Liu, "Hyperbranched polymers for organic semiconductors," *ChemPlusChem*, vol. 88, jul 2023.

[65] H. Wang, G. Wang, L. Hu, B. Ge, X. Yu, and J. Deng, "Porous polymer materials for CO2 capture and electrocatalytic reduction," *Materials*, vol. 16, p. 1630, feb 2023.

[66] S. Haudum, P. Strasser, and I. Teasdale, "Phosphorus and silicon-based macromolecules as degradable biomedical polymers," *Macromolecular Bioscience*, jul 2023.

[67] T. S. Fischer, "Dynamic single-chain nanoparticles," 2018.

[68] M. Kato, M. Kamigaito, M. Sawamoto, and T. Higashimura, "Polymerization of methyl methacrylate with the carbon tetrachloride/dichlorotris- (triphenylphosphine)ruthenium(II)/methylaluminum bis(2,6-di-tert-butylphenoxide) initiating system: Possibility of living radical polymerization," *Macromolecules*, vol. 28, pp. 1721–1723, feb 1995.

[69] J.-S. Wang and K. Matyjaszewski, "Controlled/"living" radical polymerization. atom transfer radical polymerization in the presence of transition-metal complexes," *Journal of the American Chemical Society*, vol. 117, pp. 5614–5615, may 1995.

[70] M. Ouchi, N. Badi, J.-F. Lutz, and M. Sawamoto, "Single-chain technology using discrete synthetic macromolecules," *Nature Chemistry*, vol. 3, pp. 917–924, nov 2011.

[71] C. K. Lyon, A. Prasher, A. M. Hanlon, B. T. Tuten, C. A. Tooley, P. G. Frank, and E. B. Berda, "A brief user's guide to single-chain nanoparticles," *Polymer Chemistry*, vol. 6, no. 2, pp. 181–197, 2015.

[72] A. M. Hanlon, C. K. Lyon, and E. B. Berda, "What is next in single-chain nanoparticles?," *Macromolecules*, vol. 49, pp. 2–14, dec 2015.

[73] N. Hosono, M. A. J. Gillissen, Y. Li, S. S. Sheiko, A. R. A. Palmans, and E. W. Meijer, "Orthogonal self-assembly in folding block copolymers," *Journal of the American Chemical Society*, vol. 135, pp. 501–510, dec 2012.

[74] G. M. ter Huurne, L. N. J. de Windt, Y. Liu, E. W. Meijer, I. K. Voets, and A. R. A. Palmans, "Improving the folding of supramolecular copolymers by controlling the assembly pathway complexity," *Macromolecules*, vol. 50, pp. 8562–8569, oct 2017.

[75] R. J. Passarella, D. E. Spratt, A. E. van der Ende, J. G. Phillips, H. Wu, V. Sathiyakumar, L. Zhou, D. E. Hallahan, E. Harth, and R. Diaz, "Targeted nanoparticles that deliver a sustained, specific release of paclitaxel to irradiated tumors," *Cancer Research*, vol. 70, pp. 4550–4559, jun 2010.

[76] J. N. Lockhart, D. M. Stevens, D. B. Beezer, A. Kravitz, and E. Harth, "Dual drug delivery of tamoxifen and quercetin: Regulated metabolism for anticancer treatment with nanosponges," *Journal of Controlled Release*, vol. 220, pp. 751–757, dec 2015.

[77] D. H. Appella, L. A. Christianson, I. L. Karle, D. R. Powell, and S. H. Gellman, "-peptide foldamers: robust helix formation in a new family of -amino acid oligomers," *Journal of the American Chemical Society*, vol. 118, pp. 13071–13072, jan 1996.

[78] M. Oba, "Cell-penetrating peptide foldamers: Drug-delivery tools," *ChemBioChem*, vol. 20, pp. 2041–2045, jul 2019.

[79] H. Juwarker, J. min Suk, and K.-S. Jeong, "Foldamers with helical cavities for binding complementary guests," *Chemical Society Reviews*, vol. 38, no. 12, p. 3316, 2009.

[80] G. Lautrette, C. Aube, Y. Ferrand, M. Pipelier, V. Blot, C. Thobie, B. Kauffmann, D. Dubreuil, and I. Huc, "Tuning the guest-binding ability of a helically folded capsule by in situ modification of the aromatic oligoamide backbone," *Chemistry – A European Journal*, vol. 20, pp. 1547–1553, jan 2014.

[81] J. min Suk, V. R. Naidu, X. Liu, M. S. Lah, and K.-S. Jeong, "A foldamer-based chiroptical molecular switch that displays complete inversion of the helical sense upon anion binding," *Journal of the American Chemical Society*, vol. 133, pp. 13938–13941, aug 2011.

[82] J. min Suk and K.-S. Jeong, "Indolocarbazole-based foldamers capable of binding halides in water," *Journal of the American Chemical Society*, vol. 130, pp. 11868–11869, aug 2008.

[83] M. Rogošić, H. Mencer, and Z. Gomzi, "Polydispersity index and molecular weight distributions of polymers," *European Polymer Journal*, vol. 32, pp. 1337–1344, nov 1996.

[84] L. K. Kostanski, D. M. Keller, and A. E. Hamielec, "Size-exclusion chromatography—a review of calibration methodologies," *Journal of Biochemical and Biophysical Methods*, vol. 58, pp. 159–186, feb 2004.

[85] C. Botha, J. Höpfner, B. Mayerhöfer, and M. Wilhelm, "On-line SEC-MR-NMR hyphenation: optimization of sensitivity and selectivity on a 62 MHz benchtop NMR spectrometer," *Polymer Chemistry*, vol. 10, no. 18, pp. 2230–2246, 2019.

[86] M. Röding, D. Bernin, J. Jonasson, A. Särkkä, D. Topgaard, M. Rudemo, and M. Nydén, "The gamma distribution model for pulsed-field gradient NMR studies of molecular-weight distributions of polymers," *Journal of Magnetic Resonance*, vol. 222, pp. 105–111, sep 2012.

[87] B. Håkansson, M. Nydén, and O. Söderman, "The influence of polymer molecular-weight distributions on pulsed field gradient nuclear magnetic resonance self-diffusion experiments," *Colloid &amp Polymer Science*, vol. 278, pp. 399–405, may 2000.

[88] H. Walderhaug, O. Söderman, and D. Topgaard, "Self-diffusion in polymer systems studied by magnetic field-gradient spin-echo NMR methods," *Progress in Nuclear Magnetic Resonance Spectroscopy*, vol. 56, pp. 406–425, may 2010.

[89] P. T. Callaghan and D. N. Pinder, "A pulsed field gradient NMR study of self-diffusion in a polydisperse polymer system: dextran in water," *Macromolecules*, vol. 16, pp. 968–973, jun 1983.

[90] G. Fleischer, "The effect of polydispersity on measuring polymer self-diffusion with the n.m.r. pulsed field gradient technique," *Polymer*, vol. 26, pp. 1677–1682, oct 1985.

[91] R. Marega, V. Aroulmoji, M. Bergamin, L. Feruglio, F. Dinon, A. Bianco, E. Murano, and M. Prato, "Two-dimensional diffusion-ordered NMR spectroscopy as a tool for monitoring functionalized carbon nanotube purification and composition," *ACS Nano*, vol. 4, pp. 2051–2058, apr 2010.

[92] Y. Bakkour, V. Darcos, S. Li, and J. Coudane, "Diffusion ordered spectroscopy (DOSY) as a powerful tool for amphiphilic block copolymer characterization and for critical micelle concentration (CMC) determination," *Polymer Chemistry*, vol. 3, no. 8, p. 2006, 2012.

[93] J. P. Cole, J. J. Lessard, K. J. Rodriguez, A. M. Hanlon, E. K. Reville, J. P. Mancinelli, and E. B. Berda, "Single-chain nanoparticles containing sequence-defined segments: using primary structure control to promote secondary and tertiary structures in synthetic protein mimics," *Polymer Chemistry*, vol. 8, no. 38, pp. 5829–5835, 2017.

[94] K. Gu, J. Onorato, S. S. Xiao, C. K. Luscombe, and Y.-L. Loo, "Determination of the molecular weight of conjugated polymers with diffusion-ordered NMR spectroscopy," *Chemistry of Materials*, vol. 30, pp. 570–576, jan 2018.

[95] P. Lewinski, S. Sosnowski, S. Kazmierski, and S. Penczek, "scpl/scp-lactide polymerization studied by sup1/suph NMR with diffusion-ordered spectroscopy (DOSY): a "one NMR tube experiment" providing data on monomer conversion, polymer structure, msubn/sub and msubw/sub," *Polymer Chemistry*, vol. 6, no. 24, pp. 4353–4357, 2015.

[96] O. Altintas, D. Schulze-Suenninghausen, B. Luy, and C. Barner-Kowollik, "ABC-type miktoarm star terpolymers accessed by h-bonding driven supramolecular self-assembly," *European Polymer Journal*, vol. 62, pp. 409–417, jan 2015.

[97] K. Iijima, D. Aoki, H. Sogawa, S. Asai, and T. Takata, "Synthesis and characterization of supramolecular cross-linkers containing cyclodextrin dimer and trimer," *Polymer Chemistry*, vol. 7, no. 21, pp. 3492–3495, 2016.

[98] O. Altintas, P. Gerstel, N. Dingenouts, and C. Barner-Kowollik, "Single chain self-assembly: preparation of ,-donor–acceptor chains via living radical polymerization and orthogonal conjugation," *Chemical Communications*, vol. 46, no. 34, p. 6291, 2010.

[99] C. H. Wunderlich, R. G. Huber, R. Spitzer, K. R. Liedl, K. Kloiber, and C. Kreutz, "A novel paramagnetic relaxation enhancement tag for nucleic acids: A tool to study structure and dynamics of RNA," *ACS Chemical Biology*, vol. 8, pp. 2697–2706, oct 2013.

[100] G. Pintacuda, M. John, X.-C. Su, and G. Otting, "NMR structure determination of protein-ligand complexes by lanthanide labeling," *Accounts of Chemical Research*, vol. 40, pp. 206–212, jan 2007.

[101] J. EISINGER, R. G. SHULMAN, and W. E. BLUMBERG, "Relaxation enhancement by paramagnetic ion binding in deoxyribonucleic acid solutions," *Nature*, vol. 192, pp. 963–964, dec 1961.

[102] A. J. Lenard, F. A. Mulder, and T. Madl, "Solvent paramagnetic relaxation enhancement as a versatile method for studying structure and dynamics of biomolecular systems," *Progress in Nuclear Magnetic Resonance Spectroscopy*, vol. 132-133, pp. 113–139, oct 2022.

[103] T. S. Fischer, D. Schulze-Sünninghausen, B. Luy, O. Altintas, and C. Barner-Kowollik, "Stepwise unfolding of single-chain nanoparticles by chemically triggered gates," *Angewandte Chemie International Edition*, vol. 55, pp. 11276–11280, jun 2016.

[104] J. Nicolas, Y. Guillaneuf, C. Lefay, D. Bertin, D. Gigmes, and B. Charleux, "Nitroxide-mediated polymerization," *Progress in Polymer Science*, vol. 38, pp. 63–235, jan 2013.

[105] T. S. Fischer, J. Steinkoenig, H. Woehlk, J. P. Blinco, K. Fairfull-Smith, and C. Barner-Kowollik, "High resolution mass spectrometric access to nitroxide containing polymers," *Polymer Chemistry*, vol. 8, no. 35, pp. 5269–5274, 2017.

[106] N. D. Knöfel, H. Rothfuss, J. Willenbacher, C. Barner-Kowollik, and P. W. Roesky, "Platinum(II)-crosslinked single-chain nanoparticles: An approach towards recyclable homogeneous catalysts," *Angewandte Chemie International Edition*, vol. 56, pp. 4950–4954, apr 2017.

[107] J. Willenbacher, K. N. R. Wuest, J. O. Mueller, M. Kaupp, H.-A. Wagenknecht, and C. Barner-Kowollik, "Photochemical design of functional fluorescent single-chain nanoparticles," *ACS Macro Letters*, vol. 3, pp. 574–579, jun 2014.

[108] A. Mardyukov and A. Studer, "Preparation of photoactive polymers and post-modification via nitroxide trapping under UV irradiation," *Macromolecular Rapid Communications*, vol. 34, pp. 94–101, oct 2012.

[109] B. A. Chalmers, J. C. Morris, K. E. Fairfull-Smith, R. S. Grainger, and S. E. Bottle, "A novel protecting group methodology for syntheses using nitroxides," *Chemical Communications*, vol. 49, no. 88, pp. 10382–10384, 2013.

[110] E. Blasco, B. T. Tuten, H. Frisch, A. Lederer, and C. Barner-Kowollik, "Characterizing single chain nanoparticles (SCNPs): a critical survey," *Polymer Chemistry*, vol. 8, no. 38, pp. 5845–5851, 2017.

[111] Y. Song, Y. Ding, and C.-M. Dong, "scpstimuli-responsive/scp polypeptide nanoassemblies: Recent progress and applications in cancer nanomedicine," *WIREs Nanomedicine and Nanobiotechnology*, vol. 14, jul 2021.

[112] S. H. Pham, Y. Choi, and J. Choi, "Stimuli-responsive nanomaterials for application in antitumor therapy and drug delivery," *Pharmaceutics*, vol. 12, p. 630, jul 2020.

[113] C.-L. Liu, C.-H. Lin, C.-C. Kuo, S.-T. Lin, and W.-C. Chen, "Conjugated rod–coil block copolymers: Synthesis, morphology, photophysical properties, and stimuli-responsive applications," *Progress in Polymer Science*, vol. 36, pp. 603–637, may 2011.

[114] L. Greb, A. Eichhöfer, and J.-M. Lehn, "Internal c–c bond rotation in photoisomers of -bisimines: a light-responsive two-step molecular speed regulator based on double imine photoswitching," *European Journal of Organic Chemistry*, vol. 2016, pp. 1243–1246, feb 2016.

[115] G. Patias, A. M. Wemyss, S. Efstathiou, J. S. Town, C. J. Atkins, A. Shegiwal, R. Whitfield, and D. M. Haddleton, "Controlled synthesis of methacrylate and acrylate diblock copolymers ivia/i end-capping using CCTP and FRP," *Polymer Chemistry*, vol. 10, no. 47, pp. 6447–6455, 2019.

[116] S. Dong, B. Zheng, M. Zhang, X. Yan, X. Ding, Y. Yu, and F. Huang, "Preparation of a diblock supramolecular copolymer via self-sorting organization," *Macromolecules*, vol. 45, pp. 9070–9075, nov 2012.

[117] A. Mandal and A. F. M. Kilbinger, "Catalytic living ROMP: block copolymers from macro-chain transfer agents," *Polymer Chemistry*, vol. 14, no. 23, pp. 2797–2802, 2023.

[118] Z. Kokan, B. Kovačević, Z. Štefanić, P. Tzvetkova, and S. I. Kirin, "Controlling orthogonal self-assembly through icis/i–itrans/i isomerization of a non-covalent palladium complex dimer," *Chemical Communications*, vol. 54, no. 17, pp. 2094–2097, 2018.

[119] S. Garmendia, A. P. Dove, D. Taton, and R. K. O'Reilly, "Self-catalysed folding of single chain nanoparticles (SCNPs) by NHC-mediated intramolecular benzoin condensation," *Polymer Chemistry*, vol. 10, no. 18, pp. 2282–2289, 2019.

[120] O. Altintas, P. Krolla-Sidenstein, H. Gliemann, and C. Barner-Kowollik, "Single-chain folding of diblock copolymers driven by orthogonal h-donor and acceptor units," *Macromolecules*, vol. 47, pp. 5877–5888, aug 2014.

[121] P. A. Limacher and W. Klopper, "Computational study of the molecular structure and hydrogen bonding in the hamilton wedge/cyanuric acid binding motif," *ChemPhysChem*, vol. 18, pp. 3352–3359, oct 2017.

[122] K. Maurer-Chronakis, *Synthesis of Cyanuric Acid and Hamilton Receptor Functionalized Tetraphenylporphyrins: Investigation on the Chiroptical and Photophysical Properties of their Self-assembled Superstructures with Depsipeptide and Fullerene Dendrimers.* doctoralthesis, Friedrich-Alexander-Universität Erlangen-Nürnberg (FAU), 2011.

[123] G. Pagès, V. Gilard, R. Martino, and M. Malet-Martino, "Pulsed-field gradient nuclear magnetic resonance measurements (PFG NMR) for diffusion ordered spectroscopy (DOSY) mapping," *The Analyst*, vol. 142, no. 20, pp. 3771–3796, 2017.

[124] M. R. M. Koos, "Novel methods for modern nmr spectroscopy - optimized pulses and new experiments," 2017.

[125] S. C. Solleder, D. Zengel, K. S. Wetzel, and M. A. R. Meier, "A scalable and high-yield strategy for the synthesis of sequence-defined macromolecules," *Angewandte Chemie International Edition*, vol. 55, pp. 1204–1207, dec 2015.

[126] S. P. Rucker and A. Shaka, "Broadband homonuclear cross polarization in 2d n.m.r. using DIPSI-2," *Molecular Physics*, vol. 68, pp. 509–517, oct 1989.

[127] A. Shaka, J. Keeler, and R. Freeman, "Evaluation of a new broadband decoupling sequence: WALTZ-16," *Journal of Magnetic Resonance (1969)*, vol. 53, pp. 313–340, jun 1983.

[128] A. Shaka, J. Keeler, T. Frenkiel, and R. Freeman, "An improved sequence for broadband decoupling: WALTZ-16," *Journal of Magnetic Resonance (1969)*, vol. 52, pp. 335–338, apr 1983.

[129] M. H. Levitt, R. Freeman, and T. Frenkiel, "Supercycles for broadband heteronuclear decoupling," *Journal of Magnetic Resonance (1969)*, vol. 50, pp. 157–160, oct 1982.

[130] J. Cavanagh and M. Rance, "Suppression of cross-relaxation effects in TOCSY spectra via a modified DIPSI-2 mixing sequence," *Journal of Magnetic Resonance (1969)*, vol. 96, pp. 670–678, feb 1992.

[131] W. Peti *Journal of Biomolecular NMR*, vol. 18, no. 3, pp. 199–205, 2000.

[132] Y. Xia and P. T. Callaghan, "Study of shear thinning in high polymer solution using dynamic NMR microscopy," *Macromolecules*, vol. 24, pp. 4777–4786, aug 1991.

[133] K. I. Momot and P. W. Kuchel, "Convection-compensating diffusion experiments with phase-sensitive double-quantum filtering," *Journal of Magnetic Resonance*, vol. 174, pp. 229–236, jun 2005.

[134] A. Primikyri, E. Kyriakou, P. Charisiadis, C. Tsiafoulis, H. Stamatis, A. G. Tzakos, and I. P. Gerothanassis, "Fine-tuning of the diffusion dimension of –OH groups for high resolution DOSY NMR applications in crude enzymatic transformations and mixtures of organic compounds," *Tetrahedron*, vol. 68, pp. 6887–6891, aug 2012.

[135] S. Viel, L. Mannina, and A. Segre, "Detection of a – complex by diffusion-ordered spectroscopy (DOSY)," *Tetrahedron Letters*, vol. 43, pp. 2515–2519, apr 2002.

[136] M. Kfoury, D. Landy, S. Ruellan, L. Auezova, H. Greige-Gerges, and S. Fourmentin, "Determination of formation constants and structural characterization of cyclodextrin inclusion complexes with two phenolic isomers: carvacrol and thymol," *Beilstein Journal of Organic Chemistry*, vol. 12, pp. 29–42, jan 2016.

[137] M. J. Stchedroff, A. M. Kenwright, G. A. Morris, M. Nilsson, and R. K. Harris, "2d and 3d DOSY methods for studying mixtures of oligomeric dimethylsiloxanes," *Physical Chemistry Chemical Physics*, vol. 6, no. 13, p. 3221, 2004.

[138] K. Wang and K. Chen, "Direct assessment of oligomerization of chemically modified peptides and proteins in formulations using DLS and DOSY-NMR," *Pharmaceutical Research*, vol. 40, pp. 1329–1339, jan 2023.

[139] H. Liu, Y. Wang, Y. Lang, H. Yao, Y. Dong, and S. Li, "Bicontinuous cyclosporin a loaded water-AOT/tween 85-isopropylmyristate microemulsion: Structural characterization and dermal pharmacokinetics in vivo," *Journal of Pharmaceutical Sciences*, vol. 98, pp. 1167–1176, mar 2009.

[140] B. Antalek, "Using pulsed gradient spin echo NMR for chemical mixture analysis: How to obtain optimum results," *Concepts in Magnetic Resonance*, vol. 14, pp. 225–258, jan 2002.

[141] N. Cherifi, A. Khoukh, A. Benaboura, and L. Billon, "Diffusion-ordered spectroscopy NMR DOSY: an all-in-one tool to simultaneously follow side reactions, livingness and molar masses of polymethylmethacrylate by nitroxide mediated polymerization," *Polymer Chemistry*, vol. 7, no. 33, pp. 5249–5257, 2016.

[142] R. Plummer, D. J. T. Hill, and A. K. Whittaker, "DOSY NMR studies of chemical exchange behavior of poly(2-hydroxyethyl methacrylate)," *Macromolecules*, vol. 39, pp. 3878–3889, may 2006.

[143] L. Korchia, C. Bouilhac, V. Lapinte, C. Travelet, R. Borsali, and J.-J. Robin, "Photodimerization as an alternative to photocrosslinking of nanoparticles: proof of concept with amphiphilic linear polyoxazoline bearing coumarin unit," *Polymer Chemistry*, vol. 6, no. 33, pp. 6029–6039, 2015.

[144] M. Baier, D. Wöll, and S. Mecking, "Diffusion of molecular and macromolecular polyolefin probes in cylindrical block copolymer structures as observed by high temperature single molecule fluorescence microscopy," *Macromolecules*, vol. 51, pp. 1873–1884, feb 2018.

[145] S. C. Solleder, R. V. Schneider, K. S. Wetzel, A. C. Boukis, and M. A. R. Meier, "Recent progress in the design of monodisperse, sequence-defined macromolecules," *Macromolecular Rapid Communications*, vol. 38, p. 1600711, mar 2017.

[146] S. C. Solleder, S. Martens, P. Espeel, F. Du Prez, and M. A. R. Meier, "Combining two methods of sequence definition in a convergent approach: Scalable synthesis of highly defined and multifunctionalized macromolecules," *Chemistry – A European Journal*, vol. 23, pp. 13906–13909, sep 2017.

[147] K. S. Wetzel and M. A. R. Meier, "Monodisperse, sequence-defined macromolecules as a tool to evaluate the limits of ring-closing metathesis," *Polymer Chemistry*, vol. 10, no. 21, pp. 2716–2722, 2019.

[148] F. M. Arrabal-Campos, P. Oña-Burgos, and I. Fernández, "Molecular weight prediction with no dependence on solvent viscosity. a quantitative pulse field gradient diffusion NMR approach," *Polymer Chemistry*, vol. 7, no. 26, pp. 4326–4329, 2016.

[149] F. M. Arrabal-Campos, J. D. Álvarez, A. García-Sancho, and I. Fernández, "Molecular weight prediction in polystyrene blends. unprecedented use of a genetic algorithm in pulse field gradient spin echo (PGSE) NMR," *Soft Matter*, vol. 13, no. 37, pp. 6620–6626, 2017.

[150] S. Viamonte-Aristizábal, A. García-Sancho, F. M. A. Campos, J. A. Martínez-Lao, and I. Fernández, "Synthesis of high molecular weight l-polylactic acid (PLA) by reactive extrusion at a pilot plant scale: Influence of 1,12-dodecanediol and di(trimethylol propane) as initiators," *European Polymer Journal*, vol. 161, p. 110818, dec 2021.

[151] C. Chamignon, D. Duret, M.-T. Charreyre, and A. Favier, "sup1/suph DOSY NMR determination of the molecular weight and the solution properties of poly(in/i-acryloylmorpholine) in various solvents," *Macromolecular Chemistry and Physics*, vol. 217, pp. 2286–2293, jun 2016.

[152] N. H. Williamson, M. Nydén, and M. Röding, "The lognormal and gamma distribution models for estimating molecular weight distributions of polymers using PGSE NMR," *Journal of Magnetic Resonance*, vol. 267, pp. 54–62, jun 2016.

[153] A. Botana, J. A. Aguilar, M. Nilsson, and G. A. Morris, "J-modulation effects in DOSY experiments and their suppression: The oneshot45 experiment," *Journal of Magnetic Resonance*, vol. 208, pp. 270–278, feb 2011.

[154] J. D. Haller, "Selective averaging in high resolution liquid-state nmr: Application to coherence transfer and homonuclear decoupling," 2021.

[155] A. M. Torres, R. D. Cruz, and W. S. Price, "Removal of j-coupling peak distortion in PGSE experiments," *Journal of Magnetic Resonance*, vol. 193, pp. 311–316, aug 2008.

[156] Y. Shrot and L. Frydman, "Single-scan 2d DOSY NMR spectroscopy," *Journal of Magnetic Resonance*, vol. 195, pp. 226–231, dec 2008.

[157] L. Guduff, I. Kuprov, C. van Heijenoort, and J.-N. Dumez, "Spatially encoded 2d and 3d diffusion-ordered NMR spectroscopy," *Chemical Communications*, vol. 53, no. 4, pp. 701–704, 2017.

[158] N. M. Loening, J. Keeler, and G. A. Morris, "One-dimensional DOSY," *Journal of Magnetic Resonance*, vol. 153, pp. 103–112, nov 2001.

List of Figures

List of Tables

A. Appendix

A.1. Spectra SCNP MeTtap

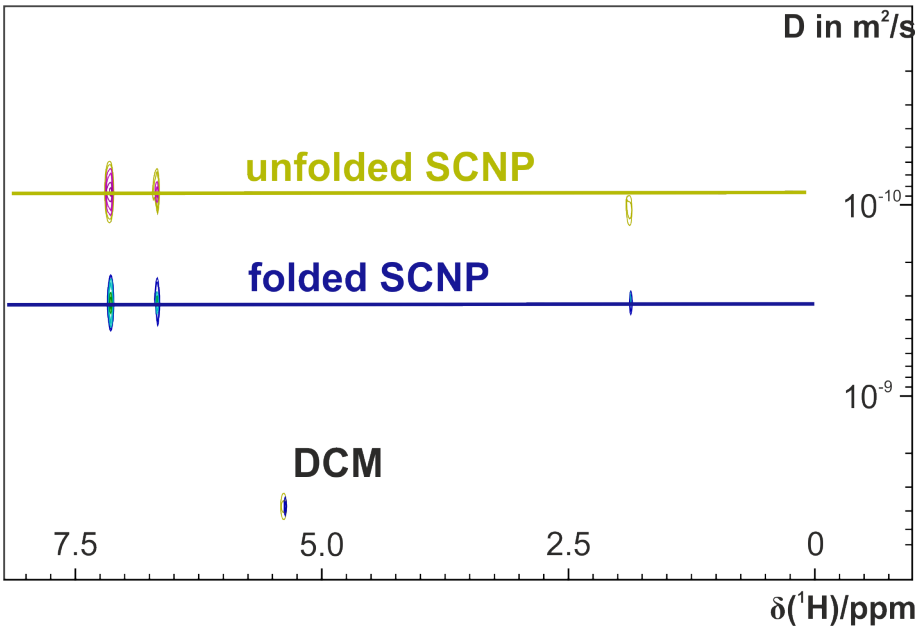

Figure A.1: DOSY plot of the folded and unfolded SCNP

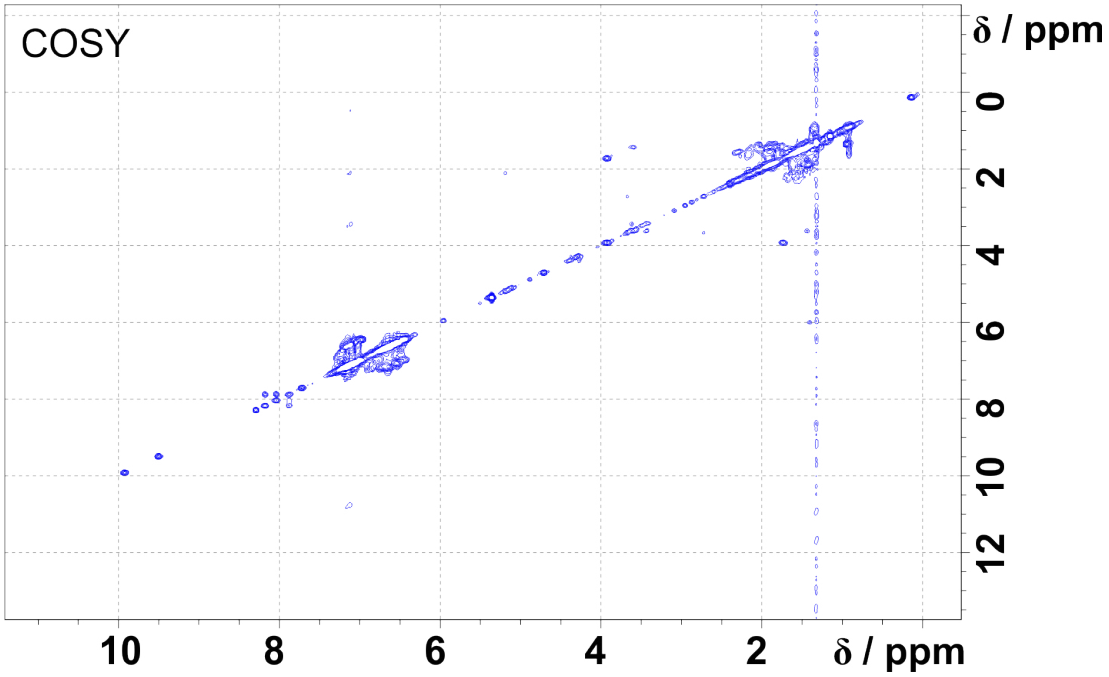

Figure A.2: COSY spectrum of the SCNP MeTrap

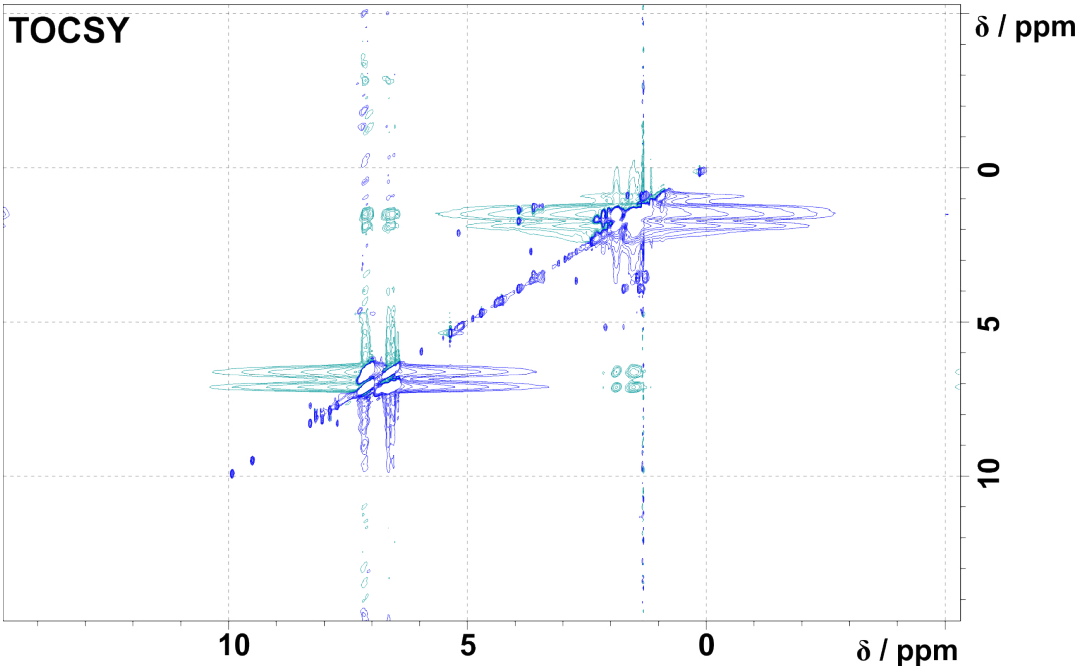

Figure A.3: TOCSY spectrum of the SCNP MeTrap

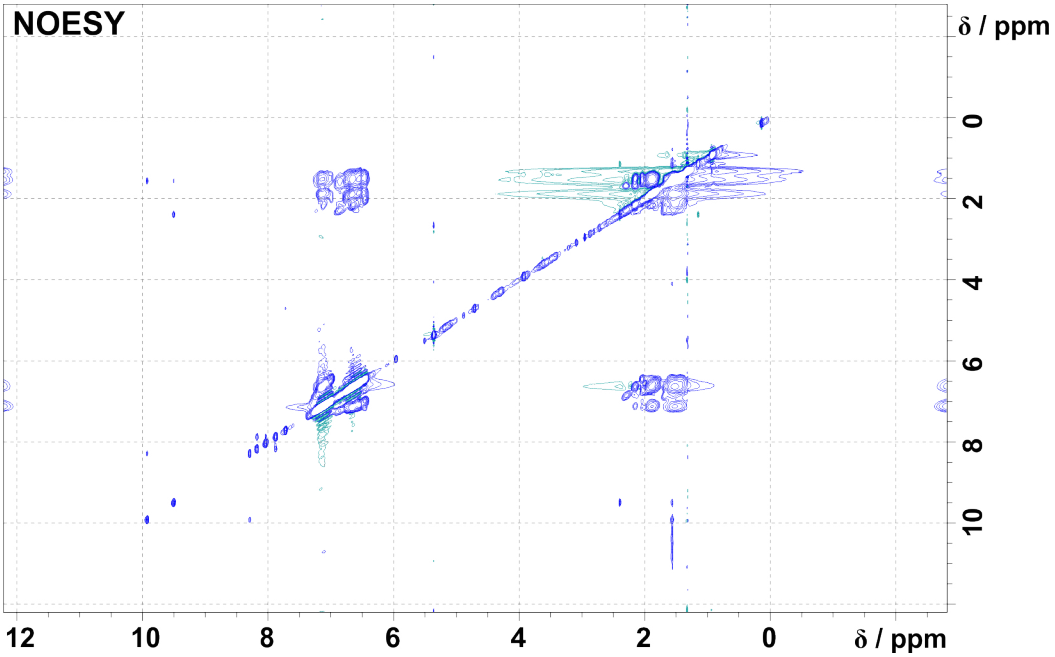

Figure A.4: NOESY spectrum of the SCNP MeTrap

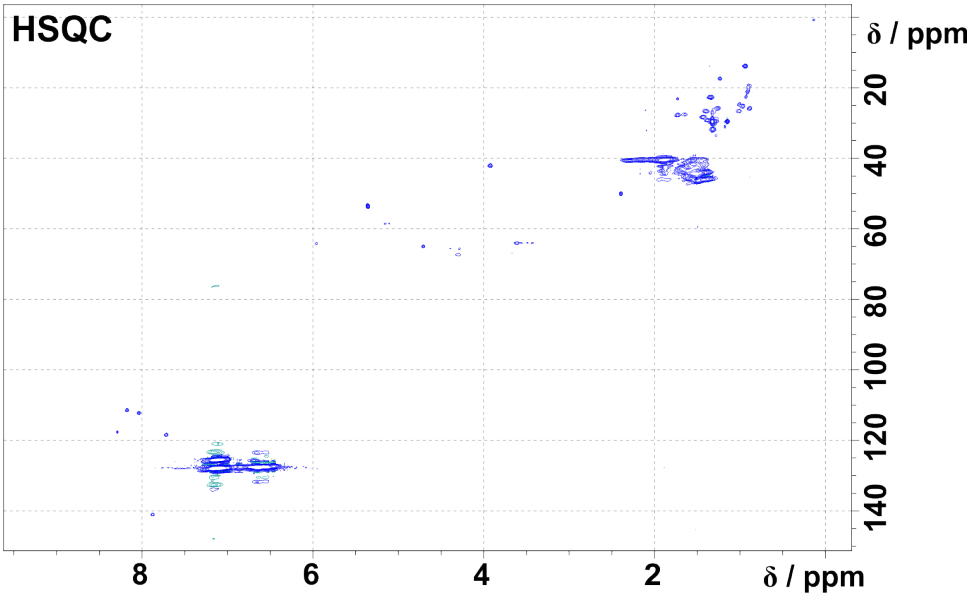

Figure A.5: HSQC spectrum of the SCNP MeTrap

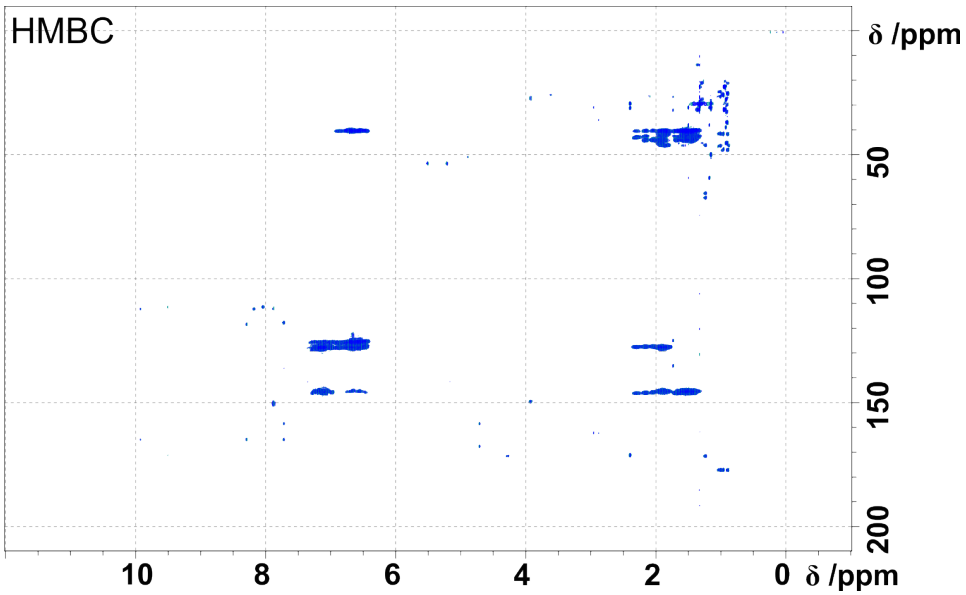

Figure A.6: HMBC spectrum of the SCNP MeTrap

A.2. SCNP orthogonal folding motif

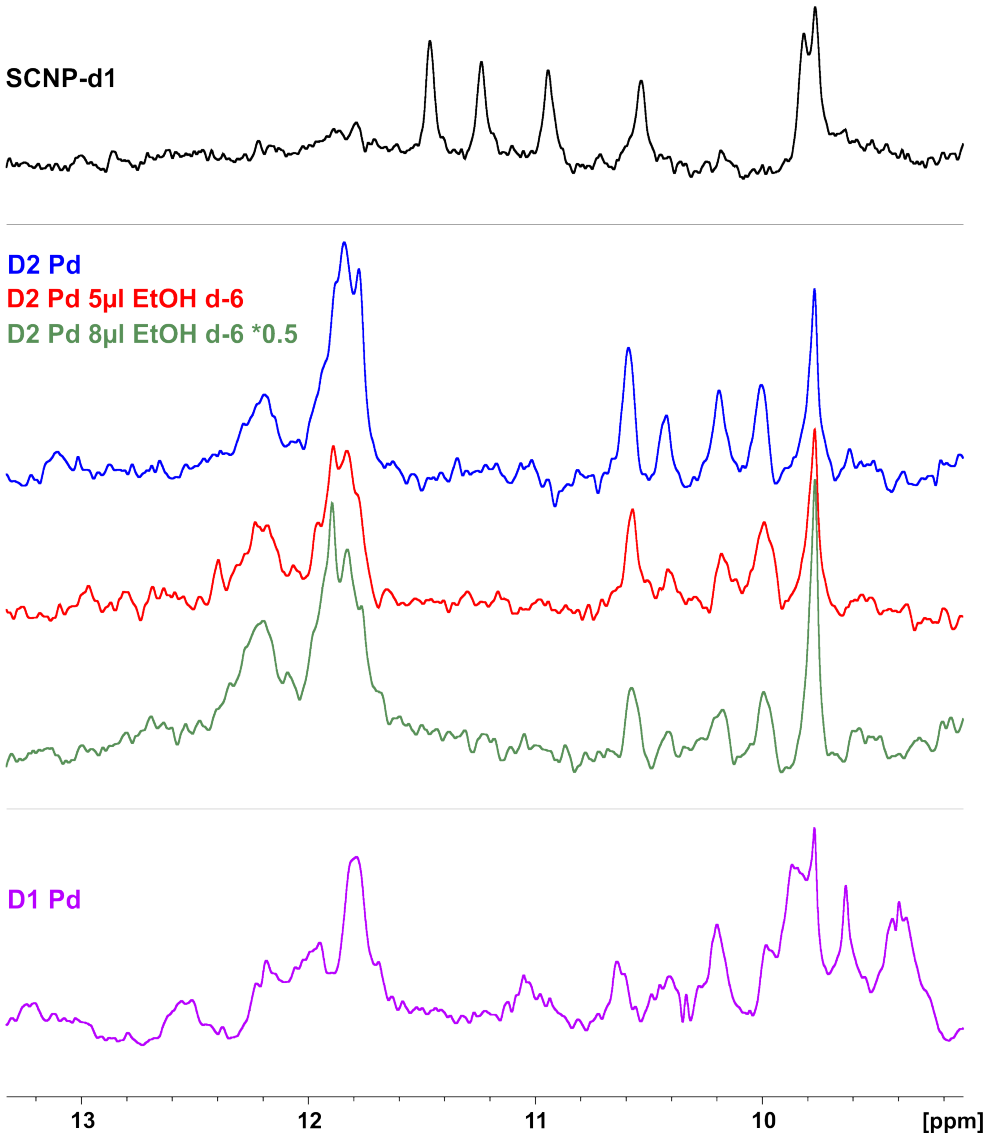

Figure A.7: 1D comparison of the dual folding SCNP.

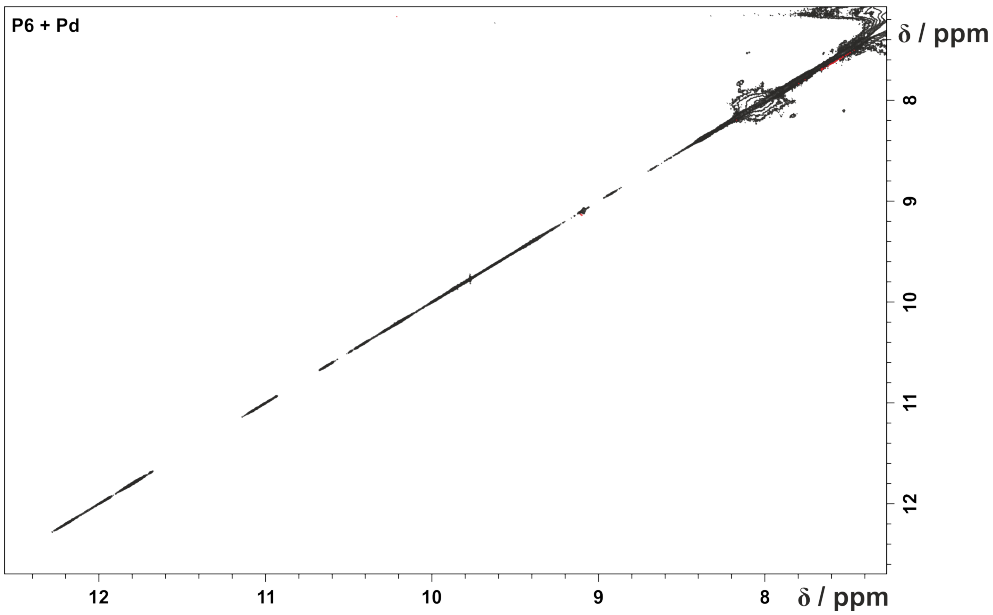

Figure A.8: NOESY spectrum of the precursor P6

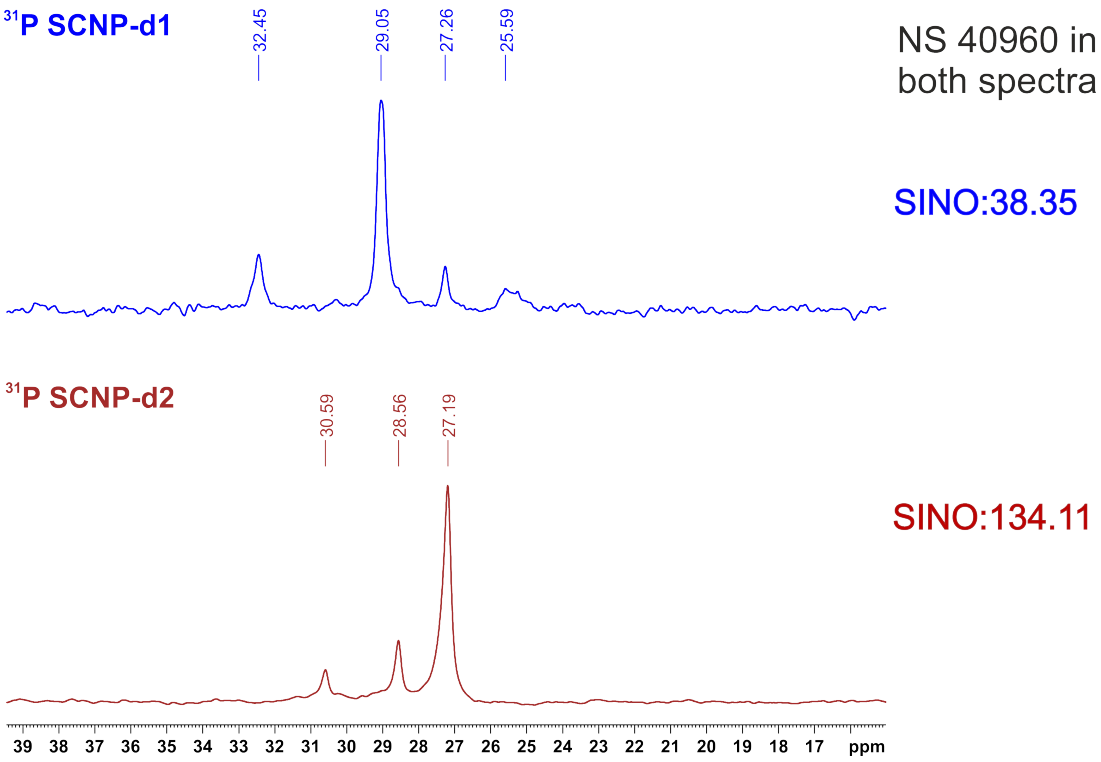

Figure A.9: P^{31} spectra of **SCNP-d1SCNP-d2**

A.3. Dispersity

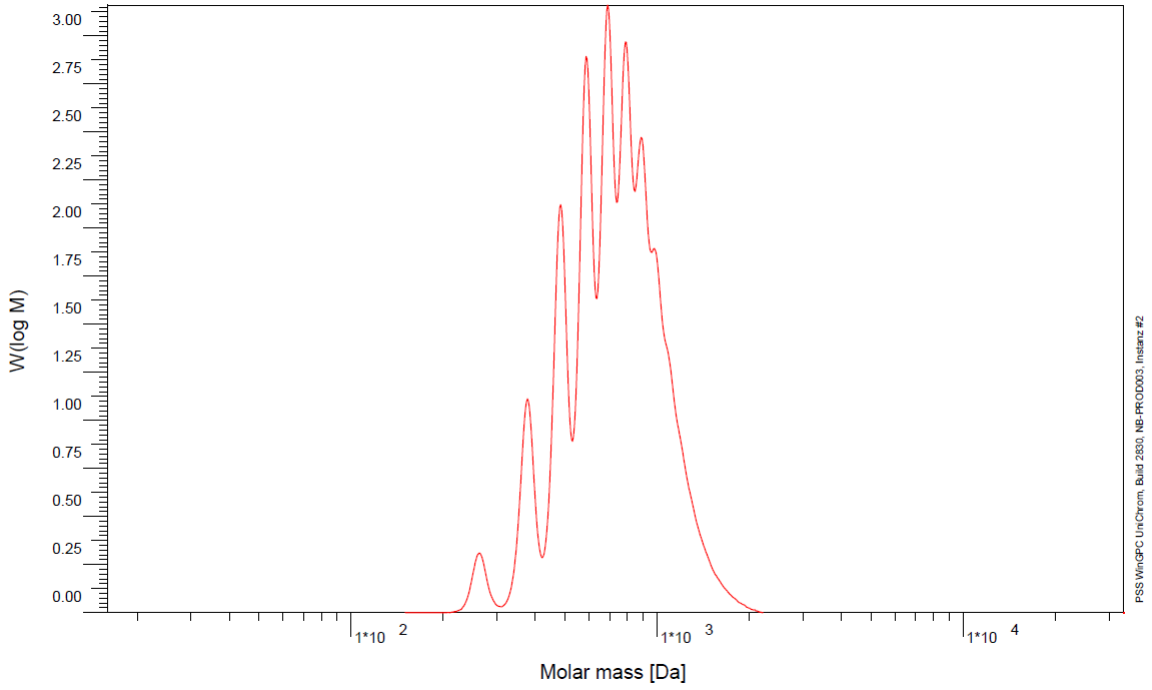

Figure A.10: GPC measurement of PSS-PS700.

A.4. Pulse Sequences

A.4.1. BETA DOSY

```
# 1 "/opt/topspin3.5pl6/exp/stan/nmr/lists/pp/user/stebpse_dipsi2_5_sp.bs"
;ledbpgp2s
;avance-version (12/01/11)
;2D sequence for diffusion measurement using stimulated
;    echo and LED
;using bipolar gradient pulses for diffusion
;using 2 spoil gradients
;
;D. Wu, A. Chen & C.S. Johnson Jr.,
;    J. Magn. Reson. A 115, 260-264 (1995).
;
;$CLASS=HighRes
;$DIM=2D
;$TYPE=
;$SUBTYPE=
;$COMMENT=
```

```
# 1 "/opt/topspin3.5pl6/exp/stan/nmr/lists/pp/Avance.incl" 1
;Avance3aqs.incl
;   for AV III with AQS IPSO
;
;avance-version (15/06/05)
;
;$CLASS=HighRes Incl
;$COMMENT=
# 170 "/opt/topspin3.5pl6/exp/stan/nmr/lists/pp/Avance.incl"
;$Id: Avance3aqs.incl,v 1.1.8.3 2015/03/05 16:46:54 ber Exp $
# 18 "/opt/topspin3.5pl6/exp/stan/nmr/lists/pp/user/stebpse_dipsi2_5_sp.bs"

# 1 "/opt/topspin3.5pl6/exp/stan/nmr/lists/pp/Grad.incl" 1
;Grad2.incl  -  include file for Gradient Spectroscopy
;   for TCU3
;
;avance-version (07/01/17)
;
;$CLASS=HighRes Incl
;$COMMENT=

# 27 "/opt/topspin3.5pl6/exp/stan/nmr/lists/pp/Grad.incl"
define list<gradient> EA=<EA>


# 31 "/opt/topspin3.5pl6/exp/stan/nmr/lists/pp/Grad.incl"
;$Id: Grad2.incl,v 1.14 2012/01/31 17:49:21 ber Exp $
# 19 "/opt/topspin3.5pl6/exp/stan/nmr/lists/pp/user/stebpse_dipsi2_5_sp.bs"

# 1 "/opt/topspin3.5pl6/exp/stan/nmr/lists/pp/Delay.incl" 1
;Delay.incl  -  include file for commonly used delays
;
;version (13/08/07)
;
;$CLASS=HighRes Incl
;$COMMENT=

# 9 "/opt/topspin3.5pl6/exp/stan/nmr/lists/pp/Delay.incl"
;general delays

define delay DELTA
define delay DELTA1
define delay DELTA2
define delay DELTA3
```

```
define delay DELTA4
define delay DELTA5
define delay DELTA6
define delay DELTA7
define delay DELTA8
define delay DELTA9
define delay DELTA10
define delay DELTA11
define delay DELTA12
define delay DELTA13
define delay DELTA14
define delay DELTA15
define delay DELTA16

define delay TAU
define delay TAU1
define delay TAU2
define delay TAU3
define delay TAU4
define delay TAU5
define delay TAU6
define delay TAU7
define delay TAU8
define delay TAU9
# 40 "/opt/topspin3.5pl6/exp/stan/nmr/lists/pp/Delay.incl"
define delay INCR1
define delay INCR2
define delay INCR3
define delay INCR4
define delay INCR5
define delay INCR6


;delays for centering pulses
# 50 "/opt/topspin3.5pl6/exp/stan/nmr/lists/pp/Delay.incl"
define delay CEN_HN1
define delay CEN_HN2
define delay CEN_HN3
define delay CEN_HC1
define delay CEN_HC2
define delay CEN_HC3
define delay CEN_HC4
define delay CEN_HP1
define delay CEN_HP2
define delay CEN_CN1
define delay CEN_CN2
```

```
define delay CEN_CN3
define delay CEN_CN4
define delay CEN_CP1
define delay CEN_CP2


;loop counters
# 69 "/opt/topspin3.5pl6/exp/stan/nmr/lists/pp/Delay.incl"
define loopcounter COUNTER
define loopcounter SCALEF
define loopcounter FACTOR1
define loopcounter FACTOR2
define loopcounter FACTOR3
define loopcounter FACTOR4
define loopcounter FACTOR5
define loopcounter FACTOR6


# 80 "/opt/topspin3.5pl6/exp/stan/nmr/lists/pp/Delay.incl"
;$Id: Delay.incl,v 1.14.2.1 2013/08/30 09:43:33 ber Exp $
# 20 "/opt/topspin3.5pl6/exp/stan/nmr/lists/pp/user/stebpse_dipsi2_5_sp.bs'


# 23 "/opt/topspin3.5pl6/exp/stan/nmr/lists/pp/user/stebpse_dipsi2_5_sp.bs'
define list<gradient> diff=<Difframp>
define delay bigDELTA
define delay littleDELTA


"p2=p1*2"
"d17=d16-4u"
# 32 "/opt/topspin3.5pl6/exp/stan/nmr/lists/pp/user/stebpse_dipsi2_5_sp.bs'
"FACTOR1=(d9/(p6*115.112))/2"
"l1=FACTOR1*2"

"bigDELTA=l1*p6*115.112+d16*4+p2+p30*2"
"littleDELTA=p30*2"

"acqt0=0"
# 1 "mc_line 41 file /opt/topspin3.5pl6/exp/stan/nmr/lists/pp/user/stebpse_
; dimension 2D; AQ_mode  (F1) QF
define delay MCWRK
define delay MCREST
define loopcounter t1loop
"t1loop=0"
define loopcounter ph1loop
```

```
"ph1loop=0"
define loopcounter ST1CNT
"ST1CNT = td1 / 1"
"MCREST = d1 - d1"
"MCWRK = 0.250000*d1"

    dccorr
# 41 "/opt/topspin3.5pl6/exp/stan/nmr/lists/pp/user/stebpse_dipsi2_5_sp.bs'
# 41 "/opt/topspin3.5pl6/exp/stan/nmr/lists/pp/user/stebpse_dipsi2_5_sp.bs'
1 ze
# 1 "mc_line 41 file /opt/topspin3.5pl6/exp/stan/nmr/lists/pp/user/stebpse_
LBLAV, MCWRK
      MCWRK
       "phval0 = t1loop * 1"
      MCWRK setgrad diff
# 42 "/opt/topspin3.5pl6/exp/stan/nmr/lists/pp/user/stebpse_dipsi2_5_sp.bs'
  bigDELTA                ;dummy for automated bigDELTA calculation
  littleDELTA  ;dummy for automated littleDELTA calculation
# 1 "mc_line 44 file /opt/topspin3.5pl6/exp/stan/nmr/lists/pp/user/stebpse_
2 MCWRK  * 3
LBLST1, MCWRK
  MCREST
# 45 "/opt/topspin3.5pl6/exp/stan/nmr/lists/pp/user/stebpse_dipsi2_5_sp.bs'

  50u setnmr3|0 setnmr0|34|32|33 ctrlgrad 0

  4u pl1:f1
# 50 "/opt/topspin3.5pl6/exp/stan/nmr/lists/pp/user/stebpse_dipsi2_5_sp.bs'
  (p10 ph1):f1

       d16
  p30:gp6*diff
  d16 pl0:f1

  (p60:sp60 ph2):f1
# 58 "/opt/topspin3.5pl6/exp/stan/nmr/lists/pp/user/stebpse_dipsi2_5_sp.bs'
  d16
       p30:gp6*-1*diff
  d16    pl10:f1


; tau M
;begin DIPSI2
# 66 "/opt/topspin3.5pl6/exp/stan/nmr/lists/pp/user/stebpse_dipsi2_5_sp.bs'
4 p6*3.556 ph23
  p6*4.556 ph25
```

```
  p6*3.222 ph23
  p6*3.167 ph25
  p6*0.333 ph23
  p6*2.722 ph25
  p6*4.167 ph23
  p6*2.944 ph25
  p6*4.111 ph23

  p6*3.556 ph25
  p6*4.556 ph23
  p6*3.222 ph25
  p6*3.167 ph23
  p6*0.333 ph25
  p6*2.722 ph23
  p6*4.167 ph25
  p6*2.944 ph23
  p6*4.111 ph25

  p6*3.556 ph25
  p6*4.556 ph23
  p6*3.222 ph25
  p6*3.167 ph23
  p6*0.333 ph25
  p6*2.722 ph23
  p6*4.167 ph25
  p6*2.944 ph23
  p6*4.111 ph25

  p6*3.556 ph23
  p6*4.556 ph25
  p6*3.222 ph23
  p6*3.167 ph25
  p6*0.333 ph23
  p6*2.722 ph25
  p6*4.167 ph23
  p6*2.944 ph25
  p6*4.111 ph23
  lo to 4 times l1

  ;end DIPSI2

  d16 pl1:f1
  p30:gp6*diff
  d16 pl0:f1
# 113 "/opt/topspin3.5pl6/exp/stan/nmr/lists/pp/user/stebpse_dipsi2_5_sp.bs
  (p60:sp60 ph3):f1
```

```
  d16
  p30:gp6*-1*diff
  d17

  4u setnmr3^0 setnmr0^34^32^33 ctrlgrad 7

  go=2 ph31
# 1 "mc_line 122 file /opt/topspin3.5pl6/exp/stan/nmr/lists/pp/user/stebpse
  MCWRK  wr #0 if #0 zd

  "t1loop+=1"
      MCWRK
      "phval0 = t1loop * 1"
      MCWRK setgrad diff
  lo to LBLST1 times ST1CNT
  MCWRK
  "t1loop=0"
  MCWRK rf #0
  lo to LBLAV times tdav
# 123 "/opt/topspin3.5pl6/exp/stan/nmr/lists/pp/user/stebpse_dipsi2_5_sp.bs
exit
# 128 "/opt/topspin3.5pl6/exp/stan/nmr/lists/pp/user/stebpse_dipsi2_5_sp.bs
ph1= 0
ph2= 0 2
ph3= 0 0 2 2
ph23=3
ph25=1
ph31=0;0 0 2  3 1 1 3 1 3 3 1


;pl1 : f1 channel - power level for pulse (default)
;p1  : f1 channel -  90 degree high power pulse
;p2  : f1 channel - 180 degree high power pulse
;p10 : f1 channel - Ernst flip angle pulse
;p19: gradient pulse 2 (spoil gradient)
;p30: gradient pulse (little DELTA * 0.5)
;d1  : relaxation delay; 1-5 * T1
;d9  : isotropic mixing time = approx. big DELTA
;d16: delay for gradient recovery
;ns: 4 * n; also n possible
;ds: 4 * m
;td1: number of experiments
;FnMODE: QF
;        use xf2 and DOSY processing
# 152 "/opt/topspin3.5pl6/exp/stan/nmr/lists/pp/user/stebpse_dipsi2_5_sp.bs
```

```
;use gradient ratio:    gp 6 : gp 7   : gp 8
;                       100  : -17.13 : -13.17

;for z-only gradients:
;gpz6: 100%
;gpz7: -17.13% (spoil)
;gpz8: -13.17% (spoil)

;use gradient files:
;gpnam6: SMSQ10.100
;gpnam7: SMSQ10.100
;gpnam8: SMSQ10.100
# 165 "/opt/topspin3.5pl6/exp/stan/nmr/lists/pp/user/stebpse_dipsi2_5_sp.bs
;use AU-program dosy to calculate gradient ramp-file Difframp


# 169 "/opt/topspin3.5pl6/exp/stan/nmr/lists/pp/user/stebpse_dipsi2_5_sp.bs
;$Id: ledbpgp2s,v 1.8 2012/01/31 17:49:27 ber Exp $
```

A.4.2. ccBETA DOSY

```
# 1 "/opt/topspin3.5pl6/exp/stan/nmr/lists/pp/user/stebpse_dipsi2_5_sp_CONVC
;ledbpgp2s
;avance-version (12/01/11)
;2D sequence for diffusion measurement using stimulated
;   echo and LED
;using bipolar gradient pulses for diffusion
;using 2 spoil gradients
;
;D. Wu, A. Chen & C.S. Johnson Jr.,
;   J. Magn. Reson. A 115, 260-264 (1995).
;
;$CLASS=HighRes
;$DIM=2D
;$TYPE=
;$SUBTYPE=
;$COMMENT=


# 1 "/opt/topspin3.5pl6/exp/stan/nmr/lists/pp/Avance.incl" 1
;Avance3aqs.incl
;   for AV III with AQS IPSO
;
;avance-version (15/06/05)
;
;$CLASS=HighRes Incl
```

```
;$COMMENT=
# 170 "/opt/topspin3.5pl6/exp/stan/nmr/lists/pp/Avance.incl"
;$Id: Avance3aqs.incl,v 1.1.8.3 2015/03/05 16:46:54 ber Exp $
# 18 "/opt/topspin3.5pl6/exp/stan/nmr/lists/pp/user/stebpse_dipsi2_5_sp_CONV

# 1 "/opt/topspin3.5pl6/exp/stan/nmr/lists/pp/Grad.incl" 1
;Grad2.incl - include file for Gradient Spectroscopy
;   for TCU3
;
;avance-version (07/01/17)
;
;$CLASS=HighRes Incl
;$COMMENT=

# 27 "/opt/topspin3.5pl6/exp/stan/nmr/lists/pp/Grad.incl"
define list<gradient> EA=<EA>


# 31 "/opt/topspin3.5pl6/exp/stan/nmr/lists/pp/Grad.incl"
;$Id: Grad2.incl,v 1.14 2012/01/31 17:49:21 ber Exp $
# 19 "/opt/topspin3.5pl6/exp/stan/nmr/lists/pp/user/stebpse_dipsi2_5_sp_CONV

# 1 "/opt/topspin3.5pl6/exp/stan/nmr/lists/pp/Delay.incl" 1
;Delay.incl - include file for commonly used delays
;
;version (13/08/07)
;
;$CLASS=HighRes Incl
;$COMMENT=

# 9 "/opt/topspin3.5pl6/exp/stan/nmr/lists/pp/Delay.incl"
;general delays

define delay DELTA
define delay DELTA1
define delay DELTA2
define delay DELTA3
define delay DELTA4
define delay DELTA5
define delay DELTA6
define delay DELTA7
define delay DELTA8
define delay DELTA9
define delay DELTA10
define delay DELTA11
define delay DELTA12
```

```
define delay DELTA13
define delay DELTA14
define delay DELTA15
define delay DELTA16

define delay TAU
define delay TAU1
define delay TAU2
define delay TAU3
define delay TAU4
define delay TAU5
define delay TAU6
define delay TAU7
define delay TAU8
define delay TAU9
# 40 "/opt/topspin3.5pl6/exp/stan/nmr/lists/pp/Delay.incl"
define delay INCR1
define delay INCR2
define delay INCR3
define delay INCR4
define delay INCR5
define delay INCR6


;delays for centering pulses
# 50 "/opt/topspin3.5pl6/exp/stan/nmr/lists/pp/Delay.incl"
define delay CEN_HN1
define delay CEN_HN2
define delay CEN_HN3
define delay CEN_HC1
define delay CEN_HC2
define delay CEN_HC3
define delay CEN_HC4
define delay CEN_HP1
define delay CEN_HP2
define delay CEN_CN1
define delay CEN_CN2
define delay CEN_CN3
define delay CEN_CN4
define delay CEN_CP1
define delay CEN_CP2


;loop counters
# 69 "/opt/topspin3.5pl6/exp/stan/nmr/lists/pp/Delay.incl"
define loopcounter COUNTER
```

```
define loopcounter SCALEF
define loopcounter FACTOR1
define loopcounter FACTOR2
define loopcounter FACTOR3
define loopcounter FACTOR4
define loopcounter FACTOR5
define loopcounter FACTOR6


# 80 "/opt/topspin3.5pl6/exp/stan/nmr/lists/pp/Delay.incl"
;$Id: Delay.incl,v 1.14.2.1 2013/08/30 09:43:33 ber Exp $
# 20 "/opt/topspin3.5pl6/exp/stan/nmr/lists/pp/user/stebpse_dipsi2_5_sp_CONV


# 23 "/opt/topspin3.5pl6/exp/stan/nmr/lists/pp/user/stebpse_dipsi2_5_sp_CONV
define list<gradient> diff=<Difframp>
define delay bigDELTA
define delay littleDELTA


"p2=p1*2"
"d17=d16-4u"
# 32 "/opt/topspin3.5pl6/exp/stan/nmr/lists/pp/user/stebpse_dipsi2_5_sp_CONV
"FACTOR1=(d9/(p6*115.112))/2"
"l1=FACTOR1"
"l2=FACTOR1"

"bigDELTA=2*(l1*p6*115.112+d16*4+p60+p30*2)"
"littleDELTA=p30*2"
"d20=bigDELTA+d16/2"

"acqt0=0"
# 1 "mc_line 43 file /opt/topspin3.5pl6/exp/stan/nmr/lists/pp/user/stebpse_d
; dimension 2D; AQ_mode  (F1) QF
define delay MCWRK
define delay MCREST
define loopcounter t1loop
"t1loop=0"
define loopcounter ph1loop
"ph1loop=0"
define loopcounter ST1CNT
"ST1CNT = td1 / 1"
"MCREST = d1 - d1"
"MCWRK = 0.250000*d1"

    dccorr
```

```
# 43 "/opt/topspin3.5pl6/exp/stan/nmr/lists/pp/user/stebpse_dipsi2_5_sp_CONV
# 43 "/opt/topspin3.5pl6/exp/stan/nmr/lists/pp/user/stebpse_dipsi2_5_sp_CONV
1 ze
# 1 "mc_line 43 file /opt/topspin3.5pl6/exp/stan/nmr/lists/pp/user/stebpse_d
LBLAV, MCWRK
      MCWRK
       "phval0 = t1loop * 1"
      MCWRK setgrad diff
# 44 "/opt/topspin3.5pl6/exp/stan/nmr/lists/pp/user/stebpse_dipsi2_5_sp_CONV
  bigDELTA                ;dummy for automated bigDELTA calculation
  littleDELTA  ;dummy for automated littleDELTA calculation
# 1 "mc_line 46 file /opt/topspin3.5pl6/exp/stan/nmr/lists/pp/user/stebpse_d
2 MCWRK  * 3
LBLST1, MCWRK
  MCREST
# 47 "/opt/topspin3.5pl6/exp/stan/nmr/lists/pp/user/stebpse_dipsi2_5_sp_CONV

  50u setnmr3|0 setnmr0|34|32|33 ctrlgrad 0

  4u pl1:f1
# 52 "/opt/topspin3.5pl6/exp/stan/nmr/lists/pp/user/stebpse_dipsi2_5_sp_CONV
  (p10 ph1):f1

       d16
  p30:gp6*diff
  d16 pl0:f1

  (p60:sp60 ph2):f1
# 60 "/opt/topspin3.5pl6/exp/stan/nmr/lists/pp/user/stebpse_dipsi2_5_sp_CONV
  d16
       p30:gp6*-1*diff
  d16    pl10:f1


; tau M
;begin DIPSI2
# 68 "/opt/topspin3.5pl6/exp/stan/nmr/lists/pp/user/stebpse_dipsi2_5_sp_CONV
4 p6*3.556 ph23
  p6*4.556 ph25
  p6*3.222 ph23
  p6*3.167 ph25
  p6*0.333 ph23
  p6*2.722 ph25
  p6*4.167 ph23
  p6*2.944 ph25
  p6*4.111 ph23
```

```
  p6*3.556 ph25
  p6*4.556 ph23
  p6*3.222 ph25
  p6*3.167 ph23
  p6*0.333 ph25
  p6*2.722 ph23
  p6*4.167 ph25
  p6*2.944 ph23
  p6*4.111 ph25

  p6*3.556 ph25
  p6*4.556 ph23
  p6*3.222 ph25
  p6*3.167 ph23
  p6*0.333 ph25
  p6*2.722 ph23
  p6*4.167 ph25
  p6*2.944 ph23
  p6*4.111 ph25

  p6*3.556 ph23
  p6*4.556 ph25
  p6*3.222 ph23
  p6*3.167 ph25
  p6*0.333 ph23
  p6*2.722 ph25
  p6*4.167 ph23
  p6*2.944 ph25
  p6*4.111 ph23
  lo to 4 times l1

  ;end DIPSI2

  d16 pl1:f1
  p30:gp6*diff
  d16 pl0:f1
# 115 "/opt/topspin3.5pl6/exp/stan/nmr/lists/pp/user/stebpse_dipsi2_5_sp_CON
  (p60:sp60 ph3):f1

  d16
  p30:gp6*-1*diff
  d16
        d16
  p30:gp6*-1*diff
  d16 pl0:f1
```

```
  (p60:sp60 ph2):f1
# 126 "/opt/topspin3.5pl6/exp/stan/nmr/lists/pp/user/stebpse_dipsi2_5_sp_CON
  d16
       p30:gp6*diff
  d16    pl10:f1


; tau M
;begin DIPSI2
# 134 "/opt/topspin3.5pl6/exp/stan/nmr/lists/pp/user/stebpse_dipsi2_5_sp_CON
5 p6*3.556 ph23
  p6*4.556 ph25
  p6*3.222 ph23
  p6*3.167 ph25
  p6*0.333 ph23
  p6*2.722 ph25
  p6*4.167 ph23
  p6*2.944 ph25
  p6*4.111 ph23

  p6*3.556 ph25
  p6*4.556 ph23
  p6*3.222 ph25
  p6*3.167 ph23
  p6*0.333 ph25
  p6*2.722 ph23
  p6*4.167 ph25
  p6*2.944 ph23
  p6*4.111 ph25

  p6*3.556 ph25
  p6*4.556 ph23
  p6*3.222 ph25
  p6*3.167 ph23
  p6*0.333 ph25
  p6*2.722 ph23
  p6*4.167 ph25
  p6*2.944 ph23
  p6*4.111 ph25

  p6*3.556 ph23
  p6*4.556 ph25
  p6*3.222 ph23
  p6*3.167 ph25
  p6*0.333 ph23
```

```
  p6*2.722 ph25
  p6*4.167 ph23
  p6*2.944 ph25
  p6*4.111 ph23
  lo to 5 times l2

  ;end DIPSI2

  d16 pl1:f1
  p30:gp6*-1*diff
  d16 pl0:f1
# 181 "/opt/topspin3.5pl6/exp/stan/nmr/lists/pp/user/stebpse_dipsi2_5_sp_CON
  (p60:sp60 ph3):f1

  d16
  p30:gp6*diff
  d17

  4u setnmr3^0 setnmr0^34^32^33 ctrlgrad 7

  go=2 ph31
# 1 "mc_line 190 file /opt/topspin3.5pl6/exp/stan/nmr/lists/pp/user/stebpse_
  MCWRK  wr #0 if #0 zd

  "t1loop+=1"
      MCWRK
       "phval0 = t1loop * 1"
      MCWRK setgrad diff
  lo to LBLST1 times ST1CNT
  MCWRK
  "t1loop=0"
  MCWRK rf #0
  lo to LBLAV times tdav
# 191 "/opt/topspin3.5pl6/exp/stan/nmr/lists/pp/user/stebpse_dipsi2_5_sp_CON
exit
# 196 "/opt/topspin3.5pl6/exp/stan/nmr/lists/pp/user/stebpse_dipsi2_5_sp_CON
ph1= 0
ph2= 0 2
ph3= 0 0 2 2
ph23=3
ph25=1
ph31=0;0 0 2  3 1 1 3 1 3 3 1


;pl1 : f1 channel - power level for pulse (default)
;p1  : f1 channel -  90 degree high power pulse
```

```
;p2  : f1 channel - 180 degree high power pulse
;p10 : f1 channel - Ernst flip angle pulse
;p19: gradient pulse 2 (spoil gradient)
;p30: gradient pulse (little DELTA * 0.5)
;d1  : relaxation delay; 1-5 * T1
;d9  : isotropic mixing time = approx. big DELTA
;d16: delay for gradient recovery
;ns: 4 * n; also n possible
;ds: 4 * m
;td1: number of experiments
;FnMODE: QF
;         use xf2 and DOSY processing
# 220 "/opt/topspin3.5pl6/exp/stan/nmr/lists/pp/user/stebpse_dipsi2_5_sp_CON
;use gradient ratio:    gp 6 : gp 7   : gp 8
;                       100  : -17.13 : -13.17

;for z-only gradients:
;gpz6: 100%
;gpz7: -17.13% (spoil)
;gpz8: -13.17% (spoil)

;use gradient files:
;gpnam6: SMSQ10.100
;gpnam7: SMSQ10.100
;gpnam8: SMSQ10.100
# 233 "/opt/topspin3.5pl6/exp/stan/nmr/lists/pp/user/stebpse_dipsi2_5_sp_CON
;use AU-program dosy to calculate gradient ramp-file Difframp


# 237 "/opt/topspin3.5pl6/exp/stan/nmr/lists/pp/user/stebpse_dipsi2_5_sp_CON
;$Id: ledbpgp2s,v 1.8 2012/01/31 17:49:27 ber Exp $
```

A.5. Python Programs

A.5.1. Python Code Gamma Distribution

```
# -*- coding: utf-8 -*-
"""
Created on Thu Aug 10 08:24:34 2023

@author: kx6269
"""


import numpy as np
import scipy.stats as stats
import matplotlib.pyplot as plt
```

```
from sklearn import preprocessing


name= "Polystyrene Weight Distribution"


alpha = 0.51
K = 1e-7


x = np.linspace(5e-11, 2e-9, 100) #Diffusionswerte
mx = np.linspace(1e3, 5e6, 10000) #f r Massenverteilungsvergleich



# dSTE  shape=6.85587004095, scale=9.62754201633e-11
# ccBETA shape=7.070323556, scale=9.33716085578e-11




#dSTE
#mx =  (x/K)**(-1/alpha)
y1 = stats.gamma.pdf(x, a=6.85587004095, scale=9.62754201633e-11) #Diffwert
x2 = K * (mx**(-alpha))
y2 = stats.gamma.pdf(x2, a=6.85587004095, scale=9.62754201633e-11) #Massenv


#ccBETA
y3 = stats.gamma.pdf(x, a=7.070323556, scale=9.33716085578e-11) #Diffw dSTE
x4 = K * (mx**(-alpha))
y4 = stats.gamma.pdf(x4, a=7.070323556, scale=9.33716085578e-11) #Massenw d

plt.plot(x, y1, label='dSTE: shape=6.85587004095, scale=9.62754201633e-11')
#plt.plot(mx, y2, label='dSTE: shape=6.85587004095, scale=9.62754201633e-1

plt.plot(x, y3, label='ccBETA: shape=7.070323556, scale=9.33716085578e-11')
#plt.plot(mx, y4, label='ccBETA: shape=7.070323556, scale=9.33716085578e-1

plt.xscale("log")
plt.xlabel("$D [m^2/s^{-1}]$")                                  #Einheit Diffusi
#plt.xlabel("$M_w [g mol^{-1}]$")                                 #Einheit Mass
#plt.plot(sec_x, sec_yn, label='SEC')
plt.legend()

plt.savefig('Polystyrene_Diffusion_Distribution.png')
```

```
plt.savefig('Polystyrene_Diffusion_Distribution.pdf')
plt.savefig('Polystyrene_Diffusion_Distribution.svg')
plt.show()
```

A.5.2. Python Code DOSY FIT

```
import numpy as np
import nmrglue as ng
import matplotlib.pyplot as plt
import scipy


# ------------------------------------------------------
# Set parameters here:
SI = 32

name = "PS700_ccBETA"
DOSY_folder = "nmr/45"                          # DOSY experiment
DOSY_2D = DOSY_folder + "/pdata/1"                          # xf2 processed ->
DOSY_1D = DOSY_folder + "/pdata/999"          # do .pp or .int here!
GAMMA = 4172

extract = "integral"                        # set to "integral" or "peaklist"
results = {}
D_init = 10**(-9)
sigma_init = 10**(-9)
alpha = 0.51                  #alpha for PS
kappa = "...."

kap = 422 / 1215 + 23 / (1080 * np.pi ** 2)   #calculate gradient shape val
lam = 0.5

noiseLimitLeft = 10
noiseLimitRight = 9
# ------------------------------------------------------



# ------------------------------------------------------
# define functions

def get_scale(dic, dic_proc, key, key_proc):
    outp = {}
    outp['ax'] = dic_proc[key_proc]['AXNAME']
    outp['nuc'] = dic_proc[key_proc]['AXNUC']
    outp['SWppm'] = dic[key]['SW']
```

```
    outp['SWHz'] = dic_proc[key_proc]['SW_p']
    outp['ppm'] = outp['SWHz'] / outp['SWppm']
    outp['O1Hz'] = dic[key]['O1']
    outp['ac_O1ppm'] = outp['O1Hz']/outp['ppm'] + outp['SWppm'] / 2
    outp['O1ppm'] = dic_proc[key_proc]['OFFSET']
    outp['lim'] = [outp['O1ppm'], outp['O1ppm'] - outp['SWppm']]
    outp['np'] = dic_proc[key_proc]['STSI']
    outp['axppm'] = np.linspace(outp['lim'][0], outp['lim'][1], outp['np'])
    return outp


def find_nearest(array, value):
    idx = (np.abs(array - value)).argmin()
    return [idx, array[idx]]


# DOSY functions
def load_difflist(path_to_file):
    tmp = open(path_to_file+"/difflist", 'r')
    load_data = tmp.read()
    load_data = load_data.split('\n')
    tmp.close()
    return np.array([float(line) for line in load_data if line != ''])


def extract_DOSY(xaxis, data, area):
    l = find_nearest(xaxis, area[0])
    r = find_nearest(xaxis, area[1])
    return data[:, l[0]:r[0]]


def read_peaklist(peaklist_dir):
    f = open(peaklist_dir+"/peaklist.xml","r+")
    peaklist_data = f.read()
    f.close()

    i = 1; peaklist = {}
    for line in peaklist_data.split("\n"):
        line = line.split(" ")
        if "<Peak1D" in line:
            peaklist[i] = [ float(l.split("=")[1][1:-1]) for l in line if '
            i += 1
        return peaklist


def read_integrals(integrals_dir):
```

```
        f = open(integrals_dir+"/integrals.txt","r+")
        integrals_data = f.read()
        f.close()

        flag=False; integrals = {}
        for line in integrals_data.split("\n"):
                line = [l for l in line.split(" ") if l != ""]
                try:
                        if line[0] == "1": flag = True
                except: pass
                if flag and line != []:
                        i = int(line[0])
                        integrals[i] = [ float(l) for l in line[1:]]
        return integrals
#-------------------------------------------------------------------------------




#-------------------------------------------------------------------------------
# read in DOSY data
dic, data = ng.bruker.read(DOSY_folder)                                  # load raw
dic_proc, data_proc = ng.bruker.read_pdata(DOSY_2D)     # load processed da
F2 = get_scale(dic, dic_proc, 'acqus', 'procs')

if extract == "integral": # use integrals
    integrals = read_integrals(DOSY_1D)
    expdata = {}
    for i, area in integrals.items():
        temp = extract_DOSY(F2["axppm"], data_proc, area)
        expdata[i] = np.sum(temp[:SI, :], axis=1)

elif extract == "peaklist": # use peaklist
    peaklist = read_peaklist(DOSY_1D)
    expdata = {}
    for i, peak in peaklist.items():
        index = find_nearest(F2["axppm"], peak[0])
        expdata[i] = np.concatenate(data_proc[:SI, index[0]-1:index[0]])

else: raise ValueError("Define the variable extract as: \"integral\" or \"
#-------------------------------------------------------------------------------




#-------------------------------------------------------------------------------
```

```
# Set parameters for DOSY decay here:
difflist = load_difflist(DOSY_folder)

g = difflist * 100
gam = GAMMA * 2*np.pi

P2 = dic["acqus"]["P"][2] * 10**(-6)
P30 = dic["acqus"]["P"][30] * 10**(-6)
D16 = dic["acqus"]["D"][16]
D20 = dic["acqus"]["D"][20]

tau = D16 + P2
delta = 2*P30
DELTA = D20 + ((2*kap - 2*lam - 1) * 2*P30) / 4 - tau / 2

l = find_nearest(F2['axppm'], noiseLimitLeft)
r = find_nearest(F2['axppm'], noiseLimitRight)
error = 3 * np.std(data_proc[0, l[0]:r[0]])
# ------------------------------------------------------------



# ------------------------------------------------------------
# least squares fit with scipy.optimize.curve_fit

def singleExp(g, A, D):  # define the fit function --> single exponential
    return A * np.exp(- D * gam**2 * delta**2 * g**2 * DELTA)

# Guo's gamma distribution: alpha = kappa and beta = 1/theta
def gammaDistFit(g, A, Dmean, sigma):  # define the fit function --> single
    B = gam**2 * delta**2 * g**2 * DELTA
    return  A * np.abs(1 + B * sigma**2 / Dmean) ** (-1 * Dmean**2 / sigma*


for i, expdat in expdata.items():  #

    test_low = np.log( (expdat-error) / expdat)

    popt_gamma, pcov_gamma = scipy.optimize.curve_fit(gammaDistFit, g, expo
    perr_gamma = np.sqrt(np.diag(pcov_gamma))

    Dmean = popt_gamma[1]
    sigma = popt_gamma[2]

    PDI = (1 + sigma**2 / Dmean**2) ** (1 / alpha**2)
    shape = ((Dmean**2)/(sigma)**2) #kappa, or alpha
```

```
    scale = ((sigma**2)/(Dmean)) #theta
    rate = ((Dmean)/(sigma**2)) #beta

    popt_lin, pcov_lin = scipy.optimize.curve_fit(singleExp, g, expdat, p0=
    perr_lin = np.sqrt(np.diag(pcov_lin))

    results[(name, i)] = [popt_lin, perr_lin] #saves A, D, B and errors for

    if extract=="peaklist": plt.title("D = %1.4E"% (popt_gamma[1])+"
sigma: %1.4E"% (popt_gamma[2])+ "\n PDI: %1.3E"% (PDI)+"   peak:"+str(peak
    elif extract=="integral": plt.title("D = %1.4E"% (popt_gamma[1])+"
sigma: %1.4E"% (popt_gamma[2])+ "\n PDI: %1.3E"% (PDI)+"   peak:"+str(integ
    plt.xlabel(r"$(G/cm)^2$ x $10^3$")
    plt.ylabel("f(x)")
    plt.plot(g**2, expdat, "bd")        #draws measurement points
    plt.plot(g**2, gammaDistFit(g, popt_gamma[0], popt_gamma[1], popt_gamma
    # plt.semilogy(g**2, expdat, "ro")
    plt.semilogy(g**2, singleExp(g, popt_lin[0], popt_lin[1]))
    plt.savefig(str(name)+"_peak"+str(i)+".png")
    plt.savefig(str(name)+"_peak"+str(i)+".pdf")
    plt.savefig(str(name)+"_peak"+str(i)+".svg")
    plt.show()
    plt.close("all")

# ____________________________________________________________
```

```
# # ____________________________________________________________
# SI units
# - D * gam^2 * g^2 * delta^2 * DELTA
# m2/s * 1/(G s)^2 * (G/m)^2 * s^2 * s

# D = m2 / s
# delta = s
# DELTA = s
# gam / 10^4 * 10^6 = MHz / (T * 10^4) = 10^6 * MHz / G = Hz / G
# 100 * difflist = G / m = g
# # ____________________________________________________________
```

B. Danksagung

Ich danke Herrn Prof. Burkhard Luy für die Unterstützung und die Bereitstellung des Themas.

Vielen Dank an Prof. Gisela Guthausen für die erfolgreiche wissenschaftliche Zusammenarbeit.

Gerne Blicke ich zurück an die Zeit im Sonderforschungsbereich SFB 1176 für die tollen Kooperationen.

Desweiteren danke ich dem Arbeitskreis Bulu für die zahlreichen wissenschaftlichen Gespräche.

Besonderer Dank gilt Thomas, Martin, Jens, Pavleta und Ella für die anregenden Gespräche und Unterstützung.

Ebenfalls möchte ich meinen ehemaligen Bachelorstudenten Anna, Ricardo, Kati und Felicia danken, die meine Leidenschaft für Wissenschaft und Lehre immer wieder auf's neue entfacht haben.

Hervorheben möchte ich Nadja, die mich immer wieder motiviert hat weiter zu machen und für die tolle Zeit im Arbeitskreis.

Sehr gefreut habe ich mich über die entstandene Freundschaft zu Carlo, den ich über die Zeit am KIT kennengelernt habe.

Meine Familie und Freunde haben mir über die ganzen Jahre immer zur Seite gestanden. Danke dafür!

Ohne meine Frau Karoline und meine Söhne Karl und Johann hätte ich das nie geschafft. Danke und ich liebe euch!